DISSERTATION

A K-ϵ TURBULENCE MODEL FOR PREDICTING THE THREE-DIMENSIONAL VELOCITY FIELD AND BOUNDARY SHEAR IN CLOSED AND OPEN CHANNELS

Submitted by

Youssef Ismail Hafez

Civil Engineering Department

In partial fulfillment of the requirements

for the degree of Doctor of Philosophy

Colorado State University

Fort Collins, Colorado

Spring 1995

COLORADO STATE UNIVERSITY

Spring, 1995

WE HEREBY RECOMMEND THAT THE DISSERTATION PREPARED UNDER OUR SUPERVISION BY YOUSSEF ISMAIL HAFEZ ENTITLED "A K-ϵ TURBULENCE MODEL FOR PREDICTING THE THREE-DIMENSIONAL VELOCITY FIELD AND BOUNDARY SHEAR IN CLOSED AND OPEN CHANNELS" BE ACCEPTED AS FULFILLING IN PART REQUIREMENTS FOR THE DEGREE OF DOCTOR OF PHILOSOPHY.

Committee on Graduate Work

Albert Molinas

Bogusz Bienkiewicz

Kurt Gerow

Erik Thompson

Co-Advisor

Advisor

Department Head

ABSTRACT OF DISSERTATION

A K-ϵ TURBULENCE MODEL FOR PREDICTING THE THREE-DIMENSIONAL VELOCITY FIELD AND BOUNDARY SHEAR IN CLOSED AND OPEN CHANNELS

The objectives of this dissertation are to predict the three-dimensional velocity field and boundary shear in closed and open channels. Attention is given to the secondary motion effects on the main velocity and boundary shear. Secondary motion is induced by wall corners, free surfaces, or periodic roughness changes. Channels are straight and rectangular with different aspect ratios and different wall roughness conditions including lateral periodic bed roughness changes in open channels.

A finite element computer model was developed to solve the Reynolds equations of motion and continuity for steady and fully developed mean turbulent flow. Turbulent stresses appearing in the Reynolds equations are modeled in terms of mean velocity gradients and turbulent viscosity. The non-linear algebraic stress model developed by Speziale (1987) is used in closed channels, while that of Naot and Rodi (1982) is used in open channels with new algebraic surface proximity functions. A two equation turbulence model consisting of the turbulent kinetic energy (K), and its rate of dissipation

(ϵ) evaluates the turbulent viscosity that appears in the algebraic stress models.

The system of governing equations is divided into two groups: one for the continuity and momentum equations, and the other for the turbulent kinetic energy (K) and its rate of dissipation (ϵ) equations. The two groups of equations are solved sequentially rather than simultaneously, assuming one group is known while solving for the other, until convergence and compatibility are obtained.

The four-node bilinear element is used to linearly approximate each of the velocities, K, and ϵ while a single point quadrature approximates the pressure as a constant over the element. The iterative penalty approach is used to eliminate the continuity equation and to replace the pressure in the equations of motion.

The Galerkin finite element method together with the finite element approximations are used to transform the non-linear governing partial differential equations into non-linear integral equations. These equations are casted in a form suitable for applying Newton's method which solves non-linear equations. The integral equations are integrated using a Gaussian quadrature to reduce the equations to non-linear algebraic equations. The equations are stored in a non-symmetric skyline matrix which significantly reduces the matrix size.

The equations are linearized and solved using the Gauss forward elimination and back substitution technique. The relaxation factor is taken equal to unity and convergence is obtained in all the cases considered herein.

For both hydraulically smooth and rough wall square ducts, the eight symmetrical vortex structure of the secondary velocities is successfully predicted. The Secondary velocities cause bulging of the main velocity contours into the corners and shifting of the maximum wall shear stress toward the corner in agreement with the experimental data by Leutheusser (1963). In this study, the prediction of the magnitude of the secondary velocities along the duct walls and corner bisectors is in better agreement with the experimental data of Gessner and Emery (1980) than are the numerical predictions of Naot and Rodi (1982), and Demuren and Rodi (1984).

Rectangular ducts with a depth over width ratio of 1:3 (aspect ratio 1:3) are investigated. The secondary velocity structure at the corner bisectors is similar to that of the square ducts except that the two corner vortices are no longer symmetrical with a larger vortex in the direction of the longer side. Roughness over all walls in square and rectangular ducts increases the magnitude of the secondary velocities but has the same secondary velocity pattern as smooth walled ducts.

In square and rectangular ducts with two opposite walls smooth and the other two rough, the vortices at the smooth walls are much stronger than those at the rough walls. This could be utilized in industrial applications where convection of mass and heat in ducts can be directed to the smooth walls rather than to the rough walls.

In hydraulically smooth open channels (aspect ratio 1:2), using quadratic surface-proximity functions, the depression of the main velocity maximum is simulated well at about 0.6 H above the bed level. Secondary velocities are no longer symmetrical with respect to the wall corner bisector as was in the square duct due to the presence of the free surface. The upper free surface vortex is much stronger than the lower corner one and occupies a much larger area. The effect of the free surface on the rate of dissipation (ϵ) is well simulated by using a gradient open surface boundary condition for ϵ developed by Yacoub et al. (1992). This results in dampening of the turbulent viscosity near the free surface consistent with the experimental observation of Ueda et al. (1977). The bed shear stress is maximum at the channel center, while the side wall shear stress is maximum at 0.46 H above the bed, and decreases in the upward and downward directions due to the effect of the strong upper vortex.

For hydraulically rough open channels (aspect ratio 1:2), similar features were predicted as with the smooth ones. But here, an increase in the strength of the secondary velocities causes the velocity maximum to be depressed to 0.57 H above the bed. When the side walls of the open channel (aspect ratio 1:2) are smooth and the bottom wall is rough, the strength and size of the lower corner vortex decreases significantly and the velocity maximum moves to the free surface.

For wider rectangular open channels with aspect ratio about 1:4, the same features as open channels with aspect ratio 1:2 are predicted, except that the upper vortex extends latterly from the bank about 1.1 to 1.7 times the flow depth depending upon the wall roughness conditions. Beyond that region there is a very weak vortex in the central part of the channel which allows the primary velocity maxima to be on the free surface.

In the case of periodic roughness for which data of Muller and Studerus (1979) exists, cubic surface proximity functions are used to avoid negative values of K and ϵ. Owing to the periodic roughness distribution, a cellular secondary velocity structure develops in which the secondary velocities are directed downward over the rough parts and upward over the smooth parts with a corresponding wavy pattern of the main velocity and bed shear stress. Regions of high bed shear are in the down flow regions and vice versa. Bed shear at the rough stripes is about twice the shear over the adjacent smooth ones.

When the roughness of the rough stripes increases from 0.0025 m to 0.012 m, the magnitude of the cellular secondary cells increases significantly, and the main velocity, K, and ϵ contour lines display an increasing wavy pattern. Bed shear over the rough stripes is about 4.5 times that at the adjacent smooth ones. When the same experiment with the periodic roughness is simulated, while interchanging the rough stripes with smooth ones, the secondary velocity structure adjusts correspondingly to preserve downflows over the rough stripes and upflows over the smooth stripes.

When the whole bottom of the channel is simulated with one uniform roughness, the cellular pattern disappears indicating that the cellular secondary structure is predicted only in the case of periodic roughness.

In all simulated cases, prediction of the average main velocity and hence the discharge is very satisfactory with an error of about 1 percent in the square duct, 3 percent in rectangular ducts, and $\pm$ 6 percent in open channels. The error increase in open channel cases is primarily due to uncertainty in the energy slope given to the computer model.

The model successfully predicts the three various types of secondary motion generated by corners, free surfaces, and periodic roughnesses. The magnitude of secondary velocities is well predicted in the case of closed channels but slightly over-predicted in the case of open channels. The turbulent kinetic energy and the dissipation rate are also well predicted in both closed and open channels, even though past researchers had difficulty obtaining solutions for much simpler flow problems.

In general, the model predictions are very good despite the complexity of the turbulent flow phenomena, the high non-linearity of the governing equations, the large number of variables, and the lack of certain data for calibration of the model.

Youssef Ismail Hafez
Civil Engineering
Colorado State University
Fort Collins, Colorado 80521
Spring 1995

ACKNOWLEDGEMENTS

I wish to express my deepest gratitude to my advisor Dr. Johannes Gessler for his guidance, help, and support throughout this study. Likewise my thanks go to the co-advisor Dr. Erik Thompson for his valuable comments and suggestions. Thanks are due to: Dr. Albert Molinas, Dr. Bogusz Bienkiewicz, and Dr. Kurt Georg for encouraging me to carry this study.

Special thanks to my friend Eehab Khalil for his great help in typing this dissertation. I also appreciate the help and support from my friends: Amr Fadl, Hani Noshi, Tarek Halim, Mahmoud El-Neklawi, and Abedl-Rahman Abdel-Rahman.

I would like also to make special thanks to Debbie Buderus for her care and support throughout this study.

To my brother Dr. Mohamed I Hafez, who has been a role model for me, I express my gratitude. Likewise my gratitude goes to my sisters Wafaa, Amina, Eman, my teacher Shiek Abdel Azizi, and the rest of my family for their prayers for me to succeed in this study.

To my parents Ismail Hafez and Amal Soliman, I wish to say thanks for always being loving, caring, and supporting. Your prayers for me have been so helpful specially in hard times.

To

the support and dedication of my parents:

my mother

Amal Soliman

and my father

Ismail Hafez

TABLE OF CONTENTS

Chapter **Page**

CHAPTER I

INTRODUCTION

Ever since the beginning of history, water has been flowing in channels, rivers, seas, and oceans providing ways of life for drinking, irrigation, fishing, and navigation. This led mankind to try controlling the flow of water by building dams, conduits, and navigation channels. To do so, it is essential to understand how water flows and how it responds to man-made structures. In modern day life, fluids especially water and air, are an important part to many industries. Transport processes of mass and heat in industrial applications depend significantly upon the momentum transport phenomenon which is affected by velocity and boundary shear. Thus, the velocity of fluids and how fluids overcome the boundary resistance of channels are the most relevant pieces of information needed for the process of understanding and controlling the flow.

As the flows are often turbulent, attention is given to the characteristics of turbulent flows in closed and open channels. Turbulent flows are characterized by being three-dimensional (i.e., consisting of a primary component in the main flow direction and two secondary components in the plane of the cross section).

Most studies in hydraulics and fluid mechanics dealt with the primary flow and associated transport processes of momentum, mass, and heat in the longitudinal direction. Only recently have effects of secondary motion been included. This limited such studies to one or two dimensional analysis in spite of the obvious effects of the secondary motion.

Secondary motions are generated by the anisotropy of the normal turbulent stresses which is greatest near a corner, along a boundary wall, or along the free surface of a channel. Hence these secondary motions are called "turbulence-driven" secondary motion or Prandtle second kind. They are fundamentally different from the curvature induced secondary motion or Prandtle first kind caused by the centrifugal forces in curved channels. The turbulence-driven secondary motions are not present in laminar flows where the turbulent stresses are zero, or in circular conduits where for symmetry considerations the turbulent stresses are isotropic.

Although the magnitude of the secondary currents in straight channels is small as compared to the main flow (generally less than 5 percent of the main flow), they have great effects on the distributions of the main velocity, the boundary shear, and the turbulent viscosity. Secondary motions are responsible for shifting the main velocity maximum to a point below the free surface, bulging of primary velocity contours toward the corners of the cross section, three-dimensional sediment distributions and bed configurations (such as sand ribbons in straight rivers), and shifting the bed shear stress maximum toward the corner. These features are very important for sediment transport, bank erosion, and stable canal design.

As the magnitude of the secondary motions is small, their experimental evaluation becomes very difficult and hence the need for a mathematical determination. Governing equations which form the basis of analysis for the three-dimensional velocity distributions are the Reynolds equations of motion and continuity. The Reynolds equations result from dividing the instantaneous values of the velocities and pressure into mean (time average) and fluctuating quantities, and by substituting the sums into the continuity and

Navier-Stokes equations. This results in the appearance of turbulent stresses which need to be evaluated. To close the equations, the turbulent stresses are often modeled in terms of mean flow velocity gradients and turbulent viscosity, thus establishing the turbulence model. The two equation model (K-ϵ) evaluates the turbulent viscosity which appears in the turbulence model.

The objectives of this dissertation are to numerically predict the three dimensional velocity field and boundary shear in closed and open channels by developing a finite element computer model that solves the governing equations for steady, and fully developed turbulent flows. The numeric model predicts the main velocity, the secondary velocities, the boundary shear, and the K-ϵ distributions over the flow cross section of straight closed and open channels. The effects of the geometry of the cross section and the distribution of the wall roughness are investigated. Computational results are compared with existing experimental data.

This dissertation starts with a review of secondary motion effects, velocity and boundary shear distributions, turbulent flow governing equations, origin of secondary motions followed by methods of their predictions and measurements, K-ϵ turbulence model, boundary conditions of turbulent flows, and finite element method for turbulent flow problems. Then, the mathematical model is described, followed by its application to a number of flow conditions in closed and open channels. At the end of the dissertation conclusions and recommendations are presented.

CHAPTER II

THEORY AND LITERATURE REVIEW

The theory reviewed in this chapter concerns turbulent flows in closed and open channels. The flows of interest throughout this study are incompressible, steady, fully developed, and have a high Reynolds number (i.e. one in the fully turbulent range). Under steady conditions all time derivatives of mean values are zero. Under fully developed conditions all gradients of mean values in the main flow direction are zero except the longitudinal pressure gradient (dp/dx) in closed channels, which is the constant driving force of the flow.

The velocity field is three dimensional and is represented by the main and secondary velocities, while the geometry of the flow domain is two dimensional and is represented by the cross section of the channel.

The topics which explain the turbulent flow phenomena in closed and open channels fall into the following categories.

(1) Secondary motion effects.

(2) Velocity and boundary shear.

(3) Turbulent flow governing equations.

(4) Linear eddy viscosity model.

(5) Origin of secondary motions.

(6) Measurements of secondary motions.

(7) Prediction of secondary motions.

(8) K-ϵ turbulence model.

(9) Boundary conditions of turbulent flow problems.

(10) Finite element method for turbulent flow problems.

2.1 Secondary Motion Effects:

In the last century, Thomson (1878) first reported the effect of secondary motions in open channels. He attributes the depression of the velocity maximum below the free surface of open channels to the secondary motions. The secondary motion along the free surface transports low momentum fluid from the banks toward the center of the channel, leading to the lower velocity at the surface.

In square ducts, a similar process occurs near the corners where fluid with lower momentum flows from the central part of the walls to the core region of the duct. At the same time, fluid with higher momentum flows from the core region along the duct diagonals to the corner regions, thus causing bulging of the velocity contours to the corners. A similar bulging was observed by Nikuradse (1926) in water flume experiments.

The corner induced secondary motion shifts the bed shear stress maximum toward the corner as measured by Leutheusser (1963) in a square duct, and by Gosh and Roy (1970) in trapezoidal open channel flow. This shift in bed shear is important for sediment transport and erosion problems.

In natural open channel flows, secondary flow cells associated with lateral variation of bed roughness and three-dimensional sediment distributions and bed configurations are reported by Vanoni (1946), Kinoshita (1967), Culbertson (1967), and Karcz (1973).

Vanoni (1946) describes the pattern of sand ribbons transported along the flume bed. He concludes that secondary circulation is caused by the addition of sediments, and that this type of circulation might also exist in natural channels.

Kinoshita (1967) found through an aerial photo survey of flood rivers that a boil produced a low-speed zone at the surface and that high-speed zones were formed with spacing twice the flow depth. He suggests that cellular secondary currents might exist in straight rivers which have a pair of counter rotating vortices with vortex diameters equal to about the flow depth.

Culbertson (1967) observed sand trails, or ribbons of sand in the Rio Grande conveyance channel near Bernardo, New Mexico. He attributes this formation which occurred in the upper flat bed regime, to the effect of helical flow cells.

Karcz (1973) also observed patterns of continuous longitudinal ridges and troughs. He attributes these to flow-configurations characterized by streamwise-persisting and rhythmic spanwise variation in velocity. He reports the presence of these ribbons at velocities both lower and higher than those required to produce ripples. He also indicates that larger sand ribbons are best visible at, or close to, transition to the upper-bed regime.

In laboratory flumes, Muller and Studerus (1979) performed experiments to simulate sand ribbons by attaching roughness stripes on the smooth bed of a flume. They observed cellular secondary structure where secondary flow is directed downward over the rough stripes and upward over the smooth ones. The cross sectional primary velocity

, K, and ϵ contours follow the secondary motion in the same way.

Nezu and Nakagawa (1984) claim that the existence of free surface is not an essential cause of cellular secondary currents, and hence carried their experiments in air conduit where more accurate measurements could be conducted. They attached longitudinal ridge elements onto both the lower and upper bottoms of the conduit simulating the longitudinal ridges and troughs of river bed forms (i.e., sand ribbons). They observed cellular secondary structure where the secondary flow, and consequently the primary velocity and turbulent variables, were directed downward over the troughs and upward over the ridges.

2.2 Velocity and Boundary Shear:

The velocity field of fluid flow is affected by the shear on the walls of the channel. The reverse is also true. This interrelationship between the velocity field and the boundary shear is explicitly expressed for one dimensional flows. For example, the well known resistance to flow formula by Chezy (1775) expressed this relation as

$$\frac{u_{av}}{u_*} = \frac{c}{\sqrt{g}} \tag{2.2.1}$$

with

$$u_* = \sqrt{\frac{\textit{wall shear stress}}{\rho}} \tag{2.2.2}$$

where u_{av} is the cross sectional average longitudinal velocity, u_* is the primary shear velocity which is related to the primary wall shear via (2.2.2), c is Chezy's resistance coefficient, g is the gravitational acceleration, and ρ is the fluid density.

Prandtl (1925) introduced the mixing length theory which relates the primary turbulent shear stress to the local mean flow velocity gradient. As a consequence, the relationship between the mean flow longitudinal velocity and the boundary shear for hydraulically smooth boundaries is the logarithmic law of the wall

$$\frac{u(y)}{u_*} = A \log \left(\frac{u_* \, y}{\nu}\right) + B \qquad (2.2.3)$$

where y is the normal distance to the wall, υ is the kinematic velocity, and A and B are empirical constants.

For hydraulically rough boundaries the following relation is obtained

$$\frac{u(y)}{u_*} = E \log \left(\frac{y}{K_s}\right) + D \qquad (2.2.4)$$

in which K_s is the equivalent sand grain roughness and E and D are empirical constants.

Equations (2.2.3) and (2.2.4) have been used extensively in determining the vertical velocity profile in two dimensional flows (very wide channels where side wall effects are neglected). It is assumed in these equations that the average shear velocity over the wall perimeter u_* , could be used instead of its local value. The average value is generally given as

$$u_* = \sqrt{g \; R \; S} \qquad (\textit{for open channels}) \qquad (2.2.5)$$

and

$$u_* = \sqrt{\left(-\frac{dP}{dx}\right) R} \qquad (\textit{for closed channels}) \qquad (2.2.6)$$

where R is the hydraulic radius defined as the flow area divided by the wetted perimeter, S is the longitudinal energy slope and dp/dx is the longitudinal pressure gradient driving the flow.

Another application of Equations (2.2.3) and (2.2.4) is to estimate the shear velocity and hence the boundary shear distribution along the wall perimeter by using measured or calculated values of the longitudinal velocity very near the wall and assuming that the boundary shear is constant in that short distance from the wall. Various applications of this semi-empirical approach were done by Bathurst (1979), Schamber and Larock (1981), and Naot (1984).

Experimental determination of the boundary shear is still based upon Equations (2.2.3) and (2.2.4) through the replacement of the u velocity by the dynamic pressure ($\rho\ u^2/2$) which can be measured near the bed more accurately than the velocity. This was done by Preston (1954) for smooth boundaries, and Hwang and Laursen (1963) for rough boundaries. However, the latter authors report difficulties in measuring the shear over rough boundaries. They attribute this to "inadequate knowledge of the flow near rough boundaries as what is the roughness of any particular surface, what is the correct form of the velocity distribution, and where is the zero velocity datum."

In both semi empirical and experimental approaches, the effects of the cross sectional geometry, bed roughness, and secondary motion on the boundary shear are implicitly included through the longitudinal velocity.

The difficulty in measuring the longitudinal velocity and the dynamic pressure near rough walls, especially in open channels, and the availability of powerful computers, led researchers to calculate the main velocity near the wall using mathematical models. These models solve the governing equations of turbulent flows to obtain the velocity distribution, and consequently the corresponding boundary shear distribution using one form or another of the logarithmic law of the wall.

2.3 Turbulent Flow Governing Equations:

The equations which govern the distribution of the instantaneous velocities and pressure are based upon the conservation laws for mass and momentum. These equations are expressed in tensor notation as:

Mass conservation (continuity equation)

$$\frac{\partial U_i}{\partial X_i} = 0 \tag{2.3.1}$$

and

Momentum conservation (Navier-Stokes equations):

$$\frac{\partial U_i}{\partial t} + U_j \frac{\partial U_i}{\partial X_j} = -\frac{1}{\rho} \frac{\partial P}{\partial X_i} + \nu \frac{\partial^2 U_i}{\partial X_j^2} + F_i \tag{2.3.2}$$

where U_i ($i=1,2,3$) are the instantaneous velocity components in the direction X_i, P is the instantaneous static pressure and F_i are body forces per unit mass in the X_i direction.

Equations (2.3.1) and (2.3.2) are exact, but they cannot be solved for practical turbulent flows as today computers do not have the required storage capacity and speed. Rodi (1984) reports that turbulent motion contains elements typically of the order 10^{-3} of the flow domain. This means that in three dimensional problems, at least 10^9 grid points would be necessary to cover the flow domain. Storing the flow variables at that many grid points and the tremendous number of required arithmetic operations is still far beyond present day super-computers.

To solve practical flow problems, Reynolds simplified the turbulent motion by dividing the instantaneous values into mean (time average) and fluctuating part. The period T over which the averaging process is performed is long compared with the time scale of the turbulent motion. In transient problems T is small compared with the time scale of the mean flow. Following Reynolds, the instantaneous values of the velocities U_i and the pressure P are divided into mean (time average) and fluctuating quantity as

$$U_i = \overline{U_i} + u_i \tag{2.3.3}$$

and

$$P = \overline{P} + p \; . \tag{2.3.4}$$

The time average mean quantity for the U_i velocity as an example is defined as

$$\overline{U_i} = \frac{1}{T} \int_o^T U_i \, dt \; . \tag{2.3.5}$$

The time average of single turbulent fluctuations is zero, while in general, the time average of double correlations is not zero, i.e.

$$\overline{u_i} = 0 \qquad , \qquad \overline{u_i \, u_j} \neq 0 \; . \tag{2.3.6}$$

Substituting Equations (2.3.3) and (2.3.4) into Equations (2.3.1) and (2.3.2) and performing time averaging in the way indicated by Equation (2.3.6) yields

$$\frac{\partial \overline{U_i}}{\partial X_i} = 0 \tag{2.3.7}$$

and

$$\frac{\partial \overline{U_i}}{\partial t} + \overline{U_j} \frac{\partial \overline{U_i}}{\partial X_j} = -\frac{1}{\rho} \frac{\partial \overline{P}}{\partial X_i} + \frac{\partial}{\partial X_j} (\nu \frac{\partial \overline{U_i}}{\partial X_j} - \overline{u_i u_j}) + F_i \; . \tag{2.3.8}$$

The averaging process introduces unknown double correlations between the fluctuating velocities, which when multiplied by the density ρ represent time average turbulent or Reynolds stresses τ_{ij}. Consequently Equations (2.3.8) and (2.3.7) are called the Reynolds equations of motion and continuity.

In many flow regions the turbulent stresses are larger than their laminar counterparts, $\mu\ \partial U_i / \partial X_j$, which are therefore often neglected. Equation (2.3.8) after neglecting the laminar stresses and expressing the velocity correlations in terms of the turbulent stresses becomes

$$\frac{\partial \overline{U_i}}{\partial t} + \overline{U_j}\frac{\partial \overline{U_i}}{\partial X_j} = -\frac{\partial}{\partial X_i}(\frac{\overline{P}}{\rho}) + \frac{\partial}{\partial X_j}(\frac{\overline{\tau_{ij}}}{\rho}) + F_i\ . \tag{2.3.9}$$

From here forward the over-bar is omitted when expressing time average quantities with upper case letters expressing time averages and lower case letters expressing fluctuating quantities.

The expanded form of the Reynolds equations of motion and continuity for steady, incompressible, fully developed, and high Reynolds number flow, is written as:

- Mass conservation (The continuity equation)

$$\frac{\partial V}{\partial Y} + \frac{\partial W}{\partial Z} = 0 \tag{2.3.10}$$

- Momentum conservation (The Reynolds equations of motion):

X direction or the longitudinal flow direction

$$V\frac{\partial U}{\partial Y} + W\frac{\partial U}{\partial Z} = -\frac{d}{dx}(\frac{P}{\rho}) + \frac{\partial}{\partial Y}(\frac{\tau_{yx}}{\rho}) + \frac{\partial}{\partial Z}(\frac{\tau_{zx}}{\rho}) + F_x \tag{2.3.11}$$

Y direction or the vertical direction

$$V\frac{\partial V}{\partial Y} + W\frac{\partial V}{\partial Z} = -\frac{\partial}{\partial Y}(\frac{P}{\rho}) + \frac{\partial}{\partial Y}(\frac{\tau_{yy}}{\rho}) + \frac{\partial}{\partial Z}(\frac{\tau_{zy}}{\rho}) + F_y \tag{2.3.12}$$

and

Z direction or the transverse direction

$$V\frac{\partial W}{\partial Y} + W\frac{\partial W}{\partial Z} = -\frac{\partial}{\partial Z}(\frac{P}{\rho}) + \frac{\partial}{\partial Y}(\frac{\tau_{yz}}{\rho}) + \frac{\partial}{\partial Z}(\frac{\tau_{zz}}{\rho}) + F_z \tag{2.3.13}$$

where U,V,W are the time average mean velocities in the X,Y,Z directions respectively, Fig 2.1, P is the time average mean pressure, the τ's are turbulent (Reynolds) stresses and the F's are body forces. The turbulent stresses are symmetrical: i.e., $\tau_{ij} = \tau_{ji}$.

As the viscous stress terms are neglected, the equations are not applicable very near the channel walls in the viscous sublayer where viscous effects play a dominant role. Turbulence modelling is the subject of finding the turbulent stresses by usually relating them to mean flow quantities to close the system of equations.

2.4 Linear Eddy Viscosity Model:

The turbulent stresses appearing in the Reynolds equations of motion are usually unknown and should be determined to close the system of equations. One form of closure is the Boussinesq's (1877) approximation which is still widely used in many fluid flow problems. It is called the linear eddy viscosity turbulence model and is expressed in tensor notation as

$$\tau_{ij} = \nu_T (\frac{\partial U_i}{\partial X_j} + \frac{\partial U_j}{\partial X_i}) - \frac{2}{3} K \delta_{ij} \tag{2.4.1}$$

and

$$\nu_T = C_\mu \frac{K^2}{\epsilon} \tag{2.4.2}$$

where

δ_{ij} = Kroneker's delta

= 1 (i = j)

= 0 (i $\neq$ j),

ν_T = the turbulent eddy viscosity,

C_μ = a non-dimensional constant with standard value equal to 0.09,

ϵ = the dissipation rate of the turbulent kinetic energy, and

K = the turbulent kinetic energy per unit mass defined as

$$K = \frac{1}{2} (\overline{u}^2 + \overline{v}^2 + \overline{w}^2) . \tag{2.4.3}$$

The turbulent kinetic energy is a positive quantity (the realizability constraint) as seen from Equation (2.4.3).

2.5 Origin of Secondary Motions:

The secondary motions (V and W velocities) in a straight channel under steady and fully developed flow conditions are governed by the momentum equations as in Equations (2.3.12) and (2.3.13). After operating on these two equations to eliminate the pressure, an equation for the stream-wise component of the vorticity (Ω) is obtained. Following Einstein and Li (1958), the equation is expressed as

$$\left(V \frac{\partial \Omega}{\partial Y} + W \frac{\partial \Omega}{\partial Z}\right) = \frac{\partial^2}{\partial Y \partial Z}(\tau_{yy} - \tau_{zz}) + \left(\frac{\partial^2}{\partial Z^2} - \frac{\partial^2}{\partial Y^2}\right)\tau_{yz} + \mu \nabla^2 \Omega \tag{2.5.1}$$

in which

$$\Omega = \frac{\partial W}{\partial Y} - \frac{\partial V}{\partial Z} \qquad (2.5.2)$$

and

$$\tau_{yy} = -\rho\ \overline{v^2} \quad , \tau_{zz} = -\rho\ \overline{w^2} \quad , \tau_{yz} = -\rho\overline{vw}\ . \qquad (2.5.3)$$

In Equation (2.5.3) u, v, w are velocity fluctuations in the X, Y, Z directions, respectively.

Equation (2.5.1) exactly governs the secondary motion in the cross sectional plane (YZ plane). The primary U velocity does not appear directly in the equation, however the U velocity affects the turbulent shear stresses which in turn affect the vorticity. The two terms on the left hand side of Equation (2.5.1) represent the existence of secondary motion and convection of longitudinal vorticity by secondary motions. The first term on the right hand side represents generation of secondary motion by the anisotropy of the normal turbulent stresses. The second term on the right side represents dissipation of secondary motion by the turbulent shear stress. The last term on the right side represents the viscous dissipation which is negligible except very near the wall regions.

Nezu and Nakayama (1984) show experimentally that the first two terms on the right side of Equation (2.5.1) are the dominant ones in controlling secondary motions.

It is clear from Equation (2.5.1) that in laminar flows, where the turbulent stresses are identically zero, secondary motions do not exist. In regions where the anisotropy of the turbulent stresses is non-zero, such as at channel walls and free surfaces, secondary motions are present. Thus, any turbulence model predicting secondary motion should predict the anisotropy of the turbulent stresses correctly.

Unfortunately, the linear eddy viscosity model given by Equation (2.4.1) is fundamentally incapable of predicting secondary motions as shown by Speziale (1987). This is seen by expanding Equation (2.4.1) for the turbulent stresses while dropping terms containing the secondary velocities as they are an effect of the turbulent stresses rather than a cause:

$$\tau_{yy} = -\frac{2}{3} \rho K \tag{2.5.4}$$

$$\tau_{zz} = -\frac{2}{3} \rho K \tag{2.5.5}$$

$$\tau_{yx} = \rho \nu_T \frac{\partial U}{\partial Y} \tag{2.5.6}$$

$$\tau_{zx} = \rho \nu_T \frac{\partial U}{\partial z} \tag{2.5.7}$$

$$\tau_{yz} = 0 . \tag{2.5.8}$$

Equations (2.5.4), (2.5.5), and (2.5.8) show that the normal stress difference (τ_{yy} - τ_{zz}) and the shear stress τ_{yz} are zero, and hence no secondary motion is predicted when using the linear eddy viscosity model. Models capable of predicting secondary motions are reviewed in Section (2.7).

2.6 Measurements of Secondary Motions:

Measurements of turbulence-driven secondary velocities are difficult as their magnitude is often less than 5 percent of the primary velocity. In the early stages, hot-wire anemometers were used to measure the secondary motions. However the results are affected by the difficulty of determining the direction of secondary motion and by flow interference from the probe.

Experimenters consider the satisfaction of the continuity equation as an indication to the error in measuring the secondary velocities. Data collected by Gessner and Jones (1965) in air ducts show that flow away from the wall is about 20 percent greater than flow towards it, on all profiles. Launder and Ying (1973) found that at Z/H=0.2 and 0.5, the error is about 10%, but at Z/H=0.8 the flow away from the wall is five times as large as the flow toward the wall.

Based upon measurements of duct flows using laser-Doppler anemometry, Melling and Whitelaw (1976) report that the error in determining the secondary velocities arise from the small difference between two comparatively large frequencies. The results are very sensitive to a small change in the orientation of the fringe pattern, even if frequency-shifting is employed. The anemometer can detect a small part of the streamwise component of velocity. Since this component is typically 100 times greater than the secondary velocities, measurements of the latter will be significantly in error. It should be noted that Melling and Whitelaw measurements were not performed at fully developed conditions, as seen from their rather unsymmetrical secondary velocity data.

Nezu and Rodi (1985) used a Laser Doppler Anemometer (LDA) to measure secondary motions in smooth walled open channels. They report having difficulty in measuring the spanwise velocity component by LDA, as the side wall is not perfectly transparent due to side wall roughness and the side wall inclination.

Tominaga et al. (1989), used a hot-film anemometer for measuring all three components of the velocity in open channels. Their results are questionable as measurements were taken before the flow became fully developed. For example, a test section was 7.5 m downstream from the entrance of the channel with flow depths of about 20 cm. The ratio L/H becomes 37.5 which is not considered sufficient for obtaining fully developed conditions.

In natural channels and rivers, the presence of suspended sediments increases the difficulty of measuring the secondary velocities as reported by Nezu et al. (1993).

From the foregoing discussion, it is clear that measurements of secondary motions only provide qualitative information about the pattern of the secondary velocities and the order of their magnitude. This has led many researchers to calculating the secondary velocities using the governing equations of turbulent flows. This is illustrated in Section (2.7).

2.7 Prediction of Secondary Motions:

Rather than trying to measure the secondary velocities, a different and perhaps better approach is to solve the Reynolds equations of motion and continuity. The turbulent stresses appearing in these equations are often expressed in non-linear algebraic stress relations. The eddy viscosity, expressed by Equation (2.4.2), often appears in these relations. Researchers often use the two equation model (K-ϵ) to determine the turbulent viscosity.

Although researchers often use the K-ϵ model for evaluating the eddy viscosity, they take different approaches for expressing the turbulent stresses.

Naot et al. (1974), use differential transport equations for all the turbulent stresses and apply them to fully-developed square channel flow. Reece (1976) uses the full stress equations in closed channels under both developed and developing conditions and in developed open channel flow. Reece predicts the depression of the velocity maximum below the free surface for a narrow channel. This is also in agreement with Nikuradse's measurements.

While differential stress transport equations are adequate and conceptually more accurate for obtaining the turbulent stresses, they are not economical due to the increasing number of differential equations. In addition, more model assumptions are required to express higher order correlations (triple velocity fluctuations) which are experimentally difficult to verify. Hence researchers simplify these differential stress equations to simpler and more economical algebraic equations known as algebraic stress models.

Launder and Ying (1973) were the first to calculate the secondary motions in developed channel flow using an algebraic stress model. They simplified the stress transport model of Hanjalic and Launder (1972) by neglecting the convection and diffusion terms (assumption of local equilibrium between the production and dissipation terms) and by further neglecting all secondary velocity gradients. The algebraic stress model is given as:

$$\tau_{yy} = C_3 \, \rho \, K - C_2 \, \mu_T \left(\frac{K}{\epsilon}\right)\left(\frac{\partial U}{\partial Y}\right)^2 \tag{2.7.1}$$

$$\tau_{zz} = C_3 \, \rho \, K - C_2 \, \mu_T \left(\frac{K}{\epsilon}\right)\left(\frac{\partial U}{\partial Z}\right)^2 \tag{2.7.2}$$

$$\tau_{yz} = C_2 \, \mu_T \left(\frac{K}{\epsilon}\right)\left(\frac{\partial U}{\partial Y}\right)\left(\frac{\partial U}{\partial Z}\right) \tag{2.7.3}$$

where C_2 and C_3 are empirical constants. The primary shear stresses τ_{xy} and τ_{xz} are calculated from the standard eddy viscosity model as given by Equations (2.5.6) and (2.5.7). The turbulent eddy viscosity is expressed in terms of the turbulent kinetic energy K, and the length scale l, as

$$\nu_T = C\, l\, K^{\frac{1}{2}} . \tag{2.7.4}$$

The turbulent kinetic energy is obtained by solving its transport equation, and the length scale is determined from the algebraic geometrical formula of Buleev (1963). The model is used by Tatchell (1975) while replacing the length scale formula by a transport equation for the dissipation rate (ϵ) which makes the model more general. The same model is used by Ramachandra (1979) and Gosman and Rapley (1980), to calculate fully developed flows in square ducts, triangular ducts, and ducts with arbitrary cross sections.

In all applications of Launder and Ying's (1973) model along with its modifications, the level of the secondary motion is correctly predicted but for the wrong reason. Kacker (1973) found the Launder and Ying's (1973) model predicts the separation between the two normal stresses τ_{yy}-τ_{zz}, which drives the secondary motion, to be too small by a factor of roughly 10 which is compensated by adjusting the constants C_2 and C_3 and by neglecting the secondary velocity gradients in the algebraic stress relations. Demuren and Rodi (1984) state that the contribution of secondary velocity gradients, neglected in Launder and Ying's (1973) model, is very significant.

Naot and Rodi (1982) simplified the Reynolds-stress equation model of Launder et al. (1975), to an algebraic stress model. Their algebraic stress relations are given as:

$$\frac{\tau_{yx}}{\rho} = \nu_{TY} \frac{\partial U}{\partial Y} \tag{2.7.5}$$

$$\nu_{TY} = \frac{C_1^{\,2}}{(C_1 + \frac{3}{2}C_3)(C_1 + 2C_3)}\, \nu_T \tag{2.7.6}$$

$$\nu_T = C_\mu \frac{K^2}{\epsilon} \tag{2.7.7}$$

$$\frac{\tau_{zx}}{\rho} = \nu_{TZ} \frac{\partial U}{\partial Z} \tag{2.7.8}$$

$$\nu_{TZ} = \frac{(c_1 + \frac{5}{2} C_3)}{(C_1 + 2\ C_3)} \nu_T \tag{2.7.9}$$

$$\begin{aligned} \frac{\tau_{yy}}{\rho} = & -\frac{K}{(C_1+2\ C_3)}[\frac{2}{3}(\alpha-\frac{1}{2}\beta+C_1-1) \\ & +\frac{\beta}{\epsilon}(-\frac{\tau_{yx}}{\rho}\frac{\partial U}{\partial Y}+\frac{\tau_{zx}}{\rho}\frac{\partial U}{\partial Z})] \\ & +2\ \nu_T \frac{\partial V}{\partial Y} \end{aligned} \tag{2.7.10}$$

$$\begin{aligned} \frac{\tau_{zz}}{\rho} = & -\frac{K}{C_1}[\frac{2}{3}(\alpha-\frac{1}{2}\beta+C_1-1) \\ & +\frac{\beta}{\epsilon}(-\frac{\tau_{zx}}{\rho}\frac{\partial U}{\partial Z}+\frac{\tau_{yx}}{\rho}\frac{\partial U}{\partial Y})-C_3\frac{\tau_{yy}}{\rho\ K}] \\ & +2\ \nu_T \frac{\partial W}{\partial Z} \end{aligned} \tag{2.7.11}$$

$$\begin{aligned} \frac{\tau_{yz}}{\rho} = & -\frac{\beta}{(C_1+\frac{3}{2}C_3)}\frac{K}{\epsilon}(-\frac{\tau_{zx}}{\rho}\frac{\partial U}{\partial Y}-\frac{\tau_{yx}}{\rho}\frac{\partial U}{\partial Z}) \\ & +\nu_T(\frac{\partial W}{\partial Y}+\frac{\partial V}{\partial Z})\ . \end{aligned} \tag{2.7.12}$$

To express the effect of approaching a boundary, the model coefficients are given in terms of two functions accounting for the distance from solid walls (f_1) and open surfaces (f_2) given by :

$$\alpha = 0.7636 - 0.06 f_1 \tag{2.7.13}$$

$$\beta = 0.1091 + 0.06 f_1 \tag{2.7.14}$$

$$C_1 = 1.5 - 0.5 f_1 \quad , \quad C_3 = 0.1 f_2 \tag{2.7.15}$$

Naot and Rodi (1982) suggest the use of quadratic formulas for f_1 and f_2 rather than linear formulas. The quadratic formulas are given as:

$$f_1 = (\frac{l}{y_a})^2 \quad and \quad f_2 = (\frac{l}{h_a})^2 \tag{2.7.16}$$

where l is the dissipation length scale defined in this case as

$$l = (\frac{C_\mu}{\kappa}) \frac{K^{3/2}}{\epsilon} \tag{2.7.17}$$

and y_a, and h_a are average distances from solid walls and open surface, respectively, and κ is the Von Karman constant taken as 0.42 in open channels.

The functions f_1 and f_2 are taken equal to 1.0 adjacent to the surfaces, since $l \sim y$ near solid walls and l is finite near free surfaces. Both functions vanish away from the surfaces due to the quadratic formula. However, the dependence of the two functions upon the mixing length, which is generally unknown and should be determined in the iteration process, can cause values greater than one for either functions.

Naot and Rodi found that by neglecting the secondary velocity gradients, the secondary motion grows without bounds and no stable solution could be found. They used the Spalding-Patankar algorithm for solving the governing equations which uses the finite difference method. Some doubt is put on these methods because difference methods use upwinding which yields smooth solutions that are not necessarily true. In addition, it is not clear how the authors overcome convergence problems, especially with the K-ϵ model. They took the two constants: $\sigma_K = 1.225$ and $\sigma_\epsilon = 1.225$ while their standard values are 1.0 and 1.3, respectively. This was case specific to compensate for upwinding and other uncertainties.

However, their model simulates most features of secondary motions including bulging of main velocity contours to the corners in square ducts, depression of the velocity maximum below the free surface, and reduction of the eddy viscosity near the free surface. Yet, the secondary motion is over predicted which results in increasing bulging of the primary velocity contours.

Naot (1984) applies the same model to open channel flows with bed and side wall roughness heterogeneity. He simulates the experiments of Muller and Studerus (1979) for a single cell in a wide open channel with periodic roughness steps. The cellular pattern of the secondary motion is predicted correctly, with the secondary flow moving down over the rough part and up over the smooth part. Primary velocity over the rough strip is well simulated, but over the smooth strip is under predicted due to over prediction of the secondary flow over that part. Also, the kinetic energy is under predicted over both the smooth and rough stripes.

Demuren and Rodi (1984) modified Naot and Rodi's (1982) model by retaining the secondary velocity gradients in the algebraic stress relations. They believe this reduces the over prediction of the secondary velocities existing in the latter model. However they under predicted the secondary velocities.

Krishnappen and Lau (1986) try to model the flow in an open channel with flood plain. They use the algebraic stress relations of Thatchell which are based upon Launder and Ying's (1973) model of duct flows and not suitable for open channels. They do not completely include the free surface effects on the turbulent stresses or eddy viscosity, but only modified the free surface boundary condition for ϵ. They do not provide their secondary velocities or K and ϵ calculation.

Speziale (1987) introduces a non-linear K-ϵ turbulence model for closed channels which is a form of an algebraic stress model. This model has the advantage of satisfying the realizability and invariance requirements. The model is based upon similarities between the mean turbulent flow of a Newtonian fluid and the laminar flow of viscoelastic fluids. The model relations are given as:

$$\frac{\tau_{yy}}{\rho} = -\frac{2}{3}K + l^2 \left[\left(\frac{C_E}{3} + \frac{C_D}{12}\right)\left(\frac{\partial U}{\partial Y}\right)^2 + \left(\frac{C_E}{3} - \frac{C_D}{6}\right)\left(\frac{\partial U}{\partial Z}\right)^2\right] + 2\,\nu_T \frac{\partial V}{\partial Y} \tag{2.7.18}$$

$$\frac{\tau_{zz}}{\rho} = -\frac{2}{3}K + l^2 \left[\left(\frac{C_E}{3} + \frac{C_D}{12}\right)\left(\frac{\partial U}{\partial Z}\right)^2 + \left(\frac{C_E}{3} - \frac{C_D}{6}\right)\left(\frac{\partial U}{\partial Y}\right)^2\right] + 2\,\nu_T \frac{\partial W}{\partial Z} \tag{2.7.19}$$

$$\frac{\tau_{zx}}{\rho} = \frac{1}{2}\, K^{\frac{1}{2}}\, l\, \frac{\partial U}{\partial Z} \tag{2.7.20}$$

$$\frac{\tau_{yx}}{\rho} = \frac{1}{2}\, K^{\frac{1}{2}}\, l\, \frac{\partial U}{\partial Y} \tag{2.7.21}$$

$$\frac{\tau_{yz}}{\rho} = \frac{1}{4}\, C_D\, l^2 \left(\frac{\partial U}{\partial Z}\right)\left(\frac{\partial U}{\partial Y}\right) . \tag{2.7.22}$$

The form Speziale uses for the length scale l, is given as

$$l = 2\, C_\mu\, \frac{K^{3/2}}{\epsilon} . \tag{2.7.23}$$

The dimensionless constants C_E and C_D are both taken by Speziale as 1.68 based upon turbulent channel data. Equations (2.7.18), (2.7.19), and (2.7.22) indicate that $(\tau_{yy}-\tau_{zz})$ and τ_{yz} are generally not vanishing, and the secondary motion can be generated.

Speziale uses an experimentally determined eddy viscosity distribution and successfully predicts the eight vortex pattern in square ducts. However, he does not give quantitative results about the magnitude of the secondary velocities and their effects upon primary flow and boundary shear distributions.

Naot et al. (1993), investigate the flow in compound rectangular open channels using the same algebraic stress relations as used in Naot and Rodi's (1982) model, but with a different free surface boundary condition for ϵ. The pattern of primary and secondary velocities, including the vortex pair at the flood plain and the main channel intersection, agree with their experimental data. However, they report under prediction of the turbulent kinetic energy and friction factor.

In summary, algebraic stress turbulence models are capable of predicting turbulence-driven secondary motions, primary velocity, and turbulent eddy viscosity. These models are more economical than differential stress transport equations and are sufficient for many engineering flow problems. Nevertheless, all of the models developed to date use the finite difference method along with calibration of certain constants. The finite element method has not been tested in predicting primary and secondary velocities associated with algebraic stress models and K-ϵ turbulence models.

2.8 K-ϵ Turbulence Model:

The turbulent eddy viscosity is used in various turbulence models as mentioned before in the isotropic eddy viscosity model, Naot and Rodi's (1982) algebraic stress model, and Speziale's (1987) non-linear model. The turbulent viscosity is related to the turbulent kinetic energy and dissipation rate of the kinetic energy as seen in Equation (2.4.2). The two equation K-ϵ turbulence model is used extensively to determine the K and ϵ quantities by solving their differential transport equations. So far, the K-ϵ model has been the most popular one in practical fluid flow problems. For example, Keller and

Rastogi (1975) modeled flow over spillways, Svensson (1978) investigated wind-induced channel flow, Leschziner and Rodi (1979) studied flow in a strongly curved open channel bend, Celik and Rodi (1989) studied suspended sediment transport in non-equilibrium situations, Finnie and Jeppson (1991) studied flow under a sluice gate, Yacoub et al. (1992) modeled flow behind the slug front, and all models predicting the secondary motion discussed in Section 2.7 are using this model as well.

The popularity of the K-ϵ model stems from its universality and economics in terms of computer time and memory.

The K-ϵ transport equations for steady, fully developed, high Reynolds number flow are given as:

- Turbulent kinetic energy transport equation (K)

$$\begin{aligned} V\frac{\partial K}{\partial Y}+W\frac{\partial K}{\partial Z}&=\frac{\partial}{\partial Y}\left(\frac{\nu_T}{\sigma_K}\frac{\partial K}{\partial Y}\right)+\frac{\partial}{\partial Z}\left(\frac{\nu_T}{\sigma_K}\frac{\partial K}{\partial Z}\right)\\ &\quad+\nu_T\left[\left(\frac{\partial U}{\partial Y}\right)^2+\left(\frac{\partial U}{\partial Z}\right)^2\right]-\epsilon \end{aligned} \tag{2.8.1}$$

and

- Dissipation rate of the turbulent kinetic energy (ϵ)

$$\begin{aligned} V\frac{\partial \epsilon}{\partial Y}+W\frac{\partial \epsilon}{\partial Z}&=\frac{\partial}{\partial Y}\left(\frac{\nu_T}{\sigma_\epsilon}\frac{\partial \epsilon}{\partial Y}\right)+\frac{\partial}{\partial Z}\left(\frac{\nu_T}{\sigma_\epsilon}\frac{\partial \epsilon}{\partial Z}\right)\\ &\quad+C_{\epsilon 1}C_\mu K\left[\left(\frac{\partial U}{\partial Y}\right)^2+\left(\frac{\partial U}{\partial Z}\right)^2\right]-C_{\epsilon 2}\frac{\epsilon}{K}\epsilon \end{aligned} \tag{2.8.2}$$

where σ_K, σ_ϵ, $C_{\epsilon 1}$, and $C_{\epsilon 2}$ are dimensionless constants determined from experiments. Rodi (1984) reports their standard values as 1.0, 1.3, 1.44, and 1.92, respectively.

In Equations (2.8.1) and (2.8.2) the left side terms represent convection by secondary motion, the first two terms on the right side represent diffusion terms, and the last two terms represent production and dissipation terms. Initial values for the three velocity components, K, and ϵ are required for solving the two quantities K and ϵ.

Schamber and Larock (1981) suggest solving the Reynolds equations of motions and continuity assuming the turbulent viscosity is known and then solving the K-ϵ equations to obtain a new turbulent viscosity. The process is repeated until convergence is achieved and all variables become compatible.

2.9 Boundary Conditions of Turbulent Flow Problems:

Boundary conditions are generally required to satisfy physical constraints on the boundaries, and to insure uniqueness of the solution. Since the governing equations are of elliptic type, boundary conditions for all variables are required along the exterior boundaries of the domain (i.e., along solid walls, free surfaces, and planes of symmetry). These different boundary conditions are discussed separately in the following sections.

2.9.1 Wall Boundary Conditions:

As most turbulence models were developed for high Reynolds number flows in which viscous effects are negligible, researchers apply their models outside the viscous sublayer. This makes the computational mesh economical and avoids the steep velocity gradients very near the walls.

To avoid the viscous sublayer, Launder and Spalding (1974) suggest the wall function approach. In this approach, the boundary conditions are specified at a distance away from the wall outside the viscous sublayer. This distance Y, normalized by kinematic viscosity υ, and longitudinal shear velocity u_* , is often taken (Rodi 1984) as

$$30 \le \frac{Y u_*}{\nu} \le 100 \ . \qquad (2.9.1.1)$$

Boundary conditions are required for the turbulent stresses on the boundaries in the Reynolds equations of motion. The shear stresses can be expressed in terms of velocities and velocities can be specified instead. For example, as the primary shear stress and the primary velocity are related through the logarithmic law of the wall, either of them can be specified as the boundary condition for the X equation.

For the X-equation, Schamber and Larock (1981) specify in their model the primary shear stress at the virtual walls in terms of the main velocity as

$$\frac{\tau}{\rho} = -u_* |u_*| = \frac{-\kappa^2}{[\ln E \frac{y u_*}{\nu}]^2} |U| U \ . \qquad (2.9.1.2)$$

Naot and Rodi (1982) specify in their model for smooth channels the main velocity U, instead of specifying the shear, at a distance y from the wall through the logarithmic law of the wall. They did not mention what value they used for the shear velocity.

As Naot (1984) investigated smooth and rough channels, he expressed the primary shear in terms of the U velocity via the logarithmic law of the wall in an iterative manner. The U velocity is calculated from the logarithmic law assuming the shear velocity is known. After obtaining a new U from solving the governing equation, the shear velocity is updated using

$$u_* = \frac{\kappa U}{\ln(E \frac{Y u_*}{\nu})} \qquad (2.9.1.3)$$

and the iteration process continues in that manner.

Naot uses E = 9.0 for smooth walls, and for completely rough walls uses

$$E = \frac{e^{\kappa B}}{(K_s \frac{u_*}{\nu})} \tag{2.9.1.4}$$

in which B=8.5, and K_s is the roughness height. In the transition between the smooth and rough regimes, E is taken according to the Naot and Emrani (1983) formula which is given as:

$$E = 9/(1 + [\frac{0.3\ K_s^+}{1+(20/K_s^+)}]) \tag{2.9.1.5}$$

$$and \quad K_s^+ = \frac{K_s\ u_*}{\nu} . \tag{2.9.1.6}$$

An expression for the entire turbulent regime developed by Yalin and used through private communication by Krishnappan and Lau (1986) in their turbulence model was given as:

$$E = \frac{e^{\kappa B_s}}{(\frac{u_*\ K_s}{\nu})} \tag{2.9.1.7}$$

in which

$$\begin{aligned} B_s = & [5.5+2.5 \ln R] \exp\{-0.217 (\ln R)^2\} \\ & +8.5 (1-\exp\{-0.217 (\ln R)^2\} \end{aligned} \tag{2.9.1.8}$$

$$and \quad R = (\frac{u_*\ K_s}{\nu}) . \tag{2.9.1.9}$$

For the Z and Y equations, Naot and Rodi (1982) use the form

$$U_l = U \sin \phi \left(1 - \frac{y}{L}\right) \tag{2.9.1.10}$$

in which U_l is the lateral velocity, ϕ is the angle between the resultant shear velocity and X direction, and L is a length determined from lateral velocities. Naot and Rodi report that using a different law for the lateral velocity has little overall influence on the calculations. The boundary condition for the velocity normal to the wall is taken as zero by Schamber and Larock (1981), Naot and Rodi (1982), Naot (1984) and Naot et al. (1993). Thus, stresses normal to the wall do not need to be specified.

Wall boundary conditions for K and ϵ are based upon the assumption of local equilibrium (Rodi 1984) where the convection and diffusion terms are small and the production of K is equal to its rate of dissipation ϵ. Under these assumptions, the boundary conditions for K and ϵ at the walls are:

$$K = \frac{u_*^2}{\sqrt{C_\mu}} \tag{2.9.1.11}$$

and

$$\epsilon = \frac{u_*^3}{\kappa\, y} \tag{2.9.1.12}$$

2.9.2 Symmetry Plane Boundary Conditions:

At planes of symmetry, the velocity component normal to the symmetry plane is zero. Hence the normal stress need not be specified at symmetry planes. Also, tangential stresses are zeros at symmetry planes. For all other variables, the normal gradient to the symmetry plane is taken as zero by Naot and Rodi (1982), and Finnie and Jeppson (1991).

2.9.3 Free Surface Boundary Conditions:

Researchers agree that the free surface behaves like a plane of symmetry for all variables except for dissipation rate ϵ. Naot and Rodi (1982) report that the free surface reduces the length scale and hence increases the dissipation rate. Naot and Rodi follow Hossain (1980) by assuming that the length scale has a virtual origin with distance $y^{\backslash}$ above the free surface, and is proportional to the distance from this origin. Thus, their surface boundary condition for ϵ is given as

$$\epsilon = \frac{C_{\mu}^{3/4}}{\kappa} K_s^{3/2} \left(\frac{1}{y^{\backslash}} + \frac{1}{y^{*}}\right) \qquad (2.9.3.1)$$

in which y^* is the average distance from the nearest wall included to ensure a smooth transition between the wall boundary condition in Equation (2.9.1.12), and the surface boundary condition in Equation (2.9.3.1). Hossain (1980) determines $y\backslash$ to be 0.07 times the channel depth H. This tentative surface boundary condition for ϵ is not based upon physical considerations.

Yacoub et al. (1992), develops a surface boundary condition for ϵ based upon physical considerations which has the form of a gradient boundary condition as

$$\frac{d\epsilon}{dX_n} = C_{\epsilon F} \frac{\epsilon^2}{K^{3/2}} \qquad (2.9.3.2)$$

where $C_{\epsilon F} = 3.5$ according to Ueda et al. (1977) data, while $C_{\epsilon F} = 2.43$ is equivalent to applying Equation (2.9.3.1). This natural boundary condition has the advantage of being suitable for finite element formulations. As Equation (2.9.3.2) does not depend upon the local flow depth, Naot et al. (1993), use it in their flood plain channels in which the depth varies over the cross section.

2.10 Finite Element Method for Turbulent Flow Problems:

Early turbulence models were in general developed using the finite difference method. With respect to turbulence-driven secondary motion, all models have used the finite difference method including the work by Gosman and Rapley (1980), Naot and Rodi (1982), Naot (1984), and Naot et al. (1993). Finite difference methods employ upwinding techniques which weight the value of the variable at the upstream node more than at the downstream node.

Finnie and Jeppson (1991) report that upwinding creates a truncation error that dampens oscillations in the solution and results in convergence to a solution that may not occur otherwise. This results in terms that have diffusive characteristics, and hence upwinding is said to produce false diffusion of turbulence. Gresho and Lee (1981) discourage the use of upwinding techniques as they tend to smoothen the solution, giving false impression of solution stability, and hiding numerical problems caused by coarse grids. Gresho and Lee suggested using smaller elements in regions where oscillations occur. Another problem with the finite difference method is its difficulty in handling certain boundary conditions and irregularly shaped flow fields.

The finite element method is popular in turbulence modelling because of its ability of handling complex geometry flow domains, and the ease in which boundary conditions are handled. Upwinding techniques are not necessary when using the finite element method as smaller elements can be easily added in regions where oscillations occur.

Many researchers use the finite element method to solve different turbulent flow problems. For example: Schamber and Larock (1981) investigated the flow in sedimentation tanks, Devantier and Larock (1986) added a suspended sediment component, Taylor et al. (1981), and Autret et al. (1987) modeled the flow over a backward step, Sharma and Carey (1986) studied heat transfer in a boundary layer, and Finnie and Jeppson (1991) modelled flow under a sluice gate.

In spite of the availability of many turbulence models suitable for every particular problem, the convergence of the K-ϵ transport equations is still difficult to obtain. This is due to the high non-linearity of the K-ϵ transport equations in which the solution becomes very sensitive to initial starting values.

Smith (1984a) illustrates the difficulty of solving the K-ϵ equations by obtaining different solutions for a simple diffusion problem with the same boundary conditions but with a different starting values. He concludes that, unless the initial estimates of K and ϵ are very close to the correct values, the solution may converge to physically incorrect results, including negative values. Hutton et al. (1987), describe the cause of these physically incorrect negative values as follows. The production term in the K equation P_K is given as

$$P_K = \nu_T \{ (\frac{\partial U}{\partial Y})^2 + (\frac{\partial U}{\partial Z})^2 \} . \tag{2.10.1}$$

If the production term in the K equation is large, this produces steep gradients of K and ϵ. If the finite element grid is too coarse, the variables oscillate during the calculations, which leads to negative values. Subsequent iterations spread the negative values until the solution diverges. Hutton et al. recommend using false diffusion and/or smoother resolution of the production term P_K so that local peaks are reduced.

Researchers take different approaches to overcome the convergence problem of the K-ϵ turbulence model. Schamber and Larock (1981) use a modified form of Newton's method where υ_T and the ratio ϵ/K are held constant in the Jacobian matrix of the K-ϵ equations. They claim that the modified scheme and underrelaxation are required to prevent K and ϵ from becoming negative. Tong (1982) adds false diffusion by taking σ_K and σ_ϵ equal to 0.5, while Polansky et al. (1984), add artificial viscosity.

Smith (1984b) proposes using the variables q and f instead of K and ϵ, where $q=\sqrt{K}$ and f is a measure of the frequency of large-scale turbulent eddies. When certain assumptions are made, the q-f model can be equivalent to the K-ϵ model with $q=\sqrt{K}$ and $f=\epsilon/k$. Devantier and Larock (1986) remove some of the non-linear parts of the K and ϵ equations and add them back in as calculations progress. Finnie and Jeppson (1991) use the q-r ($q=\sqrt{K}$ and $r=\sqrt{\epsilon}$) variable substitution in the K-ϵ model, which is a simplification of the q-f model of Smith (1984b). To obtain a convergence, they use overrelaxation during the Newton-Raphson iteration, addition and slow removal of artificial diffusion, and uniform production of the turbulent kinetic energy within each element. It should be noted that most of these techniques lack generality and are case specific.

Other researchers use finite element upwinding to prevent divergence of calculations. For example: Magnaud and Goldstein (1989), who modeled thermally stratified flow in a pressure vessel, and Haroutunian and Engelman (1989), who modeled air circulation in the Sistine Chapel.

Despite all the foregoing difficulties, the K-ϵ two equation model is still considered by many researchers to be a very powerful tool in solving practical turbulent flow problems.

CHAPTER III

THE MATHEMATICAL MODEL

Since the availability of large computers, researchers have had the ability to solve problems numerically that have not previously been possible to solve analytically. Such problems have included the Reynolds equations of motion and continuity for turbulent flows. Both the finite difference and the finite element methods are often used to obtain numerical solutions in this category.

The finite element method has the advantages that it easily allows the use of non-rectangular grids, the ability to refine the mesh during a simulation, and the approximation of geometrically complex boundaries and boundary conditions. For these reasons, the finite element method is used in this study to solve the set of governing equations that describe mean turbulent flows in closed and open channels.

The mathematical model for turbulent flows developed in this chapter will be used to investigate the following:

(1) the three-dimensional turbulent velocity structure, which includes the primary velocity and the secondary velocities;

(2) the boundary shear stress distribution;

(3) the turbulent viscosity;

(4) the effect of the geometry of the cross section on the flow field;

(5) the wall roughness effects on the flow field.

The investigation is limited to:

(1) the use of finite element analyses;

(2) incompressible, steady, fully developed, and high Reynolds number turbulent flows;

(3) two dimensional domain, which is the flow cross section outside the viscous sublayer;

(4) closed and open channels which are straight and rectangular;

(5) free surfaces which are treated as rigid lids;

(6) $K - \epsilon$ turbulence model;

(7) large scale turbulent eddies that are determined by the boundary conditions of the flow.

3.1 Summary of the Governing Equations and Boundary Conditions for the Mathematical Model:

In this section the governing equations and boundary conditions that constitute the mathematical model for mean turbulent flows are given. Most of the equations were given in Chapter II along with the definition for all variables.

The Reynolds equations of motion and continuity constitute the governing equations for the mean turbulent flow considered in this study. These equations for incompressible, steady, fully developed, and high Reynolds number turbulent flow are:

the continuity equation

$$\frac{\partial V}{\partial Y} + \frac{\partial W}{\partial Z} = 0 \tag{3.1.1}$$

the Reynolds equations of motion:

X direction or the longitudinal flow direction

$$V\frac{\partial U}{\partial Y} + W\frac{\partial U}{\partial Z} = -\frac{d}{dx}(\frac{P}{\rho}) + \frac{\partial}{\partial Y}(\frac{\tau_{yx}}{\rho}) + \frac{\partial}{\partial Z}(\frac{\tau_{zx}}{\rho}) + F_x \tag{3.1.2}$$

Y direction or the vertical direction

$$V\frac{\partial V}{\partial Y} + W\frac{\partial V}{\partial Z} = -\frac{\partial}{\partial Y}(\frac{P}{\rho}) + \frac{\partial}{\partial Y}(\frac{\tau_{yy}}{\rho}) + \frac{\partial}{\partial Z}(\frac{\tau_{zy}}{\rho}) + F_y \tag{3.1.3}$$

Z direction or the transverse direction

$$V\frac{\partial W}{\partial Y} + W\frac{\partial W}{\partial Z} = -\frac{\partial}{\partial Z}(\frac{P}{\rho}) + \frac{\partial}{\partial Y}(\frac{\tau_{yz}}{\rho}) + \frac{\partial}{\partial Z}(\frac{\tau_{zz}}{\rho}) + F_z \tag{3.1.4}$$

where U,V,W are the time average mean velocities in the X,Y,Z directions, respectively, (see Figure 2.1), P is the time average mean pressure, τ_{ij} are turbulent (Reynolds) stress components, and F_i are the components of the body force.

To close the above system of equations, where the turbulent stresses are unknown, algebraic stress models are utilized that express the turbulent stresses in terms of mean velocity gradients and turbulent viscosity. Two different sets of algebraic stress models are used, one for closed channels and the other for open channels. For closed channels the non-linear algebraic stress relations of Speziale (1987) are used and are expressed as

$$\frac{\tau_{yy}}{\rho} = -\frac{2}{3}K + l^2 \left[\left(\frac{C_E}{3}+\frac{C_D}{12}\right)\left(\frac{\partial U}{\partial Y}\right)^2 + \left(\frac{C_E}{3}-\frac{C_D}{6}\right)\left(\frac{\partial U}{\partial Z}\right)^2\right] + 2\,\nu_T \frac{\partial V}{\partial Y} \tag{3.1.5}$$

$$\frac{\tau_{zz}}{\rho} = -\frac{2}{3}K + l^2 \left[\left(\frac{C_E}{3}+\frac{C_D}{12}\right)\left(\frac{\partial U}{\partial Z}\right)^2 + \left(\frac{C_E}{3}-\frac{C_D}{6}\right)\left(\frac{\partial U}{\partial Y}\right)^2\right] + 2\,\nu_T \frac{\partial W}{\partial Z} \tag{3.1.6}$$

$$\frac{\tau_{zx}}{\rho} = \frac{1}{2} K^{\frac{1}{2}}\, l\, \frac{\partial U}{\partial Z} \tag{3.1.7}$$

$$\frac{\tau_{yx}}{\rho} = \frac{1}{2} K^{\frac{1}{2}}\, l\, \frac{\partial U}{\partial Y} \tag{3.1.8}$$

$$\frac{\tau_{yz}}{\rho} = \frac{1}{4} C_D\, l^2 \left(\frac{\partial U}{\partial Z}\right)\left(\frac{\partial U}{\partial Y}\right) \tag{3.1.9}$$

where the form used for the length scale is given as

$$l = 2\, C_\mu \frac{K^{3/2}}{\epsilon}\ . \tag{3.1.10}$$

The constants C_E and C_D are dimensionless and are specified by Speziale as 1.68 based upon turbulent channel data.

In open channels, the non-linear algebraic stress relations of Naot and Rodi (1982) are used with some modifications. These relations take into account the free surface effects which significantly reduce the length scale and turbulent viscosity at the free surface. Consequently, the dissipation rate ϵ increases at the free surface which requires using a different free surface boundary condition for ϵ. The free surface effects are induced in the turbulent stress expressions using turbulent viscosity for the vertical momentum transfer which is different than that for the lateral momentum transfer (i.e., using non-isotropic turbulent viscosity). In addition, the turbulent stress expressions contain coefficients that reflect free surface effects. The modified turbulent stresses are expressed as

$$\frac{\tau_{yx}}{\rho} = \nu_{TY} \frac{\partial U}{\partial Y} \tag{3.1.11}$$

$$\nu_{TY} = \frac{C_1^{\,2}}{(C_1 + \frac{3}{2} C_3)(C_1 + 2C_3)} \nu_T \tag{3.1.12}$$

$$\nu_T = C_\mu \frac{K^2}{\epsilon} \tag{3.1.13}$$

$$\frac{\tau_{zx}}{\rho} = \nu_{TZ} \frac{\partial U}{\partial Z} \tag{3.1.14}$$

$$\nu_{TZ} = \frac{(c_1 + \frac{5}{2} C_3)}{(C_1 + 2 C_3)} \nu_T \tag{3.1.15}$$

$$\begin{aligned} \frac{\tau_{yy}}{\rho} = & -\frac{K}{(C_1 + 2 C_3)}[\frac{2}{3}(\alpha - \frac{1}{2}\beta + C_1 - 1) \\ & + \frac{\beta}{\epsilon}(-\frac{\tau_{yx}}{\rho} \frac{\partial U}{\partial Y} + \frac{\tau_{zx}}{\rho} \frac{\partial U}{\partial Z})] \\ & + 2 \nu_{TY} \frac{\partial V}{\partial Y} \end{aligned} \tag{3.1.16}$$

$$\frac{\tau_{zz}}{\rho} = -\frac{K}{C_1}[\frac{2}{3}(\alpha-\frac{1}{2}\beta+C_1-1)$$

$$+\frac{\beta}{\epsilon}(-\frac{\tau_{zx}}{\rho}\frac{\partial U}{\partial Z}+\frac{\tau_{yx}}{\rho}\frac{\partial U}{\partial Y})-C_3\frac{\tau_{yy}}{\rho K}] \tag{3.1.17}$$

$$+2\,\nu_{TZ}\frac{\partial W}{\partial Z}$$

$$\frac{\tau_{yz}}{\rho} = -\frac{\beta}{(C_1+\frac{3}{2}C_3)}\frac{K}{\epsilon}(-\frac{\tau_{zx}}{\rho}\frac{\partial U}{\partial Y}-\frac{\tau_{yx}}{\rho}\frac{\partial U}{\partial Z}) \tag{3.1.18}$$

$$+\nu_{TY}\frac{\partial W}{\partial Y}+\nu_{TZ}\frac{\partial V}{\partial Z}$$

where the non-isotropic turbulent viscosities ν_{TZ} and ν_{TY} are used in expressions for turbulent stresses τ_{zz}, τ_{yy}, and τ_{yz} in contrast to Naot and Rodi (1982) who used an isotropic viscosity ν_T.

The model coefficients are given in terms of two functions that account for the distance from a solid wall (f_1) and the distance from an open surface (f_2) given by

$$\alpha = 0.7636 - 0.06\,f_1 \tag{3.1.19}$$

$$\beta = 0.1091 + 0.06\,f_1 \tag{3.1.20}$$

$$C_1 = 1.5 - 0.5\,f_1 \quad , \quad C_3 = 0.1\,f_2 \,. \tag{3.1.21}$$

Instead of using the functions f_1 and f_2 as given by Naot and Rodi in Equation (2.7.16) in which the mixing length is generally unknown, different algebraic functions are developed in this model. These functions are expressed as

$$f_1 = (1-Y/H)^2 \tag{3.1.22}$$

and

$$f_2 = (Y/H)^2 \tag{3.1.23}$$

where Y is the normal distance to the wall and H is the channel depth. The functions f_1 and f_2 satisfy the same conditions as those of Naot and Rodi (1982). They are equal to 1.0 at the surface they represent and to zero at all other surfaces. They have the advantage of being algebraic and do not depend upon the mixing length which is usually not known.

For both closed and open channels, the algebraic stress model contains the turbulent viscosity which is expressed in terms of the turbulent kinetic energy K, and the rate of dissipation of the turbulent kinetic energy ϵ, as

$$\nu_t = C_\mu \frac{K^2}{\epsilon} \tag{3.1.24}$$

where C_μ is a dimensionless constant of value 0.09.

The two quantities K and ϵ are evaluated from differential transport equations. The transport equations for steady, fully developed, and high Reynolds number flow are the turbulent kinetic energy transport equation (K):

$$\begin{aligned} V \frac{\partial K}{\partial Y} + W \frac{\partial K}{\partial Z} = \frac{\partial}{\partial Y}\left(\frac{\nu_T}{\sigma_K} \frac{\partial K}{\partial Y}\right) + \frac{\partial}{\partial Z}\left(\frac{\nu_T}{\sigma_K}\frac{\partial K}{\partial Z}\right) \\ + \nu_T \left[\left(\frac{\partial U}{\partial Y}\right)^2 + \left(\frac{\partial U}{\partial Z}\right)^2\right] - \epsilon \end{aligned} \tag{3.1.25}$$

and the dissipation rate of the turbulent kinetic energy transport equation (ϵ):

$$\begin{aligned} V \frac{\partial \epsilon}{\partial Y} + W \frac{\partial \epsilon}{\partial Z} = \frac{\partial}{\partial Y}\left(\frac{\nu_T}{\sigma_\epsilon} \frac{\partial \epsilon}{\partial Y}\right) + \frac{\partial}{\partial Z}\left(\frac{\nu_T}{\sigma_\epsilon}\frac{\partial \epsilon}{\partial Z}\right) \\ + C_{\epsilon 1} C_\mu K\left[\left(\frac{\partial U}{\partial Y}\right)^2 + \left(\frac{\partial U}{\partial Z}\right)^2\right] - C_{\epsilon 2} \frac{\epsilon}{K}\epsilon \end{aligned} \tag{3.1.26}$$

where σ_K, σ_ϵ, $C_{\epsilon 1}$, and $C_{\epsilon 2}$ are dimensionless constants that must be determined experimentally. Rodi (1984) reports standard values as 1.0, 1.3, 1.44, and 1.92, respectively.

For the boundary conditions, the wall function approach of Launder and Spalding (1974) is adopted. In this approach the boundary conditions are specified at a virtual boundary located a distance from the wall outside the viscous sublayer in which the K-ϵ model is not applicable.

The longitudinal (primary) shear stress on virtual wall boundaries is expressed as by Schamber and Larock (1981) as

$$\frac{\tau}{\rho} = -u_*|u_*| = \frac{-\kappa^2}{[\ln E\frac{yu_*}{\nu}]^2}|U|U \tag{3.1.27}$$

where E is taken by Yalin for the entire turbulent regime from:

$$E = \frac{e^{\kappa B_s}}{(\frac{u_* K_s}{\nu})} \tag{3.1.28}$$

in which

$$B_s = [5.5+2.5 \ln R] \, exp\{-0.217 \, (\ln R)^2\} \\ +8.5 \, (1-exp\{-0.217 \, (\ln R)^2\} \tag{3.1.29}$$

$$and \quad R = (\frac{u_* K_s}{\nu}) \tag{3.1.30}$$

The transverse (secondary) shear on virtual wall boundaries is expressed as

$$\tau_t = -\rho \, (\frac{u_*}{U})^2 \, U_t|U_t| \tag{3.1.31}$$

where τ_t is the transverse shear and U_t is the transverse (secondary) velocity.

The boundary conditions for K and ϵ at virtual wall boundaries are:

$$K = \frac{u_*^2}{\sqrt{C_\mu}} \tag{3.1.32}$$

and

$$\epsilon = \frac{u_*^3}{\kappa\, y} \ . \tag{3.1.33}$$

The normal velocity at the virtual walls, planes of symmetry, and free surfaces is zero. Gradients of the variables at planes of symmetry are also zero. The free surface modeled as a frictionless lid is treated as a plane of symmetry for all variables except ϵ. These same conditions were used by Naot and Rodi (1982), Naot (1984), and Naot et al. (1993).

The free surface boundary condition for ϵ developed by Yacoub (1992) is used herein and is expressed as

$$\frac{d\epsilon}{dX_n} = C_{\epsilon F}\, \frac{\epsilon^2}{K^{3/2}} \tag{3.1.34}$$

where $C_{\epsilon F} = 3.5$.

3.2 The Finite Element Formulation of the Governing Equations:

In order to implement the finite element method, the domain of interest is divided into small elements to form a computational mesh or grid. The finite element approximation of a variable is accomplished with known shape functions determined by the element type and its nodal values. For example, a variable ϕ is expressed within an element as

$$\phi(Z,Y) = \sum_{i=1}^{n} N_i \ \Phi_i \tag{3.2.1}$$

where N_i are the element shape functions, Φ_i are the nodal values of the variable, and n is the number of nodes for the element. In using Equation (3.2.1) as the finite element approximation for a variable from herein, the summation symbol will be deleted and summation will be over repeated indices as in Einstein's summation rules.

Care must be taken to assure that these piece-wise approximations are continuous between elements. The exception to this requirement is the pressure which is not integrated by parts to obtain the weak form of the governing equations.

In this study, where the domain of interest is two dimensional, the 4-node element is used to approximate U, V, W, K, and ϵ variables. The pressure, which is not required to be continuous over the domain, is assumed constant within each element.

The governing equations for the problem are written in their weak form. That is, the weighted average of the governing differential equation over the domain of the analysis is required to be zero for arbitrary weighting functions. Following the Galerkin method, the weighting functions are interpreted as variations in the dependent variable. For example,

$$\int_A \delta\phi \ (E_\phi) \ dA = 0 \tag{3.2.2}$$

where

A = the domain for the differential equation, and

E_ϕ = the partial differential equation for the variable ϕ.

Integration by parts is used to reduce the highest order derivatives to one order less (hence the name weak form of the equations) and results in (for two dimensional analysis) line integrals along the exterior boundaries. These line integrals place boundary conditions on the gradients of ϕ on these boundaries where ϕ is not explicitly specified. The equations are cast in the basic Newton form suitable for solving non-linear equations as

$$\int_A \delta\phi \, \left(\frac{\partial E_\phi}{\partial \phi} \, d\phi\right) \, dA \; = \; -\int_A \delta\phi \; E_\phi dA \tag{3.2.3}$$

Substitution of the finite element approximating functions results in a set of integral equations. These equations are integrated over each element using Gaussian quadrature. The contribution of all element integrations are added together to obtain a global matrix the solution of which represents the finite element approximation of the boundary value problem. Because the governing equations are non-linear in this study, the global matrix representing them is also non-linear. The final set of the equations is written in a matrix form as

$$[\; A(X^n) \;] \; \{\delta X^n\} \; = \; \{-f(X^n)\} \tag{3.2.4}$$

in which

n = iteration counter,

A = non-linear Jacobian matrix reflecting the nature of the governing equations,

X^n = set of unknown nodal values of the variables of the problem,

δX^n = set of incremental corrections to be made to the vector X^n, and

f = vector of forcing functions which represent source and sink type terms.

After solving Equation (3.2.4), the solution vector is updated at each iteration via

$$X^{n+1} = X^n + \alpha\ \delta X^n \tag{3.2.5}$$

in which α is the relaxation factor.

The non-dimensional form of the governing equations is used in the mathematical model. Selected variables representing density, length, and velocity are used as the independent normalizing variables. Secondary velocities are normalized differently than the main velocity because the secondary velocities are smaller compared with the main velocity. Therefore, the main velocity U is normalized by the measured cross sectional average main velocity (U_o), while the secondary velocities are normalized using the measured average shear velocity (u_*) which has the same order of magnitude as the secondary velocities. All length coordinates (X,Y and Z) are normalized by using H which is equal to half the duct height in closed channels and equal to the flow depth in open channels. The pressure and turbulent stresses are normalized by $\rho\ U_o^2$ in the X-equation and normalized by $\rho\ u_*^2$ in the Y and Z equations. The body force term, F, is normalized using U_o^2/H in the X equation and u_*^2/H in the Y and Z equations. The turbulent kinetic energy K is normalized by U_o^2 and the rate of dissipation ϵ is normalized by U_o^3/H .

The form of the normalized governing equations used in the mathematical model is the same as the original equations except for replacing the variables by their non-dimensional counterparts. From herein, all governing equations are understood to be in a non-dimensional form.

Following are details for applying the finite element method to the Reynolds equations of motion and the continuity equation, together with the K and ϵ equations.

The form of the Jacobian matrix for these equations is presented in Figures 3.1a, and 3.1b.

3.3 The Continuity Equation:

The iterative penalty approach is used to enforce the constraint of incompressibility. In this approach the pressure is considered as an implicit variable adjusting itself to enforce the incompressibility constraint as stated by Gresho et al. (1980). The pressure is given by

$$P^{n+1} = P^{n} - \lambda \left(\frac{\partial V}{\partial Y} + \frac{\partial W}{\partial Z}\right) \tag{3.3.1}$$

where λ is the penalty parameter.

Equation (3.3.1) is used to replace the continuity equation. The new system of governing equations in matrix form becomes

$$\begin{bmatrix} A & C \\ C^{T} & -\dfrac{I}{\lambda} \end{bmatrix}^{n} \begin{bmatrix} u \\ P \end{bmatrix}^{n+1} = \begin{bmatrix} f_1 \\ -\dfrac{P}{\lambda} \end{bmatrix}^{n} \tag{3.3.2}$$

where A is the stiffness sub-matrix resulting from the convective and diffusive terms in the momentum equations, C is the submatrix resulting from the derivatives in the continuity equation, C^{T} is the transpose of C, I is the identity matrix, n is the iteration number, u is the vector containing the velocities, P is the vector containing pressure, and f_1 is the vector containing the source terms in the equations of motion.

Equation (3.3.2) is written in the form

$$[A]^{n} \, [u]^{n+1} + [C] \, [P]^{n+1} = [f_1]^{n} \tag{3.3.3a}$$

and

$$\left[C^{T}\right][u]^{n+1}+\left[-\frac{I}{\lambda}\right][P]^{n+1}=\left[-\frac{P}{\lambda}\right]^{n} \tag{3.3.3b}$$

The pressure is found from Equation (3.3.3b) to be equal to

$$[P]^{n+1}=[P]^{n}-\lambda\left[C^{T}\right][u]^{n} \tag{3.3.4}$$

Substitution of Equation (3.3.4) into Equation (3.3.3a) yields

$$[A]^{n}[u]^{n+1}+[C][-\lambda]\left[C^{T}\right][u]^{n+1}=\left[f_{1}\right]^{n}-[C][P]^{n} \tag{3.3.5}$$

The pressure in the first iteration of Equation (3.3.5) is set to zero. After solving the system of equations and obtaining secondary velocities V and W, the pressure is updated via Equation (3.3.1) and the process of substituting and updating continues until convergence is obtained.

The Form of equation (3.3.1) allows the penalty parameter to take small values as well as large ones. The penalty parameter has the dimensions of viscosity and is normalized in equation (3.3.1) using (ρ u_* H) where ρ is the fluid density, u_* is the shear velocity, and H is the channel depth. A value of the dimensionless penalty parameter equal to 100 in both closed and open channels is chosen. With an average turbulent viscosity of about 0.07 u_* H, the ratio of λ to the average turbulent viscosity becomes about 1400. This ratio is considerably smaller than that in classical penalty methods. A high ratio can cause severe round off error problems in the computer model.

3.4 The X-direction Momentum Equation:

The momentum Equation (3.1.2) in the X-direction determines the distribution of the longitudinal velocity U. The weak form of Equation (3.1.2) is obtained by multiplying the equation by the variational δU and integrating over the domain to yield

$$f_U = \int_A \delta U \{V\frac{\partial U}{\partial Y} + W\frac{\partial U}{\partial Z} + \frac{dP}{dX} - F_X - \frac{\partial \tau_{yx}}{\partial Y} - \frac{\partial \tau_{zx}}{\partial Z}\} dA = 0 \tag{3.4.3}$$

where A is the area of the flow cross section.

The last two terms in Equation (3.4.3) are integrated by parts to obtain

$$\begin{aligned} f_U = & \int_A \delta U \{V\frac{\partial U}{\partial Y} + W\frac{\partial U}{\partial Z} + \frac{dP}{dX} - F_X\} dA \\ & - \int_A \{\frac{\partial(\delta U \tau_{yx})}{\partial Y} + \frac{\partial(\delta U \tau_{zx})}{\partial Z}\} dA \\ & + \int_A \{\frac{\partial \delta U}{\partial Y}\tau_{yx} + \frac{\partial \delta U}{\partial Z}\tau_{zx}\} dA \\ & = 0 \end{aligned} \tag{3.4.4}$$

The application of the divergence theorem to the second integral in Equation (3.4.4) yields

$$\begin{aligned} f_U = & \int_A \delta U \{V\frac{\partial U}{\partial Y} + W\frac{\partial U}{\partial Z} + \frac{dP}{dX} - F_X\} dA - \int_S \delta U \{\tau_{yx} l_y + \tau_{zx} l_z\} dS \\ & + \int_A \{\frac{\partial \delta U}{\partial Y}\tau_{yx} + \frac{\partial \delta U}{\partial Z}\tau_{zx}\} dA = 0 \end{aligned} \tag{3.4.5}$$

where

l_y and l_z = the direction cosines of the j and k unit vectors, respectively, and

S = is the coordinate along the perimeter of the cross section.

The wall function approach of Launder and Spalding (1974) is adopted in which the boundary conditions are expressed at a distance from the walls. Thus, the boundary shear stresses in the line integral of Equation (3.4.5) along planes 1 and 4 in Figure 3.2 are expressed in terms of longitudinal velocity U at a distance Y from the wall via the logarithmic law of the wall which is rewritten here as

$$\frac{\tau}{\rho} = -u_*|u_*| = -c_f|U|U . \tag{3.4.6}$$

where

$$c_f = \frac{\kappa^2}{[\ln(E\frac{u_* Y}{\nu})]^2} \tag{3.4.7}$$

The minus sign in (3.4.6) indicates that boundary shear is in the opposite direction to velocity. The shear stress τ_{zx} along plane 3 (in Figure 3.2) is zero, because plane 3 is a plane of symmetry in both closed and open channels. Plane 2 (Figure 3.2) is a plane of symmetry in the closed channel case and a free surface in the open channel case. Therefore, τ_{yx} is zero along this plane in both cases. Accordingly, the line integral in Equation (3.4.5) is identically zero along planes 2 and 3 in both cases of closed and open channels.

The primary shear stresses in the area integral of Equation (3.4.5) are expressed by their linear expressions as in Equations (2.5.6) and (2.5.7). For closed channels, the isotropic turbulent viscosity ν_T is used in the expressions for the shear stresses. For open channels, ν_{TY} is used in the expression for τ_{yx}, and ν_{TZ} is used in the expression for τ_{zx}.

Substitution of Equations (2.5.6) and (2.5.7) for the shear stresses into the area integrals of Equation (3.4.5) and Equation (3.4.6) for the boundary shear into the line integrals of Equation (3.4.5) yields

$$
\begin{aligned}
f_U = &\int_A \delta U\{V\frac{\partial U}{\partial Y}+W\frac{\partial U}{\partial Z}+\frac{dP}{dX}-F_X\}dA \\
&-\int_S \{\delta U(-c_f|U|U)(l_Y+l_Z)\}dS \\
&+\int_A \{\frac{\partial \delta U}{\partial Y}\nu_T\frac{\partial \delta U}{\partial Y}+\frac{\partial \delta U}{\partial Z}\nu_T\frac{\partial \delta U}{\partial Z}\}dA = 0
\end{aligned} \tag{3.4.8}
$$

Substitution of the finite element approximations for U and δU into Equation (3.4.8) written for a general element yields

$$
\begin{aligned}
f_U = &\int_{A_e} N_i\{V\frac{\partial N_J}{\partial Y}U_J+W\frac{\partial N_J}{\partial Z}U_J+\frac{dP}{dX}-F_X\}dA_e \\
&+\int_S \{N_i(c_f|U|N_JU_J)(l_Y+l_Z)\}dS \\
&+\int_{A_e} \{\frac{\partial N_i}{\partial Y}\nu_T\frac{\partial N_J}{\partial Y}U_J+\frac{\partial N_i}{\partial Z}\nu_T\frac{\partial N_J}{\partial Z}U_J\}dA_e=0.0
\end{aligned} \tag{3.4.9}
$$

where A_e is the element area.

The entries for the Jacobian matrix from the X-equation are

$$
\begin{aligned}
\frac{\partial f_U}{\partial U_J} = &\int_{A_e} N_i\{V\frac{\partial N_J}{\partial Y}+W\frac{\partial N_J}{\partial Z}\}dA_e+\int_S \{N_i(2c_f|U|N_J)(l_Y+l_Z)\}dS \\
&+\int_{A_e} \{\frac{\partial N_i}{\partial Y}\nu_T\frac{\partial N_J}{\partial Y}+\frac{\partial N_i}{\partial Z}\nu_T\frac{\partial N_J}{\partial Z}\}dA_e
\end{aligned} \tag{3.4.10}
$$

$$
\frac{\partial f_U}{\partial V_J} = \int_{A_e}(N_iN_J\frac{\partial U}{\partial Y})dA_e \tag{3.4.11}
$$

and

$$
\frac{\partial f_U}{\partial W_J} = \int_{A_e}(N_iN_J\frac{\partial U}{\partial Z})dA_e \tag{3.4.12}
$$

The non-linearity of the X-equation appears in the Jacobian matrix entries given by Equations (3.4.10) to (3.4.12). The three velocities U, V, W, and the turbulent viscosity ν_T appear in these Jacobian matrix entries. The turbulent viscosity contains K and ϵ as in equation (3.1.13). Therefore, initial starting values for U, V, W , K, and ϵ are required for the linearized Jacobian matrix.

In the present formulation, the two entries of the Jacobian matrix given by Equations (3.4.11) and (3.4.12) are neglected. This is justified by the assumption that in the X-momentum equation, secondary velocities V and W are constant within each element. However, the effect of the secondary velocities V and W on the longitudinal velocity U is still included through the first integral term in Equation (3.4.10).

It should be noted that in closed channels, the forcing function in the X-equation is the longitudinal pressure gradient dp/dx which is known from measurements, and that the body force term F_X is zero because all closed channel cases studied herein are horizontal. In open channels, dp/dx is zero because the flow is assumed fully developed and the forcing function is equal to the body force term F_X. The body force term F_X in open channels is equal to the X-component of the unit weight of the fluid. The X-component of the unit weight of the fluid in open channels is given by

$$F_X = \gamma \sin \theta \tag{3.4.13}$$

where γ is the unit weight of the fluid and θ is the slope of the channel with the horizontal.

3.5 The Y-direction Momentum Equation:

The procedure used for the X-momentum equation in Section 3.4 is applied for the Y-equation. The weak form of the Y-equation (3.1.3) is written as

$$f_V = \int_A \delta V\{V\frac{\partial V}{\partial Y}+W\frac{\partial V}{\partial Z}-F_Y\}dA+\int_A \delta V\frac{\partial P}{\partial Y}dA$$
$$-\int_A \delta V\{\frac{\partial \tau_{yy}}{\partial Y}+\frac{\partial \tau_{zy}}{\partial Z}\}dA = 0 \ . \qquad (3.5.1)$$

Integration of the second and the third integral terms by parts yields

$$f_V = \int_A \delta V\{V\frac{\partial V}{\partial Y}+W\frac{\partial V}{\partial Z}-F_Y\}dA+\int_A \frac{\partial(\delta V\ P)}{\partial Y}dA-\int_{A_e} \frac{\partial \delta V}{\partial Y}\ P\ dA$$
$$-\int_A\{\frac{\partial(\delta V\ \tau_{yy})}{\partial Y}+\frac{\partial(\delta V\ \tau_{zy})}{\partial Z}\}dA+\int_A\{\frac{\partial \delta V}{\partial Y}\tau_{yy}+\frac{\partial \delta V}{\partial Z}\tau_{zy}\}dA \qquad (3.5.2)$$
$$= 0 \ .$$

Application of the divergence theorem to the second and the forth integral terms yields

$$f_V = \int_A \delta V\{V\frac{\partial V}{\partial Y}+W\frac{\partial V}{\partial Z}-F_Y\}dA+\int_S \delta V\ P\ l_Y\ dS-\int_A \frac{\partial \delta V}{\partial Y}\ P\ dA$$
$$-\int_S \delta V\{\tau_{yy}l_y+\tau_{zy}l_Z\}dS+\int_A\{\frac{\partial \delta V}{\partial Y}\tau_{yy}+\frac{\partial \delta V}{\partial Z}\tau_{zy}\}dA = 0 \ . \qquad (3.5.3)$$

For rectangular channels V=0 on planes 2 and 4 in Figure 3.2 because there is no flow normal to these planes. Each plane can be a free surface, a symmetry plane, or a bottom wall boundary. Because V is known (zero) on these planes, δV = 0.0 and the following two terms in Equation (3.5.3) are identically zero, i.e.

$$\int_S \delta V\ P\ l_y\ dS = 0 \qquad (3.5.4)$$

and

$$\int_S \delta V \, \tau_{yy} \, l_y \, dS = 0 \ . \tag{3.5.5}$$

Substitution of Equation (3.3.1) for the pressure into Equation (3.5.3) yields

$$f_V = \int_A \delta V \{ V\frac{\partial V}{\partial Y} + W\frac{\partial V}{\partial Z} - F_Y \} dA - \int_A \frac{\partial \delta V}{\partial Y} [P - \lambda(\frac{\partial V}{\partial Y} + \frac{\partial W}{\partial Z})] dA$$
$$- \int_S \delta V \{ \tau_{zy} l_Z \} dS + \int_A \{ \frac{\partial \delta V}{\partial Y} \tau_{yy} + \frac{\partial \delta V}{\partial Z} \tau_{zy} \} dA = 0 \ . \tag{3.5.6}$$

The cases of closed and open channels are discussed separately because different expressions for the turbulent stresses are used in each.

3.5.1 Closed Channels:

The turbulent stresses suggested by Speziale (1987) in Equations (3.1.5) to (3.1.9) are used in this case. The expressions for τ_{yy} and τ_{yz}, needed in the area integrals of Equation (3.5.6), are rewritten as

$$\tau_{yy} = -\frac{2}{3}K + 2\nu_T \frac{\partial V}{\partial Y} + \sigma_{yy} \tag{3.5.1.1}$$

$$\sigma_{yy} = (\frac{C_E}{3} + \frac{C_D}{12}) l^2 (\frac{\partial U}{\partial Y})^2 + (\frac{C_E}{3} - \frac{C_D}{6}) l^2 (\frac{\partial U}{\partial Z})^2 \ . \tag{3.5.1.2}$$

$$\tau_{zy} = \nu_T (\frac{\partial V}{\partial y} + \frac{\partial W}{\partial Z}) + \sigma_{zy} \tag{3.5.1.3}$$

$$\sigma_{zy} = \frac{C_D}{4} l^2 \frac{\partial U}{\partial Y} \frac{\partial U}{\partial Z} \tag{3.5.1.4}$$

Here σ_{yy} and σ_{zy} represent the non-linear part of the turbulent stress that influences secondary motions. Therefore, they are considered as the forcing function for the secondary motion in the Y-equation and consequently placed in the forcing function vector.

An expression is required to evaluate the line integrals in Equation (3.5.6) for the shear stress τ_{zy} over planes 1 and 3 in Figure 3.2. Plane 3 is a plane of symmetry in which τ_{zy} is zero, and the corresponding line integral becomes zero. For plane 1, which is a wall boundary, τ_{zy} is expressed as

$$\frac{\tau_{zy}}{\rho} = -\frac{u_*^2}{U^2}\ |V|V\ . \tag{3.5.1.5}$$

Equation (3.5.1.5) is based upon the assumption that the ratio of the secondary shear stress to the primary shear stress is equal to the square of ratio of the secondary velocity to the primary velocity.

Substitution for the turbulent stresses in Equations (3.5.1.1) to (3.5.1.4), and Equation (3.5.1.5) into Equation (3.5.6) yields

$$\begin{aligned} f_V = {} & \int_A \delta V\{V\frac{\partial V}{\partial Y} + W\frac{\partial V}{\partial Z} - F_Y + \sigma_{YY} + \sigma_{zy}\}dA - \int_A \frac{\partial \delta V}{\partial Y}[P - \lambda(\frac{\partial V}{\partial Y} + \frac{\partial W}{\partial Z})]dA \\ & + \int_{side1} \delta V\frac{u_*^2|V|}{U^2}Vl_z dS + \int_A\{\frac{\partial \delta V}{\partial Y}2\nu_T\frac{\partial V}{\partial Y} + \frac{\partial \delta V}{\partial Z}\nu_T\frac{\partial V}{\partial Z} + \frac{\partial \delta V}{\partial Z}\nu_T\frac{\partial W}{\partial Y}\}dA\ . \end{aligned}$$

$$(3.5.1.6)$$

Substitution of the finite element approximations into Equation (3.5.1.6) written for a general element gives

$$\begin{aligned} f_V = {} & \int_{A_e} N_i\{V\frac{\partial N_J}{\partial Y}V_J + W\frac{\partial N_J}{\partial Z}V_J - F_Y + \sigma_{yy} + \sigma_{zy}\}dA_e + \int_{A_e}\frac{\partial N_i}{\partial Y}[P - \lambda(\frac{\partial N_J}{\partial Y}V_J + \frac{\partial N_J}{\partial Z}W_J)]dA_e \\ & + \int_{side1} N_i\frac{u_*^2|V|}{U^2}N_J V_J l_z dS + \int_{A_e}\{\frac{\partial N_i}{\partial Y}2\nu_T\frac{\partial N_J}{\partial Y}V_J + \frac{\partial N_i}{\partial Z}\nu_T\frac{\partial N_J}{\partial Z}V_J + \frac{\partial N_i}{\partial Z}\nu_T\frac{\partial N_J}{\partial Y}W_J\}dA_e\ . \end{aligned}$$

$$(3.1.5.7)$$

The entries in the Jacobian matrix are

$$\frac{\partial f_V}{\partial U_J} = 0 \tag{3.5.1.8}$$

$$\frac{\partial f_V}{\partial V_J} = \int_{A_e} N_i\{N_J\frac{\partial V}{\partial Y}+V\frac{\partial N_J}{\partial Y}+W\frac{\partial N_J}{\partial Z}\}dA_e+\int_{A_e}\frac{\partial N_i}{\partial Y}\lambda\frac{\partial N_J}{\partial Y}dA_e$$
$$+\int_{side1} 2N_i\frac{u_*^2|V|}{U^2}N_J l_z dS+\int_{A_e}\{\frac{\partial N_i}{\partial Y}2\nu_T\frac{\partial N_J}{\partial Y}+\frac{\partial N_i}{\partial Z}\nu_T\frac{\partial N_J}{\partial Z}\}dA_e$$

(3.5.1.9)

$$\frac{\partial f_V}{\partial W_J} = \int_{A_e} N_i\{N_J\frac{\partial V}{\partial Z}\}dA_e+\int_{A_e}\frac{\partial N_i}{\partial Y}\lambda\frac{\partial N_J}{\partial Z}dA_e$$
$$+\int_{A_e}\{\frac{\partial N_i}{\partial Z}\nu_T\frac{\partial N_J}{\partial Y}\}dA_e\ . \tag{3.5.1.10}$$

<u>3.5.2 Open Channels:</u>

In open channels, the modified expressions for τ_{yy} and τ_{zy} in Naot and Rodi (1982) are rewritten as

$$\frac{\tau_{yy}}{\rho} = -\frac{K}{(C_1+2\ C_3)}[\frac{2}{3}(\alpha-\frac{1}{2}\beta+C_1-1)]$$
$$+2\ \nu_{Ty}\ \frac{\partial V}{\partial Y}-\sigma_{yy} \tag{3.5.2.1}$$

$$\sigma_{yy}=\frac{K}{(C_1+2\ C_3)}\frac{\beta}{\epsilon}(-\frac{\tau_{yx}}{\rho}\ \frac{\partial U}{\partial Y}+\frac{\tau_{zx}}{\rho}\ \frac{\partial U}{\partial Z})]\ . \tag{3.5.2.2}$$

$$\frac{\tau_{yz}}{\rho} = \nu_{TY}\frac{\partial W}{\partial Y}+\nu_{Tz}\frac{\partial V}{\partial Z}-\sigma_{yz} \tag{3.5.2.3}$$

$$\sigma_{yz} = -\frac{K}{(C_1+\frac{3}{2}\ C_3)}\frac{\beta}{\epsilon}(-\frac{\tau_{zx}}{\rho}\ \frac{\partial U}{\partial Y}-\frac{\tau_{yx}}{\rho}\ \frac{\partial U}{\partial Z})]\ . \qquad (3.5.2.4)$$

The form of the open channel equations is the same as that of the closed channel case except that σ_{yy} and σ_{yz} in Equations (3.5.1.2) and (3.5.1.4) are replaced by σ_{yy} and σ_{yz} in Equations (3.5.2.2) and (3.5.2.4), respectively.

3.6 The Z-direction Momentum Equation:

The procedure used for the X-equation and Y-equation is used here for the Z-equation. The weak form after integration by parts and application of the divergence theorem becomes

$$\begin{aligned} f_W = & \int_A \delta W\{V\frac{\partial W}{\partial Y}+W\frac{\partial W}{\partial Z}-F_Z\}dA+\int_S \delta W\ Pl_z dS-\int_A \frac{\partial \delta\, W}{\partial Z}PdA \\ & -\int_S \delta\, W\{\tau_{yz}l_y+\tau_{zz}l_Z\}dS+\int_A \{\frac{\partial \delta\, W}{\partial Y}\tau_{yz}+\frac{\partial \delta\, W}{\partial Z}\tau_{zz}\}dA = 0\ . \end{aligned} \qquad (3.6.1)$$

For rectangular channels, W is known (zero) on planes 1 and 3 in Figure 3.2. Therefore, $\delta W = 0$ on these two planes and the following two terms in Equation (3.6.1) are identically zero, i.e.

$$\int_S \delta W\ P\ l_z\ dS = 0 \qquad (3.6.2)$$

$$\int_S \delta W\ \tau_{ZZ}\ l_z\ dS = 0\ . \qquad (3.6.3)$$

Substitution of Equation (3.2.1) for the pressure into Equation (3.6.1) yields

$$
\begin{aligned}
f_W = & \int_A \delta W\{V\frac{\partial W}{\partial Y} + W\frac{\partial W}{\partial Z} - F_Z\} dA - \int_A \frac{\partial \delta W}{\partial Z}[P - \lambda(\frac{\partial V}{\partial Y} + \frac{\partial W}{\partial Z})] dA \\
& - \int_S \delta W\{\tau_{yz} l_y\} dS + \int_A \{\frac{\partial \delta W}{\partial Y}\tau_{yz} + \frac{\partial \delta W}{\partial Z}\tau_{zz}\} dA = 0
\end{aligned}
\tag{3.6.4}
$$

The cases for closed and open channels are discussed separately in the following.

3.6.1 Closed Channels:

The turbulent stresses suggested by Speziale (1987) for τ_{zz} and τ_{yz} are used in this case. The expression for τ_{yz} is the same as in Equation (3.5.2.3), while that for τ_{zz} is rewritten as

$$
\tau_{zz} = -\frac{2}{3}K + 2\nu_T\frac{\partial W}{\partial Z} + \sigma_{zz} \tag{3.6.1.1}
$$

where

$$
\sigma_{zz} = (\frac{C_E}{3} + \frac{C_D}{12})l^2(\frac{\partial U}{\partial Z})^2 + (\frac{C_E}{3} - \frac{C_D}{6})l^2(\frac{\partial U}{\partial Z})^2 \ . \tag{3.6.1.2}
$$

The two non-linear parts σ_{zz} in Equation (3.6.1.2), and σ_{yz} in Equation (3.5.2.4) are considered as source terms as is done for the Y-equation. Because plane 2 (in Figure 3.2) is a plane of symmetry along which $\tau_{yz} = 0$, the line integral along this section becomes zero. Along plane 4 (in Figure 3.2) which is a wall boundary, τ_{yz} is expressed as

$$\frac{\tau_{yz}}{\rho} = -\frac{u_*^2}{U^2}|W|W . \tag{3.6.1.3}$$

Substitution from Equations (3.6.1.1) to (3.6.1.3) into equation (3.6.4) yields

$$f_W = \int_A \delta W\{V\frac{\partial W}{\partial Y} + W\frac{\partial W}{\partial Z} - F_Z + \sigma_{zz} + \sigma_{yz}\}dA - \int_A \frac{\partial \delta W}{\partial Z}[P - \lambda(\frac{\partial V}{\partial Y} + \frac{\partial W}{\partial Z})]dA$$
$$+ \int_{side4} \delta W \frac{u_*^2|W|}{U^2} W l_y dS + \int_A \{\frac{\partial \delta W}{\partial Y}\nu_T\frac{\partial V}{\partial Z} + \frac{\partial \delta W}{\partial Y}\nu_T\frac{\partial W}{\partial Y} + \frac{\partial \delta W}{\partial Z}2\nu_T\frac{\partial W}{\partial Z}\}dA$$

(3.6.1.4)

Substitution of the finite element approximations into Equation (3.6.1.4) written for a general element gives

$$f_W = \int_{A_e} N_i\{V\frac{\partial N_J}{\partial Y}W_J + W\frac{\partial N_J}{\partial Z}W_J - F_Z + \sigma_{zz} + \sigma_{yz}\}dA_e$$
$$- \int_{A_e} \frac{\partial N_i}{\partial Z}[P - \lambda(\frac{\partial N_J}{\partial Y}V_J + \frac{\partial N_J}{\partial Z}W_J)]dA_e + \int_{side4} N_i \frac{u_*^2|W|}{U^2} N_J W_J l_y dS$$
$$+ \int_{A_e} \{\frac{\partial N_i}{\partial Y}\nu_T\frac{\partial N_J}{\partial Z}V_J + \frac{\partial N_i}{\partial Y}\nu_T\frac{\partial N_J}{\partial Y}W_J + \frac{\partial N_i}{\partial Z}2\nu_T\frac{\partial N_J}{\partial Z}W_J\}dA_e .$$

(3.6.1.5)

The entries in the Jacobian matrix are

$$\frac{\partial f_W}{\partial U_J} = 0 \tag{3.6.1.6}$$

$$\frac{\partial f_W}{\partial V_J} = \int_{A_e} N_i\{N_J\frac{\partial W}{\partial Y}\}dA_e + \int_{A_e} \frac{\partial N_i}{\partial Y}\nu_T\frac{\partial N_J}{\partial Z}dA_e + \int_{A_e}\{\frac{\partial N_i}{\partial Y}\lambda\frac{\partial N_J}{\partial Y}\}dA_e \tag{3.6.1.7}$$

$$\frac{\partial f_W}{\partial W_J} = \int_{A_e} N_i\{V\frac{\partial N_J}{\partial Y}+N_J\frac{\partial W}{\partial Z}+W\frac{\partial N_J}{\partial Z}\}dA_e+\int_{A_e}\frac{\partial N_i}{\partial Y}\nu_T\frac{\partial N_J}{\partial Y}dA_e$$
$$+\int_{side2} N_i\frac{u_*^2|W|}{U^2}N_J l_y dS+\int_{A_e}\{\frac{\partial N_i}{\partial Z}2\nu_T\frac{\partial N_J}{\partial Z}+\frac{\partial N_i}{\partial Z}\lambda\frac{\partial N_J}{\partial Z}\}dA_e \tag{3.6.1.8}$$

3.6.2 Open Channels:

The expressions of Naot and Rodi (1982) are modified as is done for the Y-equation. The expression for τ_{yz} is given by Equation (3.5.2.1) and τ_{zz}, is rewritten as

$$\frac{\tau_{zz}}{\rho}=\frac{K}{C_1}[\frac{2}{3}(\alpha-\frac{1}{2}\beta+C_1-1)+2\nu_{Tz}\frac{\partial W}{\partial Z}-\sigma_{zz} \tag{3.6.2.1}$$

where

$$\sigma_{zz}=\frac{K}{C_1}[\frac{\beta}{\epsilon}(\frac{\tau_{ZX}}{\rho}\frac{\partial U}{\partial Z}-\frac{\tau_{YX}}{\rho}\frac{\partial U}{\partial Y})+C_3\frac{\tau_{YY}}{\rho k}] \ . \tag{3.6.2.2}$$

The form of the open channel equations is the same as that of the closed channel case except for the use of σ_{zz} from Equation (3.6.1.2) and σ_{yz} from Equation (3.5.2.4) in Equation (3.6.1.4).

3.7 The K-transport Equations:

The weak form for the turbulent kinetic energy Equation (3.1.25) is written as

$$f_K = \int_{A_e}\delta K\{V\frac{\partial K}{\partial Y}+W\frac{\partial K}{\partial Z}\}dA_e-\int_{A_e}\delta K\{\frac{\partial}{\partial Y}(\frac{\nu_T}{\sigma_K}\frac{\partial K}{\partial Y})+\frac{\partial}{\partial Z}(\frac{\nu_T}{\sigma_K}\frac{\partial K}{\partial Z})\}dA_e$$
$$-\int_{A_e}\delta K\{\nu_T(\frac{\partial U}{\partial Y})^2+\nu_T(\frac{\partial U}{\partial Z})^2\}dA_e+\int_{A_e}\delta K\ \epsilon\ dA_e \ . \tag{3.7.1}$$

P_k

Integration of the second integral term by parts and application of the divergence theorem yields

$$f_K = \int_A \delta K\{V\frac{\partial K}{\partial Y}+W\frac{\partial K}{\partial Z}\}dA+\int_A\{\frac{\partial\delta K}{\partial Y}\frac{\nu_T}{\sigma_K}\frac{\partial K}{\partial Y}+\frac{\partial\delta K}{\partial Z}\frac{\nu_T}{\sigma_k}\frac{\partial K}{\partial Z}\}dA$$
$$-\int_S \delta K\{(\frac{\nu_T}{\sigma_K}\frac{\partial K}{\partial Y}l_y)+(\frac{\nu_T}{\sigma_K}\frac{\partial K}{\partial Z}l_z)\}dS$$
$$-\int_A \delta K\ \{\nu_T(\frac{\partial U}{\partial Y})^2+\nu_T(\frac{\partial U}{\partial Z})^2\}dA+\int_A \delta K\ \epsilon dA\ . \tag{3.7.2}$$

Because in both closed and open channels K is specified at the walls by Equation (2.9.1.10) and the symmetry boundary condition is $\partial K/\partial X_n=0$, the line integral terms in Equation (3.7.2) are identically zero. This increases the diagonal dominance of the K equation, which improves the convergence characteristics.

Equation (3.7.2) is written for a general element and the substitution of the finite element approximations gives

$$f_K = \int_A N_i\{V\frac{\partial N_J}{\partial Y}K_J+W\frac{\partial N_J}{\partial Z}K_J\}dA+\int_A\{\frac{\partial N_i}{\partial Y}\frac{\nu_T}{\sigma_K}\frac{\partial N_J}{\partial Y}K_J+\frac{\partial N_i}{\partial Z}\frac{\nu_T}{\sigma_k}\frac{\partial N_J}{\partial Z}K_J\}dA$$
$$-\int_A N_i\{\nu_T(\frac{\partial U}{\partial Y})^2+\nu_T(\frac{\partial U}{\partial Z})^2\}dA+\int_A N_i\ N_J\ \epsilon_J\ dA \tag{3.7.3}$$

The turbulent kinetic energy K appears in the third integral term of Equation (3.7.3) through the turbulent viscosity ν_T. In calculating the Jacobian matrix entry $\partial f_K/\partial K_j$, the turbulent kinetic energy is assumed constant. This assumption is due to the high non-linearity of the third integral term in equation (3.7.3) which has the square of both turbulent kinetic energy and primary velocity gradient. Near the walls both the turbulent kinetic energy and primary velocity gradients are high.

The entries in the Jacobian matrix are

$$\frac{\partial f_K}{\partial K_J} = \int_{A_e} N_i\{V\frac{\partial N_J}{\partial Y}+W\frac{\partial N_J}{\partial Z}\}dA_e+\int_{A_e}\{\frac{\partial N_i}{\partial Y}\frac{\nu_T}{\sigma_K}\frac{\partial N_J}{\partial Y}+\frac{\partial N_i}{\partial Z}\frac{\nu_T}{\sigma_k}\frac{\partial N_J}{\partial Z}\}dA_e$$
$$+\int_{A_e}\{\frac{\partial N_i}{\partial Y}\frac{2c_\mu}{\sigma_K}\frac{K}{\epsilon}\frac{\partial K}{\partial Y}N_J+\frac{\partial N_i}{\partial Z}\frac{2c_\mu}{\sigma_K}\frac{K}{\epsilon}\frac{\partial K}{\partial Z}N_J\}dA_e \tag{3.7.4}$$

and

$$\frac{\partial f_K}{\partial \epsilon_J} = -\int_{A_e}\{\frac{\partial N_i}{\partial Y}\frac{c_\mu}{\sigma_K}\frac{K^2}{\epsilon^2}\frac{\partial K}{\partial Y}N_J+\frac{\partial N_i}{\partial Z}\frac{c_\mu}{\sigma_K}\frac{K^2}{\epsilon^2}\frac{\partial K}{\partial Z}N_J\}dA_e$$
$$+\int_{A_e}N_i c_\mu\frac{K^2}{\epsilon^2}[(\frac{\partial U}{\partial y})^2+\frac{\partial U}{\partial Z})^2]dA_e+\int_{A_e}N_iN_JdA_e\ . \tag{3.7.5}$$

3.8 The ϵ-transport Equation:

The weak form for the ϵ-equation (3.1.26) is written as

$$f_\epsilon = \int_A \delta\epsilon\{V\frac{\partial\epsilon}{\partial Y}+W\frac{\partial\epsilon}{\partial Z}\}dA-\int_A\delta\epsilon\{\frac{\partial}{\partial Y}(\frac{\nu_T}{\sigma_\epsilon}\frac{\partial\epsilon}{\partial Y})+\frac{\partial}{\partial Z}(\frac{\nu_T}{\sigma_\epsilon}\frac{\partial\epsilon}{\partial Z})\}dA$$
$$-\int_A\delta\epsilon c_{\epsilon1}c_\mu K\{(\frac{\partial U}{\partial Y})^2+(\frac{\partial U}{\partial Z})^2\}dA+\int_A\delta\epsilon c_{\epsilon2}\frac{\epsilon}{K}\epsilon dA \tag{3.8.1}$$

Integration by parts of the second integral term and application of the divergence theorem yields

$$f_\epsilon = \int_A \delta\epsilon\{V\frac{\partial\epsilon}{\partial Y}+W\frac{\partial\epsilon}{\partial Z}\}dA+\int_A\{\frac{\partial\delta\epsilon}{\partial Y}\frac{\nu_T}{\sigma_\epsilon}\frac{\partial\epsilon}{\partial Y}+\frac{\partial\delta\epsilon}{\partial Z}\frac{\nu_T}{\sigma_\epsilon}\frac{\partial\epsilon}{\partial Z}\}dA$$
$$-\int_S\delta\epsilon\{(\frac{\nu_T}{\sigma_\epsilon}\frac{\partial\epsilon}{\partial Y}l_y)+(\frac{\nu_T}{\sigma_\epsilon}\frac{\partial\epsilon}{\partial Z}l_z)\}dS$$
$$-\int_A\delta\epsilon c_{\epsilon1}c_\mu K\{(\frac{\partial U}{\partial Y})^2+(\frac{\partial U}{\partial Z})^2\}dA+\int_A\delta\epsilon c_{\epsilon3}\frac{\epsilon}{K}\epsilon dA\ . \tag{3.8.2}$$

For both closed and open channels, ϵ is specified along the wall boundaries (planes 1 and 4 in Figure 3.2) and $\partial\epsilon/\partial Z$ is zero along the plane of symmetry (plane 3 in Figure 3.2), thus the line integrals on these planes are identically zero.

In closed channels, $\partial\epsilon/\partial y=0$ on the symmetry plane 2 (Figure 3.2) and all the line integrals are identically zero. In open channels, the surface boundary condition developed by Yacoub et el. (1992) is used and $\partial\epsilon/\partial y = C_{\epsilon F}\,(\epsilon^2/K^{3/2})$.

Equation (3.8.2), written for a general element in terms of the finite element approximations, is

$$f_\epsilon = \int_{A_e} N_i\{V\frac{\partial N_J}{\partial Y}\epsilon_J + W\frac{\partial N_J}{\partial Z}\epsilon_J\}dA_e + \int_{A_e}\{\frac{\partial N_i}{\partial Y}\frac{\nu_T}{\sigma_\epsilon}\frac{\partial N_J}{\partial Y}\epsilon_J + \frac{\partial N_i}{\partial Z}\frac{\nu_T}{\sigma_\epsilon}\frac{\partial N_J}{\partial Z}\epsilon_J\}dA_e$$
$$-\int_{A_e} N_i c_{\epsilon 1} c_\mu K\{(\frac{\partial U}{\partial Y})^2 + (\frac{\partial U}{\partial Z})^2\}dA_e - \int_S N_i\frac{\nu_T}{\sigma_\epsilon}\frac{\partial N_J}{\partial Y}\epsilon_J l_y ds + \int_{A_e} N_i C_{\epsilon 2}\frac{\epsilon}{K}N_J\epsilon_J dA_e \qquad (3.8.3)$$

The entries in the Jacobian matrix are

$$\frac{\partial f_\epsilon}{\partial K_J} = \int_{A_e}\frac{2C_\mu}{\sigma_\epsilon}\frac{K}{\epsilon}\{\frac{\partial N_i}{\partial Y}\frac{\partial \epsilon}{\partial Y} + \frac{\partial N_i}{\partial Z}\frac{\partial \epsilon}{\partial Z}\}N_J dA_e - \int_S N_i C\frac{\epsilon}{2K^{1/2}}l_y N_J dS$$
$$-\int_{A_e} N_i c_{\epsilon 1} c_\mu\{(\frac{\partial U}{\partial Y})^2 + (\frac{\partial U}{\partial Z})^2\}N_J dA_e - \int_{A_e} N_i c_{\epsilon 2}\frac{\epsilon^2}{K^2}N_J dA_e \qquad (3.8.4)$$

and

$$
\begin{aligned}
\frac{\partial f_\epsilon}{\partial \epsilon_J} &= \int_{A_e} N_i\{V\frac{\partial N_J}{\partial Y} + W\frac{\partial N_J}{\partial Z}\}dA_e \\
&+ \int_{A_e} \{\frac{\partial N_i}{\partial Y}\frac{\nu_T}{\sigma_\epsilon}\frac{\partial N_J}{\partial Y} + \frac{\partial N_i}{\partial Z}\frac{\nu_T}{\sigma_\epsilon}\frac{\partial N_J}{\partial Z}\}dA_e \\
&- \int_{A_e} \frac{c_\mu}{\sigma_\epsilon}\frac{K^2}{\epsilon^2}\{\frac{\partial N_i}{\partial Y}\frac{\partial \epsilon}{\partial Y}N_J + \frac{\partial N_i}{\partial Z}\frac{\partial \epsilon}{\partial Z}N_J\}dA_e \\
&- \int_S N_i C K^{1/2}\, N_J l_y dS + \int_{A_e} N_i c_{\epsilon 2} 2\frac{\epsilon}{K}N_J dA_e
\end{aligned}
\tag{3.8.5}
$$

where $C = (C_{\epsilon F}\, C_\mu)\,/\sigma_\epsilon$.

3.9 Numerical Integration of the Equations:

Because the 4-node element is used to approximate the velocities in this study, all terms in connection with velocities will be integrated using four-point Gaussian-quadrature. The terms associated with the penalty term are integrated with one-point Gaussian-quadrature. The K and ϵ terms are integrated using the four-point Gaussian-quadrature because they are also approximated with the 4-node element.

3.10 Solution of the System of Algebraic Equations:

The system of equations, following Schamber and Larock (1981), is divided into two groups: one for the velocities and pressure, and the other for K and ϵ. The two groups are solved sequentially rather than simultaneously. This is illustrated in the flow-chart in Fig 3.3.

The matrix form for the velocity group is

$$\{[k_1(U,V,W,k,\epsilon)]+\lambda[k_2]\}\begin{bmatrix}\Delta U\\ \Delta V\\ \Delta W\end{bmatrix}=\{f_1(U,K,\epsilon)\} \tag{3.10.1}$$

and for the K and ϵ

$$[K_3(V,W,K,\epsilon)]\begin{bmatrix}\Delta K\\ \Delta\epsilon\end{bmatrix}=\{f_2(U,K,\epsilon)\} \tag{3.10:2}$$

The matrices $[K_1 + \lambda K_2]$ and $[K_3]$ are non-symmetric and sparse. To reduce matrix storage, a non-symmetric skyline (column) storage form developed by Thompson (1979) is used.

Initial guesses are required for the variables U, V, W, K, and ϵ due to the non-linearity of the system of equations. Gauss forward elimination and back substitution technique are used to solve the two systems of equations. After each iteration the solution vector is updated via

$$\begin{bmatrix}U\\ V\\ W\end{bmatrix}^{n+1}=\begin{bmatrix}U\\ V\\ W\end{bmatrix}^{n}+\alpha\begin{bmatrix}\Delta U\\ \Delta V\\ \Delta W\end{bmatrix}^{n+1} \tag{3.10.3}$$

and

$$\begin{bmatrix}K\\ \epsilon\end{bmatrix}^{n+1}=\begin{bmatrix}K\\ \epsilon\end{bmatrix}^{n}+\alpha\begin{bmatrix}\Delta K\\ \Delta\epsilon\end{bmatrix}^{n+1} \tag{3.10.4}$$

where $\alpha = 1$ is used throughout this study.

The iteration process is stopped when the absolute sum at all the nodes of each dimensionless variable is less than a specific tolerance. A tolerance value of 10^{-3} is chosen for the velocity variables and 10^{-4} for the K and ϵ variables. This is equivalent to having accuracy in the velocities up to three significant digits and in K and ϵ up to four significant digits.

A fixed number of ten iterations within each group was used and found sufficient for obtaining partial convergence during iterating in each group. This means that after ten iterations in the velocity group for example, reasonable velocity distributions are obtained. When substituting these velocity distributions into the K and ϵ group, and iterating for ten iterations, reasonable K and ϵ distributions are obtained. A complete (final) convergence is achieved when the tolerance values in both groups are achieved.

CHAPTER IV

APPLICATION OF THE MATHEMATICAL MODEL

Different flow problems in both closed and open channels have been investigated using the finite element model developed in Chapter III. Most of the cases are chosen because experimental data was available allowing comparison between predictions and measurements. The cases studied are classified in the following manner:

4.1 Closed channels :

- 4.1.1 Square duct (1:1) with smooth walls.
- 4.1.2 Square duct (1:1) with rough walls.
- 4.1.3 Square duct (1:1) with smooth side walls, and rough top and bottom walls.
- 4.1.4 Rectangular duct (1:3) with smooth walls.
- 4.1.5 Rectangular duct (1:3) with rough walls.
- 4.1.6 Rectangular duct (1:3) with rough side walls, and smooth top and bottom walls.

4.2 Open channels with uniform bed roughness:

- 4.2.1 Rectangular (1:2) with smooth side walls and bed.
- 4.2.2 Rectangular (1:2) with rough side walls and bed.
- 4.2.3 Rectangular (1:2) with smooth side walls and rough bed.
- 4.2.4 Rectangular (1:3.94) with smooth side walls and bed.

4.2.5 Rectangular (1:4.1) with rough side walls and bed.

4.2.6 Rectangular (1:3.96) with smooth side walls and rough bed.

4.3 Open channels with periodic bed roughness and smooth side walls (1:7.5):

4.3.1 Rough stripes have roughness height of 0.0025 m.

4.3.2 Rough stripes have roughness height of 0.012 m.

4.3.3 Interchanging the smooth and rough stripes of case 4.3.1.

4.4 Open channels with uniform bed roughness and smooth side walls (1:7.5).

The effect of different geometries for square and rectangular channels with different aspect ratios, and the effect of different wall roughness conditions are represented in the above cases.

In all cases, smooth wall conditions are induced through the choice of the roughness parameter E in Equation (3.4.7) using 9.0, while for rough walls E is taken according to Equation (2.9.1.4). The transition between the two cases is taken according to Equations (2.9.1.7) to (2.9.1.9).

Because all the cases considered in this study consist of rectangular channels, use is made of the 4-node rectangular element which is simple and sufficient for representing the flow domain and the flow variables.

In all cases, the virtual boundary is located a distance 0.04 H from the walls to avoid the viscous sub-layer while remaining close to the walls. This last requirement ensures that the shear stresses evaluated at the virtual boundary are nearly equal to those at the wall. According to Sill (1982) the shear stress is nearly constant within a distance 0.06 H from the wall.

The discharge is calculated in all cases by integrating the calculated velocity distribution over the computational domain and adding the small flow in the area between walls and virtual boundaries. The velocity in this area is assumed to vary linearly from zero at the wall to its calculated value at the virtual boundary. Thus, an average velocity in this area is taken as half the average velocity along the virtual boundary. The average shear velocity along any side is obtained by integrating its calculated values along the corresponding virtual wall boundary. The overall average shear velocity or boundary shear is obtained as the weighted average over all wall boundaries.

To check convergence, the absolute sum at all the nodes of each of the normalized variables ΔU, ΔV, ΔW, ΔK, and $\Delta\epsilon$ is computed and compared to the corresponding tolerance value. As seen in Tables 4.4, 4.8, and 4.12 convergence within a tolerance of 10^{-3} for velocity variables and 10^{-4} for turbulence variables is achieved in all cases, indicating success in numerically solving the governing equations.

Because the continuity equation is globally satisfied, its local satisfaction on the element level is checked. The maximum and minimum residual of the continuity equation or incompressibility error (normalized by u_*/H) are calculated over all elements (Divmax and Divmin in Tables 4.4, 4.8, and 4.12) and are less than 10^{-6} in ducts and 10^{-8} in open channels. This indicates the success of the 4-node element with constant pressure in forcing the incompressibility constraint.

The starting values for all cases are shown in Tables 4.2, 4.6, and 4.10. The secondary velocities are initially set to zero at all nodes. K and ϵ starting values are obtained after trying several different starting values and retaining those values which bring the equations to convergence.

Two different yet similar computer codes are used: one for the closed conduit case and the other for the open channel case. The difference, as explained before, lies in using different constitutive equations for the turbulent stresses and in the open surface boundary condition for ϵ. The computer codes are run on a DEC-station 5000 (UNIX) located at Colorado State University. The running time for the programs range from one to two and a half hours depending upon the mesh size, the closeness of the starting values to the solution, and the number of computer users working on the time sharing computer system. The SURFER graphic software is used for plotting contour line graphs.

4.1 Closed Channel Cases:

The computer code for the case of closed channels applies the algebraic stress relations developed by Speziale (1987). Only a quadrant of the channel is investigated in all closed channel cases, for reasons of symmetry.

The turbulence model constants are all taken as their standard values except for C_μ whose values are shown in Table 4.1. Table 4.1 contains the input data to the computer code in the different cases while Table 4.2 contains the initial starting values needed for linearizing the system of non-linear equations. The mesh data and the number of iterations are listed in Table 4.3 and the output results for some relevant variables are presented in Table 4.4.

4.1.1 The Smooth Walled Square Duct:

The availability of several complete experimental data sets for the case of fully developed turbulent flow in a smooth square duct, suggests starting the investigation with such a case. Three different data sets are available, one by Leutheusser (1963), the second by Brundrett and Baines (1964) using the same equipment, and the third by Gessner and Emery (1980).

Brundrett and Baines (1964) experimental data is obtained from a 3 inch horizontal duct that is 70 ft long and made of plastic-coated plywood. A calibration flow nozzle and fan supplies air at room temperature. The flow Reynolds number is 83,000 with a corresponding average main velocity of 54.8 ft/sec and average main shear velocity of 2.55 ft/sec. The investigation by Brundrett and Baines provides data for the secondary velocities and turbulent stresses by utilizing a constant-current hot-wire anemometer. In a previous investigation using the same equipment, Leutheusser (1963) confirms that the flow is uniform in the plane of measurement, a distance 260 times the hydraulic diameter from the inlet, near the exit, and proceeded to measure the longitudinal velocity, wall shear stress, and static pressure distributions.

Data by Gessner and Emery (1980) reported in Demuren and Rodi (1984) shows a flow Reynolds number of 250,000. However, when considering only secondary velocities, the effect of the Reynolds number can largely be eliminated by normalizing the secondary velocities with the shear velocity rather than with the average velocity as pointed out by Launder and Ying (1972) and Demuren and Rodi (1984). This justifies comparing different secondary velocity data with different flow Reynolds numbers providing the shear velocity is used for normalizing the secondary velocity.

The value of all the constants in the computer code is taken as their standard values except C_μ, which is taken as 0.068, while its standard value is 0.09. This lower value of C_μ provides excellent agreement of the numerical results with the experimental data. The lower value of C_μ is necessary to compensate for uncertainty in the constants C_D and C_E evaluated by Speziale (1987) on the basis of two-dimensional turbulent channel data in which secondary flow is negligible.

The computational mesh used in all square duct cases is shown in Figure 4.1. The number of elements is increased near the walls where all the variables have steep gradients due to wall effects. In this case 280 iterations for each of the velocity and turbulence groups are sufficient to achieve convergence.

The predicted discharge is 0.9% higher than the measured discharge which can be considered as an excellent agreement. The maximum and minimum value of the normalized incompressibility error over all elements are in the order of 10^{-6} which shows that the continuity equation is satisfied locally as well as globally.

The value of each of ΔU, ΔV, ΔW, ΔK, and $\Delta\epsilon$ in Table 4.4 is lower than the specified tolerance, confirming the convergency of the model. Stability is confirmed by running the code up to 600 iterations and observing no significant change in the solution.

The main velocity contour lines are shown in Figure 4.2a, in which bulging of the velocity contours is much less than that measured by Leutheusser (1963) and Brundrett and Baines (1964), Figure 4.2b, indicating much less predicted secondary velocities.

However, Figure 4.3, indicates that Brundrett and Baines (1964) secondary velocities are much higher than recent data of Gessner and Emery (1980). The predicted secondary velocities shown in Figure 4.3 along the wall bisector agree very well with Gessner and

Emery's (1980) data, while the scatter of experimental data along the corner bisector indicates the difficulty in measuring the secondary velocities in that region. However, as indicated by Figure 4.3, the predicted secondary velocities with the present model along the wall bisector and the duct diagonal lie between the higher prediction by Naot and Rodi's (1982) model and the lower prediction by Demuren and Rodi's (1984) model.

The pattern of the secondary velocities is shown in Figure 4.4a, which indicates the existence of the eight-vortex structure in the duct cross section in agreement with data of Brudrett and Baines (1964) shown in Figure 4.4b. Symmetry of the calculated secondary velocities up to 12 digits indicate that there is no growth of round off errors. The maximum secondary velocity is found along the duct diagonal at the coordinate (0.69 H, 0.69 H) from the duct center with a magnitude 0.31 of the average normalizing shear velocity.

Figures 4.5, 4.6a, and 4.7 show the distribution of the turbulent viscosity, the turbulent kinetic energy, and the rate of dissipation respectively. The only published data is that for K by Brundrett and Baines (1964) as shown in Figure 4.6b, which is questionable due to inaccurate measurements of the turbulent stresses and consequently K. The predicted levels of K and ϵ have their maximum values at the walls where the velocity gradients is maximum too. The magnitude of the turbulent viscosity is high in the central area of the duct and decreases rapidly toward the walls.

The predicted distribution of the wall shear stress is shown in Figure 4.8a in which the maximum shear shifts toward the corner. The secondary motion along the wall is responsible for this shift of the wall shear. A maximum shear of 1.063 times the average shear is predicted at a distance of about 0.56 H from the corner coinciding with

Leutheusser's (1963) data in Figure 4.8b, which indicates maximum shear of 1.07 times the average shear at a distance about 0.56 H from the corner. The predicted average boundary shear is 0.98 of that measured by Leutheusser (1963).

In summary, the overall prediction of the model is excellent in spite of the complexity of the phenomenon and the large number of variables and constants involved in the model. Hence it was decided to extend the application of the model to the following cases.

4.1.2 The Rough Walled Square Duct:

The flow and mesh data used for the smooth duct case is used in the rough duct case, except that the roughness height K_s is taken equal to 0.02 ft and the roughness parameter E is taken as in Equation (2.9.1.4).

The roughness decreases the average velocity and the flow rate but increases the levels of K and ϵ, especially near the walls. Consequently, the total number of iterations is higher than that for the smooth walled duct to accommodate the higher levels of K and ϵ.

Figures 4.9 and 4.10 contain predicted main and secondary velocities. The same pattern of main and secondary velocities is observed as in the smooth duct case. However, the magnitude of the secondary velocities is slightly less than in the smooth duct case despite the much decreased average main velocity and consequently the flow Reynolds number. This lead to the conclusion that for the same Reynolds number or average main velocity, the level of secondary velocities is much higher in the case of rough square ducts than that in the case of smooth ducts as proved experimentally by

Launder and Ying (1972).

The level of the turbulent kinetic energy and of the rate of dissipation increases compared to the smooth duct due to the increase of the shear velocity at the walls. From the wall boundary conditions for K and ϵ in Equations (2.9.1.11) and (2.9.1.12), respectively, it is clear that an increase of the shear velocity along the walls increases K and ϵ. However, the same patterns for K and ϵ are observed as for the smooth walled duct.

4.1.3 The Smooth and Rough Walled Square Duct:

In this case, a roughness height of 0.02 ft is imposed only on the top and bottom walls while the side walls are left smooth. The mesh and flow data are taken as in the last two cases.

The number of iterations increases to 440 iterations because non-symmetry of roughness increases the level of turbulence anisotropy. The magnitude of the predicted main velocity or discharge is larger than that in the rough duct, but smaller than that in the smooth duct.

The non-symmetry of the roughness conditions causes the main velocity, secondary velocities, K, and ϵ to be non-symmetrical as seen in Figures 4.11-4.14. The secondary velocities (Figure 4.11) show a strong vortex at the smooth side wall while there is a very weak vortex at the rough wall. Consequently, the secondary velocities along the smooth wall bisector are much larger than along the rough wall bisector. The main velocity is larger at the smooth wall and the K and ϵ levels are larger at the rough wall.

It can be concluded that, as the magnitude of the roughness on the top and bottom walls are significantly increased and the side walls are left smooth, the vortices at the rough walls greatly diminish and there are four vortices in the duct cross section instead of eight. The advantage of this phenomena can be used in industrial applications where flows carrying suspended materials convect such materials along smooth side walls. This increased convection phenomena in mass transport can also be applied to heat transport in ducts where convection is greater at smooth walls.

4.1.4 The Smooth Walled Rectangular Duct:

A smooth walled rectangular duct with dimensions 3 by 9 inches (aspect ratio of 1:3) is discussed in this section. Data obtained by Leutheusser (1963) contains the longitudinal velocity, Figure 4.17b, and boundary shear stress, Figure 4.18b. Brundrett and Baines (1964) presented the secondary flow streamlines measured by Hoagland (1960) as in Figure 4.16b.

The computational mesh is shown in Figure 4.15 in which the number of elements is increased close to the wall to accommodate steep gradients of all variables in that region. As the computational domain is larger than that for the square duct and the number of elements and nodes are close, the number of iterations to achieve convergence increases to 920 iterations. The predictions for this case are shown in Figures 4.16 to 4.21. The value of C_μ in all the rectangular duct cases are taken as 0.075 which brings the predictions in good agreement with the experimental data.

Figure 4.16a indicates that the secondary flow in a quadrant of the duct is divided almost along the corner bisector into two vortices. This pattern agrees well with that obtained from the streamline data by Hoagland (1960) shown in Figure 4.16b. However, it is different from the secondary flow predicted by Gosman and Rapley (1980) in Figure 4.16c in which the secondary flow is not directed toward the corner.

The predicted longitudinal velocity contours (Figure 4.17a) are very similar to those reported by Leutheusser's (1963) data in Figure 4.17b. The predicted wall shear stress (Figure 4.18a) indicates a maximum value at the middle of the long wall which agrees with Leutheusser's data in Figure 4.18b. The similarity of the pattern of the predicted and measured top wall shear is evident where the predicted average boundary shear is 0.98 of that measured by Leutheusser (1963). In addition, the inflection point in the shear diagram is observed in both cases at about 1.32 H from the corner with a magnitude of 1.0 times the average shear.

The secondary flow directs the contours of the turbulent quantities ν_T, K, and ϵ towards the corner as seen in Figures 4.19 to 4.21. The error in predicting the discharge is about 3% which can be considered satisfactory.

4.1.5 The Rough Walled Rectangular Duct:

Roughness of 0.02 ft height is added to the last case of the smooth rectangular duct. The main and secondary velocities are presented in Figures 4.22 and 4.23. The general patterns for all the variables are the same as for the smooth duct. The magnitude of the secondary velocities decreases slightly when compared with the case of the smooth duct. This trend is also observed in the cases of square ducts. However, only 330 iterations which is considerably smaller than for the last case, are needed to achieve convergence.

4.1.6 The Smooth and Rough Walled Rectangular Duct:

Roughness of 0.02 ft height is added along the short sides of the smooth rectangular duct of case 4.1.4. The results are presented in Figures 4.24 - 4.28. The secondary velocities (Figure 4.24) have a strong and large vortex at the smooth wall while the vortex at the rough wall almost disappears. Thus, the same phenomena of increasing convection at the smooth walls observed in the square duct, is also observed in the rectangular duct case.

The main velocity (Figure 4.25) has steep gradients at the rough wall, as is the case for the turbulence variables ν_T, K, and ϵ as seen in Figures 4.26-4.28.

4.2 Open Channel Cases:

The main difference between closed and open channels lies in the existence of the free surface. In the model, the free surface effects are induced in the case of open channels through the algebraic-stress model of Noat and Rodi (1987) and the free surface boundary condition of Yacoub et al (1992). The algebraic surface-proximity functions given by Equations (3.1.22) and (3.1.23) are used because they are simple and do not require assumptions in regard to the mixing length.

Table 4.5 contains the input data to the model while Table 4.6 contains the starting values for the non-linear variables in the model. The mesh data and the number of iterations are reported in Table 4.7 while the output values for relevant variables are shown in Table 4.8.

In all cases, for symmetry reasons only, half of the channels are considered. The value of all the constants are taken as their standard values. Thus, the coefficient C_μ is taken equal to its standard value of 0.09 while values of 0.068 and 0.075 are used in the closed channel calculations. A detailed discussion of the open channel cases follows.

4.2.1 The Smooth Open Channel (1:2):

The flow data by Knight et. al. (1984), who measured the boundary shear stress, is used in this case. However, Knight et al. do not report measurements of the main velocity, secondary velocities, and the turbulence variables. Data by Nezu et al. (1989), exists for the main and secondary velocities but does not contain the necessary flow data such as the channel slope essential to run the computer model. Hence, the flow data by Knight et. al. (1984) is used to run the computer model and the velocity results are compared to the data by Nezu et al. (1989).

The computational mesh is shown in Figure 4.29 where the elements are increased near the walls. The results of the model calculations for this case are presented in Figures 4.30 to 4.34.

The secondary velocity structure shown in Figure 4.30a, is quite different from that of the square duct shown in Figure 4.4a. The two vortices are no longer symmetrical as in the case of the square duct. The free surface enhances the growth of the upper vortex which becomes much stronger and occupies a larger area than the lower vortex. This occurs because the free surface dampens the vertical velocity fluctuations, and by continuity enhances the horizontal velocity fluctuations.

The pattern of the secondary velocities matches well the one determined experimentally by Nezu et al. (1989) shown in Figure 4.30b, and that determined numerically by Naot and Rodi (1982) shown in Figure 4.30c. The magnitude of the secondary velocities is higher than that of the square duct due to free surface effects.

The maximum secondary velocity is in the transverse direction along the free surface, about 0.5 H from the side walls with a magnitude of 1.2 times the average normalizing shear velocity. In the square duct, the maximum secondary velocity is observed along the diagonal at the coordinate (0.69 H, 0.69 H) with a magnitude of 0.31 of the average normalizing shear velocity.

The longitudinal velocity contours shown in Figure 4.31a, indicate the success of simulating the depression of the velocity maximum which occurs at 0.61 H above the bed along the channel vertical axis of symmetry. This is in agreement with the laboratory data by Nezu et al. (1984) shown in Figure 4.31b, and the numerical simulation of Naot and Rodi (1982) shown in Figure 4.31c. Good agreement with the last two references is also achieved in the pattern of the main velocity contours.

The calculated average discharge is 5.6% higher than the measured one. This might be due to inaccuracy in the value of the measured slope used by the computer model or using standard values for the turbulence model constants. Another reason might be that Naot and Rodi's algebraic stress relations used in this model have a tendency of overpredicting main and secondary velocities.

The predicted rate of dissipation (ϵ) shown in Figure 4.32, indicates the increase of ϵ at the free surface which results from using the free surface boundary condition for ϵ by Yacoub et al. (1992). The increase of ϵ near the free surface assists in dampening the turbulent viscosity there in accord with the experimental data for the turbulent viscosity in open channels such as that by Ueda et al. (1977). The increase of the level of the turbulent kinetic energy (K) at the walls shown in Figure 4.33, is well simulated.

The shear stress distribution is shown along the bottom and side walls in Figure 4.34a and 4.34b, respectively. Along the bottom wall the shear has a maximum at the channel center as the secondary velocities are too small to induce a shifting effect. Along the side walls, the shear has a maximum at 0.46 H above the bed level while decreasing in the upward and downward directions. This is due to the existence of the strong upper free surface vortex.

4.2.2 The Rough Open Channel (1:2):

The laboratory data of Tominaga et al.(1989), run R14, is utilized in which the roughness height is 0.012 m. As mentioned before, such data are suspected to be in the fully developed region of the flow. The number of elements in the vertical direction is increased to 30 elements as shown in Figure 4.35, to achieve better simulation of free surface effects.

The secondary and main velocities are presented in Figures 4.36 and 4.37. The same secondary velocity pattern and magnitude is observed as in the smooth channel. The main velocity maximum occurs at 0.57 H above the bed on the channel vertical axis of symmetry. This lowering of the maximum velocity in comparison to the last case is due to the increase in the downflow along the channel vertical axis of symmetry.

4.2.3 The Smooth Side Walls and Rough Bed Open Channel (1:2):

This case includes a roughness of 0.012 m only along the bed of the smooth channel in case 4.2.1 . The mesh used in case 4.2.2, is used in this case. Figures 4.38 and 4.39 contain the prediction of the secondary and main velocities.

The significant difference in this case compared with the last two cases, is that the velocity maximum occurs at the free surface and that the magnitude of the secondary velocities decreases. The strength and size of the lower corner vortex decreases remarkably compared with the last two cases. The weak down flow along the channel axis of symmetry is not capable of depressing the velocity maximum as seen in Figure 4.39.

4.2.4 The Smooth Rectangular Open Channel (1:3.94):

To investigate the effect of geometry in the form of different aspect ratios of rectangular open channels, the aspect ratio in this case is considered as nearly double that in the last three cases. The same type of roughness conditions on the side walls and bed used for the last three cases is considered in this case and the next two cases.

The flow data of Tominaga et al. (1989), run S2, is utilized in this case. The computational mesh is shown in Figure 4.40, and the predictions are presented in Figures 4.41 to 4.45.

The secondary velocity structure shown in Figure 4.41a, is composed of a large upper vortex extending to a length 1.37 H from the side wall and a weak lower vortex. There are very little secondary velocities in the middle part of the channel. This pattern agrees with the numerical results of Naot an Rodi (1982) shown in Figure 4.41b, but is different from the laboratory data of Tominaga et al. (1989) shown in Figure 4.41c. The two vortices in Figure 4.41c are nearly equal in size and the division between them occurs at a height of 0.6 H above the bed. The pattern in Figure 4.41c does not show neither the corner effects of directing the flow to the corner, nor the free surface effects in the form of having a large upper vortex.

The main velocity maximum along the channel vertical axis occurs on the free surface as shown in Figure 4.42, where the secondary flow is too weak to depress the velocity. The levels of K and ϵ increase at the walls as seen from Figures 4.43 and 4.44.

The shear stress on the bottom wall has a maximum at 0.6 H from the channel center while decreases dramatically toward the corner and the channel center as seen in Figure 4.45a. Along the side walls the shear stress has a maximum at 0.5 H above the bed and decreases gradually toward the bed and free surface as in Figure 4.45b. The predicted discharge is 4.3% higher than the measured one.

4.2.5 The Rough Rectangular Open Channel (1:4.1):

The flow data of Tominaga et al. (1989), run R13, is utilized in which the roughness height is 0.012 m along the side and bottom walls. The same number of elements used for the last case is used in this case too. However, difficulty arises in obtaining a converged solution due to the high levels of turbulence associated with the increased roughness on the walls. Convergence can only be obtained after initially running the code for the first forty iterations assuming all the walls smooth, and then imposing the roughness. This assists in obtaining better initial starting distributions for the non-linear variables.

The secondary and main velocities are presented in Figures 4.46 and 4.47. The upper vortex occupies a distance of 1.71 H measured from the side wall which is larger than the upper vortex in the smooth rectangular open channel case. The maximum main velocity is observed at the free surface as in the last case. There is no remarkable difference in the pattern of any of the other variables when compared with the last case.

4.2.6 The Smooth Side Walls and Rough Bed Rectangular Open Channel (1:3.96):

The flow data of Tominaga et al. (1989), run R22, is utilized in this case. It takes 900 iterations for the solution to converge on a 20 by 30 mesh.

The secondary and the main velocity predictions are shown in Figures 4.48 and 4.49. Figure 4.48 shows that the upper vortex occupies a smaller area than in the last two cases. The upper vortex extends to a distance 1.12 H from the side wall. A weak third vortex exists in the middle part of the channel and pushes the longitudinal velocity contour upward along the channel vertical axis of symmetry as seen in Figure 4.49. The predicted discharge is 0.08% less than the measured one which is very satisfactory.

4.3 Rectangular Open Channels with Periodic Roughness (1:7.5):

To investigate the effect of periodic roughness in open channels, calculations are performed and compared with existing experimental data. The experiments are carried out by Muller and Studerus (1979) in a 25 m long, 0.6 m wide, tilting flume with an aspect ratio of 1:7.5 shown in Figure 4.50. Four 20 m long and 0.06 m wide stripes of roughness are fixed 10 cm apart along the floor of the channel. The rough parts have a roughness height of 0.25 cm while the rest of the channel is hydraulically smooth.

The average measured main velocity is 55 cm/sec and the flow depth is kept at 8 cm which is half the spacing of the rough stripes. The flow Reynolds number is 44000 while the Froude number is 0.6. To obtain uniform flow, the slope is adjusted to 0.00152 giving a shear velocity of 3.1 cm/sec. Muller and Studerus report the measurements in the central cell at -16 cm < Z < 0 cm.

In the developed mathematical model, a cubic algebraic surface proximity functions are used in channels with periodic roughness. Otherwise negative values of K and ϵ appear. In addition, the calculations are performed for at least forty iterations assuming all the side walls and the bed smooth and then adding the rough stripes to the bed. This process is necessary to avoid negative values for K and ϵ, and to allow for gradually obtaining a better initial distributions of K and ϵ.

In all the following cases, the mesh shown in Figure 4.51 is used in which the elements are graded in the transverse direction to accommodate the periodic roughness. Table 4.9 contains the input data to the computer code while Table 4.10 contains the starting values. The mesh data and the number of iterations are in Table 4.11, and the output results for relevant variables are given in Table 4.11. In the following sections, three different cases are discussed.

<u>4.3.1 The Rectangular Open Channel with Periodic Roughness (k_s=0.0025 m):</u>

The results of the calculations for this case are shown in Figures 4.52 to 4.56.

The pattern of the secondary velocities shown in Figure 4.52a, consists of a cellular structure with the flow directed downward over the two central rough stripes and upward over the smooth stripes. This agrees with the data for the central cell by Muller and Studerus (1979) shown in Figure 4.52b, and the numerical simulation by Naot (1984) shown in Figure 4.52c.

Close to the side walls, the two vortex structure with a large upper vortex and a small lower one is observed. This structure is similar to the case of rectangular channels with uniform bed roughness.

The contours of the main velocity shown in Figure 4.53a, are pushed downward over the central rough stripes by the secondary velocity, and pushed upward over the adjacent smooth stripes. This distribution is similar to that of Naot (1984) shown in Figure 4.53b, including having the velocity maximum at the surface. The data of Muller and Studerus (1979) shown in Figure 4.53c, indicates that the velocity maximum is below the free surface. However, Naot (1984) implies that the data of Studerus (1982) has the maximum velocity on the surface.

A wavy pattern of the wall shear stress is observed as shown in Figure 4.54a in which the shear stress adjusts quickly to the discontinuous change of the bed roughness with a peak over the central rough strip equal to double that at the adjacent smooth one. This is in line with the experimental observation of Hwang and Nickerson (1972) in the flat plate periodic roughness experiment. If sediment is allowed to be transported by the flow, a wavy pattern of transverse sediment distributions results with ridge and trough formations. The side wall shear stress shown in Figure 4.54b, has a similar distribution to case 4.2.1 and a maximum at a distance 0.55 H above the bed.

The turbulent kinetic energy (Figure 4.55a) is similar to that obtained numerically by Naot (1984) shown in Figure 4.55b, where high levels of turbulence are observed over the rough stripes. Also, for the dissipation rate ϵ, high levels are observed over the rough stripes. The predicted discharge is 2.8% less than the measured one and it takes 300 iterations or 68 minutes of computer time to achieve convergence.

4.3.2 The Rectangular Open Channel with Periodic Roughness (K_s =0.012 m):

The roughness in the last case is increased from 0.0025 m to 0.012 m to investigate the effect of increasing the magnitude of the roughness on the flow structure.

The pattern of the secondary velocities is the same except of the disappearance of the lower corner vortex as shown in Figure 4.57. The level of the turbulence anisotropy is higher in this case than the last case due to the bigger difference in roughness magnitude between the rough and the smooth stripes. As a result, the magnitude of the secondary velocities is significantly higher in this case. The magnitude of the maximum horizontal secondary velocity along the free surface increases from 0.73 u_* (directed from the side wall to the channel center) in the last case to 0.85 u_* in this case due to the increasing difference of the roughness magnitude between the rough and the smooth stripes. Also, the maximum vertical secondary velocity along the channel vertical axis of symmetry increases from 0.35 u_* (directed in the downward direction) in the last case to 0.85 u_* in this case.

The main velocity contours (Figure 4.58) have increased bulging toward the rough stripes and away from the smooth ones. This higher bulging is also true for the turbulent quantities K and ϵ as seen in Figures 4.59 and 4.60, respectively.

The bed shear stress has in this case much higher peaks than in the last case as seen in Figure 4.61 where the shear on the rough stripes is 4.5 times that on the adjacent smooth one.

4.3.3 Interchanging the Rough Stripes with the Smooth Ones in Case 4.3.1:

The secondary velocities in this case are shown in Figure 4.62. As the rough stripes are replaced with smooth ones and vice versa, the pattern of all the variables changes correspondingly. For example, the secondary velocity pattern adjusts by directing the flow downward over the rough stripe in the middle of the channel and upward over the adjacent smooth one. The secondary motion is greatly diminished over the rough stripe at 12 cm $< Z <$ 20 cm.

An interesting difference is that the two vortices at the corner occupies the same area. This is due to the existence of the roughness at the corner which increases the secondary motion and consequently the lower corner vortex becomes larger.

The main velocity contours (Figure 4.63) also adjusts to the pattern of secondary velocity by bulging downward over the rough stripes and upward over the smooth ones.

4.4 The Wide Rectangular Channels with Uniform Bed Roughness (1:7.5):

To verify that the cellular secondary structure obtained in the last three cases is due to the periodic variation of the roughness and not due to the channel being relatively wide, the following two cases are investigated. In both cases, the same rectangular channel studied by Muller and Studerus (1979) is investigated but with uniform roughness all over the channel bed while the side walls are left smooth. The input data, starting values, mesh data, and output results are reported in Tables 4.9, 4.10, 4.11, and 4.12, respectively.

The first case has a roughness height of 0.0025 m and the second has a roughness height of 0.012 m, both uniform over the full width. The secondary velocities in each case are shown in Figures 4.64 and 4.65. The cellular secondary structure disappears, and instead, two vortices at the side wall peculiar to rectangular channels with uniform bed roughness are observed with a large upper vortex and a small lower one. The upper vortex extends to a distance about 1.15 H to 1.1 H from the side wall in the cases of 0.0025 m and 0.012 m bed roughness, respectively. Therefore, it is evident that the cellular secondary structure could only be predicted in channels with periodic roughness.

Very weak secondary velocities beyond the upper vortex are observed which could not affect the main velocity contour lines as seen in Figures 4.66 and 4.67. The main velocity distribution in this part of the channel can be assumed two-dimensional where the secondary flow can be neglected.

CHAPTER V

CONCLUSIONS

The present study has been carried out with the specific goal of investigating three-dimensional turbulent flow problems in closed and open channels. Consideration is given to the effect of secondary velocities on the primary velocity and boundary shear.

A finite element computer model was developed and proves successful in solving the Reynolds equations of motion and continuity. The model effectively predicts the three velocity components, boundary shear stress, turbulent kinetic energy, and rate of dissipation in both cases of closed and open channels. Channels are straight and rectangular.

The following conclusions are drawn from this study:

1. The 4-node bilinear element approximating the velocities, K, and ϵ with a single point quadrature for the pressure, performs well in solving turbulent flow problems. In addition, the iterative penalty approach proves efficient with respect to enforcing the incompressibility constraint and economical with respect to computer storage and time.

2. The common approach of dividing the turbulent flow governing equations into two groups, one for the velocities and pressure and the other for K and ϵ, proves sufficient and economical as the number of equations solved at one time is remarkably reduced.

3. The non-linear problems such as the turbulent flow considered herein, are very sensitive to initial starting values. The solution of a problem with simple boundary conditions

can be the initial distribution to a similar non-linear problem but with a more complicated boundary conditions.

4. The two equation model (K-ϵ) proves successful in predicting the primary and secondary flow structure in closed and open channels with different geometries and wall roughnesses. Convergence of the K and ϵ equations was obtained even in the complex cases considered in this study. This explains the success and popularity of the K-ϵ turbulence model in solving turbulent flow problems using the finite element method.

5. The algebraic stress models are sufficient for predicting primary and secondary velocities in both closed and open channels. In addition, they are much more economical than the differential stress transport models.

6. The algebraic stress model of Speziale (1987) is capable of correctly predicting the pattern and magnitude of corner-induced secondary motions in square and rectangular ducts.

7. The algebraic stress model of Naot and Rodi (1982) with simple algebraic surface proximity functions effectively predicts secondary motions in rectangular open channels. The same model is successful in predicting the cellular secondary structure induced by the periodic roughness in open channels. The free surface boundary condition for ϵ, developed by Yacoub et al. (1992), simulates well the effect of the free surface which increases the dissipation at the surface.

8. The corner secondary motions in smooth and rough square ducts are numerically found responsible for bulging the primary velocity contours to the corner and shifting the wall shear maximum toward the corner. The eight vortex structure is successfully predicted in the square and rectangular duct cases. The uniform roughness does not change the pattern of the secondary

motion but only increases the magnitude of the secondary motion. The secondary motion in rectangular ducts differs from that in square ones only in having one larger corner vortex extending in the direction of the long side of the duct. All these model predictions are confirmed by experimental findings.

9. In square and rectangular ducts with two opposite smooth walls and two opposite rough walls, the vortices at the smooth walls become much stronger than those at the rough walls. The vortices at rough walls nearly diminish when increasing the roughness.

10. The secondary motions in smooth and rough walled open channels with aspect ratio (1:2) are different from that of square ducts. The two corner vortices are no longer symmetrical with stronger and larger upper one. The upper vortex causes the main velocity maximum along the channel vertical axis of symmetry to be depressed below the free surface. All these results are confirmed by experimental findings.

11. In rectangular open channels with aspect ratio about (1:4), the upper vortex extends some length (1.12 H to 1.71 H) from the side walls, depending upon the wall roughness conditions, and the main velocity maximum is on the free surface. In wide rectangular open channels (1:7.5) with uniform bed roughness, only the two corner vortices exist with the upper one extending a distance of 1.10 and 1.15 H from the side wall in the cases of bed roughness of 0.012 m and 0.0025 m, respectively.

12. The cellular secondary structure across the full width is produced only by the periodic roughness of the channel bed. The primary, secondary velocities, K and ϵ are directed downward over the rough stripes and upward over the smooth ones confirming experimental findings.

CHAPTER VI

RECOMMENDATIONS

The present study highlights the effect of the secondary velocities on the main velocity and boundary shear distributions for turbulent flows in closed and open channels. The study also shows how modelling of a turbulent flow phenomena and a solution are successfully obtained. However, certain assumptions, selections, and methodologies were made which could be improved. In the following some recommendations are presented for improving the predictive capabilities of the present mathematical model. In addition, other applications and further modifications of the present computer model are recommended that are of interest to scientists and engineers. The recommendations are:

1. A more complete investigation of all the constants in the turbulence model should be carried out. Special attention should be given to C_μ which in the present model is 0.068 in square ducts, 0.075 in rectangular ducts, and 0.09 in open channels. The values chosen in ducts are selected on the basis of obtaining better agreement with experimental data. However, for open channels, no attempts were made for finding an optimum value for C_μ. Since agreement with experimental data is not as good in the cases of open channels as in the duct cases, studies are needed to find the optimum values for C_μ. In addition, the two constants C_E and C_D in Special's (1987) algebraic stress relations need to be determined experimentally based upon data of three-dimensional flows with secondary motions.

2. The cases considered in this study should be further investigated using different elements such as the 8-nodded element with four quadrature points for the pressure and the 9-nodded element with single quadrature point for the pressure. A comparison study could then test the performance of each of these elements.

3. The effect of the secondary motions on the three-dimensional sediment distributions such as sand ridges and troughs on the bed of open channels should be investigated. This might prove that in open channels carrying bed load, the two corner vortices will initially deposit sediment (ridge) in the corner region, which alters the turbulence structure especially the primary shear stresses and consequently the primary velocity. This might cause development of another vortex and by continuity a counter-rotating one might develop too. The new couple of vortices again might deposit sediment in the form of a new ridge which affects the primary shear stresses and the primary velocity. This process might continue until the bed of the channel is covered with sediment ridges and troughs with associated cellular secondary structure. To simulate this process, the effects of the secondary velocities on the primary shear stresses should be included.

4. The present model should be applied to channels with existing ridges, and troughs to investigate the cellular secondary structure effects.

5. Different channel shapes of cross sections such as triangles, trapezoidals, and arbitrary cross sections should be tried with the present model.

6. The current model should be applied to investigate the flow in compound channels or channels with flood plain. The flood plain and main channel interactions through the secondary

motion should be addressed in the investigation.

7. The model should be modified to accommodate many practical flow problems such as secondary motions in developing flows, secondary motions in unsteady flows, flow in curved channels, flow in channel constrictions, flow in sedimentation tanks, flow over sand dunes, flow over weirs, flow over spillways, flow under sluice gates, jet flows, stratified flows, and flow in cavities.

8. The convergence characteristics of the K-ϵ model and the possibility of negative unreal solutions should be investigated in detail.

9. Methods for solving non-linear equations which are not sensitive to the starting values should be investigated.

10. Methods for determining the best starting values for the non-linear equations need to be developed.

11. Methods for recovering the pressure field using suitable filtering techniques should be added to the present model.

12. Based upon the current model predictions, the correction procedure of Vanoni and Brooks (1957) to account for the side wall effects in laboratory flumes could be improved. In this procedure, the weak assumption that the average velocities are equal in the cross sectional subareas can be corrected by using the calculated averages from present model predictions of the main velocity.

APPENDIX A

SELECTED BIBLIOGRAPHY

SELECTED BIBLIOGRAPHY

Autret, A., Grandotto, M., and Dekeyser, I. (1987). "Finite Element Computation of a Turbulent Flow over a Backward-facing Step." Int. J. Numer. Meth. in Fluids, 7, 89-102.

Bathurst, J.C. (1979). "Distribution of Boundary Shear Stress in Rivers."Proceedings of the tenth annual geomorphology symposia, N.Y.

Brundrett, E., and Baines, W. D. (1964). "The Production and Diffusion of Vorticity in Duct Flow." J. Fluid Mech., 19, 375-392.

Buleev, N.I, (1963). "Theoretical Model of the Mechanism of Turbulent Exchange in Fluid Flows." AERE Transl. 957.

Celik, I., and Rodi, W. (1988). "Modeling Suspended Sediment Transport in Non-Equilibrium Situations." J. Hydr. Engng., ASCE, 114, 1157-1191.

Culbertson, J.K. (1967). "Evidence of Secondary Circulation in an Alluvial Channel." U.S. Geological Survey, Prof. Paper 575-D, pp. D 214-D 216.

Demuren, A.O., and Rodi, W. (1984). "Calculation of Turbulence-driven Secondary Motion in Non-circular Ducts." J. Fluid Mech.,140, 189-222.

Devantier, B.A., and Larock, B.E. (1986). "Modelling a Recirculating Density-driven Turbulent Flow" Int.J. Numer. Meth. in Fluids, 6, 241-253.

Einstein, H.A., and Li, H. (1958). "Secondary Currents in Straight Channels." Trans., American Geophysics Union, 39, 1085-1088.

Finnie, I. J. and Jeppson, W. R. (1991)."Solving Turbulent Flows Using Finite Elements" J. Hydr. Engng., ASCE, 117, 1513-1530.

Gessner, F.B., and Emery, A.F. (1980). "The Numerical Prediction of Developing Turbulent Flow in Rectangular Ducts." Turbulent Shear Flows 2, Springer, (ed. J.S. Bradbury et al.).

Gessner, F.B., and Jones, J.B. (1965). "On Some Aspects of Fully-developed Turbulent Flow in Rectangular Channels. " J. Fluid Mech., 23, part 4, 689-713.

Gosman, D.D., and Rapley, C.W. (1978). "A Prediction Method for Fully Developed Flow through Non-circular Passages." In Numerical Methods in Laminar and Turbulent Flows (ed. C. Taylor et al.) Pentech.

Gosh, S., and Roy, N. (1970). "Boundary Shear Distribution in Open Channel Flow." J. Hydr. Div., ASCE, 96, 967-994.

Gresho, P.M., and Lee, R.L. (1981). "Don't Suppress the Wiggles-They're Telling You Something." Comput. Fluids, 9, 223-253.

Gresho, P.M., Lee, R. L., and Sani, R. L. (1980)."On the Time Dependent Solution of the Incompressible Navier-Stokes Equations in Two and Three Dimensions." Recent advances in numerical methods in fluids, 1, C.Taylor and K. Morgan, eds., Pineridge press ltd., Swansea,U.K.

Hanjalic, K., and Launder, B.E. (1972). "A Reynolds Stress Model of Turbulence and its Application to Thin Shear Flows." J. Fluid Mech., 52, 609-638.

Haroutunian, V., and Engelman, M.S. (1989). "Recent Experience with Simulating Turbulent Flows in a Finite Element Context Using a Two-equation Turbulence Model." Proc. Seventh Int. Conf. on finite element methods in flow problems, 1551-1564.

Hawng, Li-San and Laursen E.M. (1963)."Shear Measurement Technique for Rough Surfaces" J. Hyd. Div., ASCE, 89, 19-37.

Hossain, M. S. (1980)."Mathematische Modellierung von Turbulenten Auftriebsströmungen." thesis presented to the University of Karlsruhe, in Karlsruhe, West Germany, in partial fulfillment of the requirements for the degree of Doctor of philosophy.

Hue W., and Nickerson, E.C. (1972). "Response of a Turbulent Boundary Layer to Lateral Roughness Discontinuities." Report THEMIS-18, Colorado State University, Fort Collins, Co.

Hutton, A.G., Smith, R.M., and Hickmott, S. (1987). "The Computation of Turbulent Flows of Industrial Complexity by the Finite Element Method-Progress and Prospects." Int. J. Numer. Meth. in Fluids, 7, 1277-1298.

Kacher, S.C. (1973). Discussion of "Prediction of Flow and Heat Transfer in Ducts of Square Cross-section." Proc. Inst. Mech. Engng 187, D 147-D148.

Karcz, I. (1973). "Reflections on the Origin of Source Small-scale Longitudinal

Streambed Scours." Fluvial Geomorphology, M. Morisawa, ed., Proceedings of the fourth annual geomorphology symposia series, pp. 149-173.

Keller, R.J. and Rastogi, A.K. (1975)."Prediction of Flow Development on Spillways." J. Hydr. Div., ASCE, HY9, 1171-1184.

Kinoshita, R. (1967)."An Analysis of the Movement of Flood Waters by Aerial Photography; Concerning Characteristics of Turbulence and Surface Flow." Photographic surveying, 6, 1-17 (in Japanese).

Krishnappen, B.G., and Lau, Y.L. (1986). "Turbulence Modelling of Flood Plain Flows." J. Hydr. Engng., ASCE, 112 (4), 251-267.

Launder, B. E., Reece, G. J., and Rodi, W. (1975)."Progress in the Development of a Reynolds-stress Turbulence Closure." J. Fluid Mech., 68, 357-566.

Launder, B. E., and Spalding, D. B. (1974)."The Numerical Computation of Turbulent Flow." Computer Methods in Applied Mechanics and Engineering, vol.3, 269-289.

Launder, B.E., and Ying, W.M. (1972). "Secondary Flows in Ducts of Square Cross-section." J.Fluid Mech. 54, pp. 289-295.

Launder, B.E., and Ying, W.W. (1973). "Prediction of Flow and Heat Transfer in Ducts of Square Cross-section." Proc. Inst. Mech. Engr. 187, 455-461.

Leschziner, M.A., and Rodi, W. (1979)."Calculation of Strongly Curved Open Channel Flow." J. Hydr. Div., ASCE, vol 105, HY10, 1279-1314.

Leutheusser, J. H. (1963). "Turbulent Flow in Rectangular Ducts" J. Hydr. Div., ASCE, , 89, 1-19.

Magnaud, J.P. , and Goldstein, S. (1989). "The Finite Element Version of the Trio Code." presented at the seventh intr. conf. on finite element methods in flow problems, Huntsville, Ala., Apr. 3-7.

Melling, A., and Whitelaw, J.H. (1976). " Turbulent Flow in a Rectangular Duct." J. Fluid Mech., 78, 289-315.

Muller, A., and Studerus, X. (1979). "Secondary Flow in Open Channel." Proc., Congress of the IAHR, Italy, pp 19-24.

Naot, D. (1984). "Response of Channel Flow to Roughness Hetrogeneity." J. Hydr. Engng., ASCE, 110, 1568-1587.

Naot , D., and Emrani, S. (1983). "Numerical Simulation of the Hydrodynamic Behavior of Fuel Rod with Longitudinal Cooling Fins." Nuclear Engng. and Design, vol. 73.

Naot, D., and Nezu, I., and Nakagawa, H. (1993). "Hydrodynamic Behavior of Compound Rectangular Open Channels." J. Hydr. Engng., ASCE, 119, 390-408.

Naot, D., and Rodi, W. (1982). "Calculation of Secondary Currents in Channel Flow." J. Hydr. Div., ASCE, vol. 108, 948-968.

Naot, D., Shavit, H., and Wolfshtein, M. (1974). "Numerical Calculation of Reynolds Stresses in a Square Duct with Secondary Flow." Wärme-und-stoffübertragung 7, 151-161.

Nezu, I., and Nakagawa, H. (1984). "Cellular Secondary Currents in Straight Conduit." J. of Hydr. Engrg., ASCE, 110, pp 173-193.

Nezu, I., and Nakagawa, H., and Rodi, W. (1989). "Significant Difference of Secondary Currents in Closed Channels and Narrow Open Channels." Proc, 23rd IAHR Congress, Ottawa, A, 125-132.

Nezu, I., and Rodi, W. (1985). "Experimental Study on Secondary Currents in Open Channel Flow." Proc., 21 st Congress of IAHR, Melbourne, 2, 115-119.

Nezu, I., Tominaga, A., and Nakagawa, H. (1993). " Field Measurements of Secondary Currents in Straight Rivers." J. Hydr. Engrg., ASCE, 119, 598-614.

Nikuradse, J. (1926). "Turbulente Strömung im Innern des Rechteckigen Offenen Kanals." Forschungsarbeiten, Heft 281, pp 36-44.

Polansky, G.F., Lamb, J. P., and Crawford, M.E. (1984). "A Finite Element Analysis of Incompressible Turbulent Backstep Flow with Heat Transfer." AIAA paper No.84-0178.

Prandtl, L. (1925). "Über die Ausgebildete Turbulenz." ZAMM, 5, P.136.

Preston, J.H. (1954). "The Determination of Turbulent Skin Friction by Means of Pitot Tubes" J. of the Royal Aeronautical Society, vol. 54, Feb., 1954.

Ramachandra, V. (1979). "The Numerical Prediction of Flow and Heat Transfer in Rod-bundle Geometries." Ph.D. thesis, University of London.

Reece, G.J. (1979). "A Generalized Reynolds-Stress Model of Turbulence." Ph.D. thesis, University of London,1977.

Rodi, W. (1984). "Turbulence Models and Their Applications in Hydraulics_ A

State of the Art Review." IAHR publication, Delft, The Netherlands.

Shamber, D. R., and Larock , B. E. (1981). "Numerical Analysis of Flow in Sedimentation Basins." J. Hydr. Div., ASCE, 107(5), 575-591.

Sharma, M., and Carey, G.F. (1986). "Turbulent Boundary-layer Analysis Using Finite Elements." Int. J. Numer. Meth. in Fluids, 6, 769-787.

Sill, B.L. (1982). "New Flat Plate Turbulent Velocity Profiles." J. Hydr. Engrg., ASCE, 108, pp 1-14.

Smith, R.M. (1984a). "On the Finite Element Calculation of Turbulent Flow Using the K-ϵ Model." Int. Numer. Meth. in Fluids, 6, 303-319.

Speziale, C. G. (1987). "On Non-Linear L-l and K-ϵ Models of Turbulence." J. Fluid Mech., 178, 459-475.

Studerus, X. (1982). "Sekundärströmungen im offenen Gerinne über Rauhen Längsstreifen." R19-82 report, ETH Zurich, Switzerland, May, 1982.

Svensson, U. (1978). "Mathematical Model of the Seasonal Thermocline." University of Lund, Dept. of Water Resources Engng., Sweeden, Rept. No. 1002.

Taylor, C., Thomas, C.E., and Morgan, K. (1981). "Modelling Flow over a Backward-facing Step Using the F.E.M. and the Two-equation Model of Turbulence." Int. J. Numer. Meth. in Fluids, 7, 89-102.

Tominaga, A., Nezu, I., Ezaki, K., and Nakagawa, H. (1989). " Three-dimensional Turbulent Structure in Straight Open-channel Flows." J. Hydr. Res., IAHR, 27, 149-173.

Tong, G.D. (1982). "Computation of Recirculating Flows in two Dimensions Using Finite Elements and the K-ϵ Model." Proc. First IAHR Symp. on Refined Modelling of Flows, Paris, France.

Thompson, E. (1978). "The Finite Element Method." Class notes of CE665, Colorado State University, Ft. Collins, Co.

Thomson, J. (1878). "On the Flow of Water in Uniform Regime in Rivers and Other Open Channels." Proc., Royal Society, vol. 191, 1878.

Ueda, H., Moller, R., Komori, S., and Mizushina, T. (1977). "Eddy Diffusivity Near the Free Surface of Open Channel Flow." Int. J. of Heat and Mass Transfer, vol. 20, 1127-1136.

Vanoni, V.A. (1946). "Transportation of Suspended Sediment by Water." Trans., ASCE, 111, 67-133.

Yacoub, N., Moalem, M.D., and Naot, D. (1992). "Towards the Numerical Simulation of the Horizontal Slug Front." Int. J. Numer. Meth. in Fluids, 14, 127-146.

Zienkiewicz, O.C. (1989). "The Finite Element Method." McGraw-Hill, fourth edition, vol. 1.

APPENDIX B

FIGURES

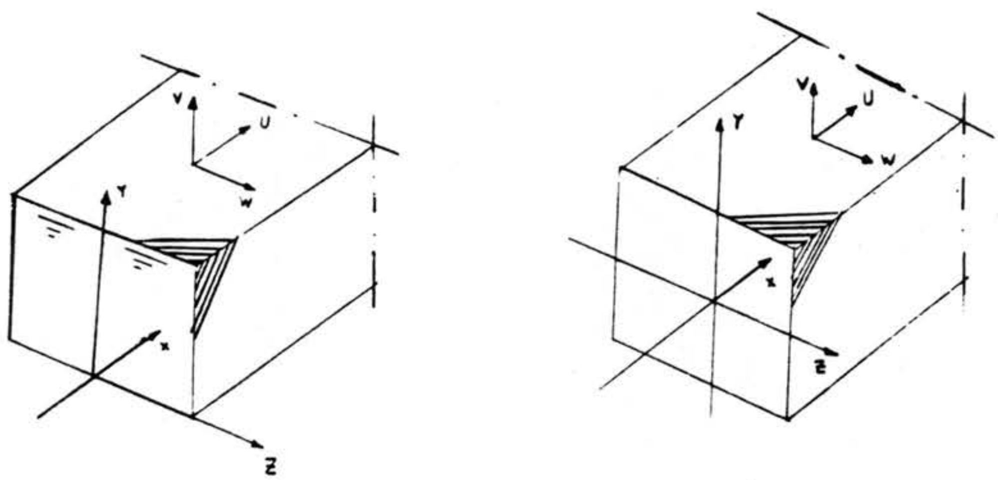

Open Channel

Closed Channel

Figure 2.1 Co-ordinate Axes in Closed and Open Channels.

$$\begin{bmatrix} \frac{\partial f_U}{\partial U} & \frac{\partial f_U}{\partial V} & \frac{\partial f_U}{\partial W} \\ \frac{\partial f_V}{\partial U} & \frac{\partial f_V}{\partial V} & \frac{\partial f_V}{\partial W} \\ \frac{\partial f_W}{\partial U} & \frac{\partial f_W}{\partial V} & \frac{\partial f_W}{\partial W} \end{bmatrix} \begin{bmatrix} dU \\ dV \\ dW \end{bmatrix} = \begin{bmatrix} -f_U \\ -f_V \\ -f_W \end{bmatrix}$$

Figure 3.1 a Jacobian Matrix for X, Y, and Z Momentum Equations.

$$\begin{bmatrix} \frac{\partial f_k}{\partial k} & \frac{\partial f_k}{\partial \epsilon} \\ \frac{\partial f_\epsilon}{\partial k} & \frac{\partial f_\epsilon}{\partial \epsilon} \end{bmatrix} \begin{bmatrix} dk \\ d\epsilon \end{bmatrix} = \begin{bmatrix} -f_k \\ -f_\epsilon \end{bmatrix}$$

Figure 3.1b Jacobian Matrix for K and ϵ Transport Equations.

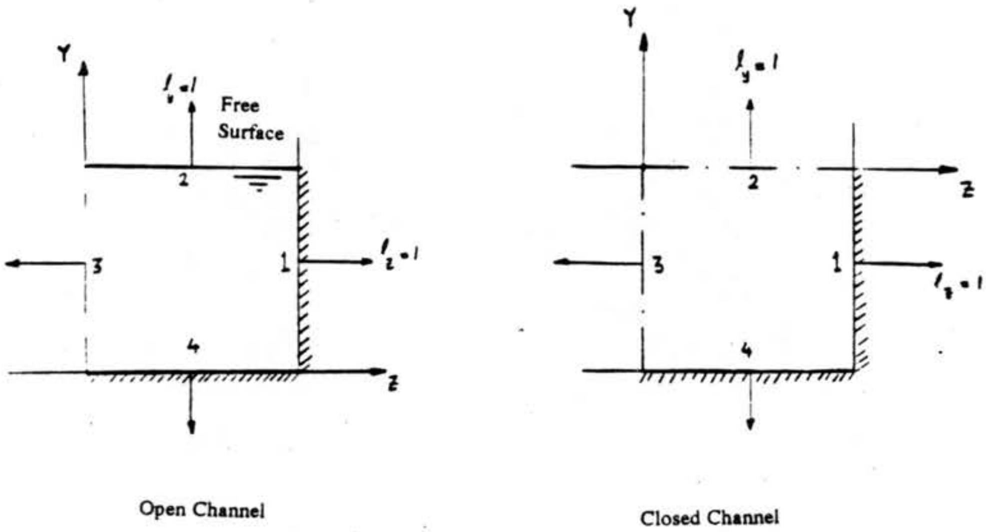

Figure 3.2 Domain of closed and open Channels.

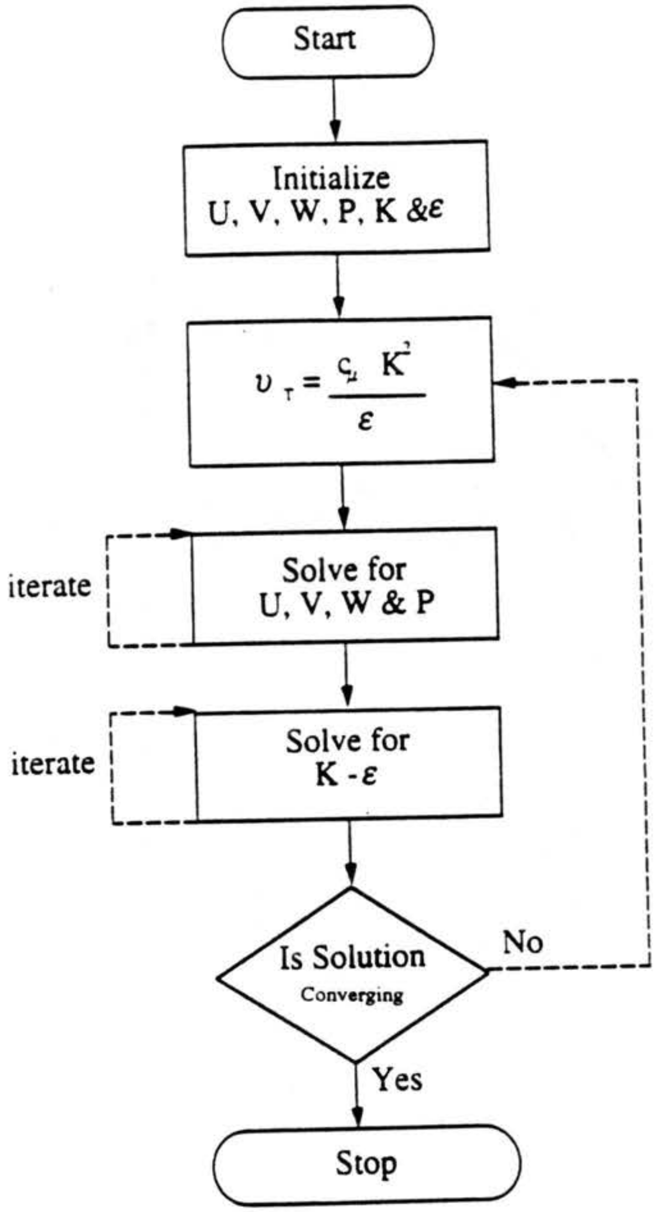

Figure 3.3 Flow Chart of the Main Steps of the Computer Model.

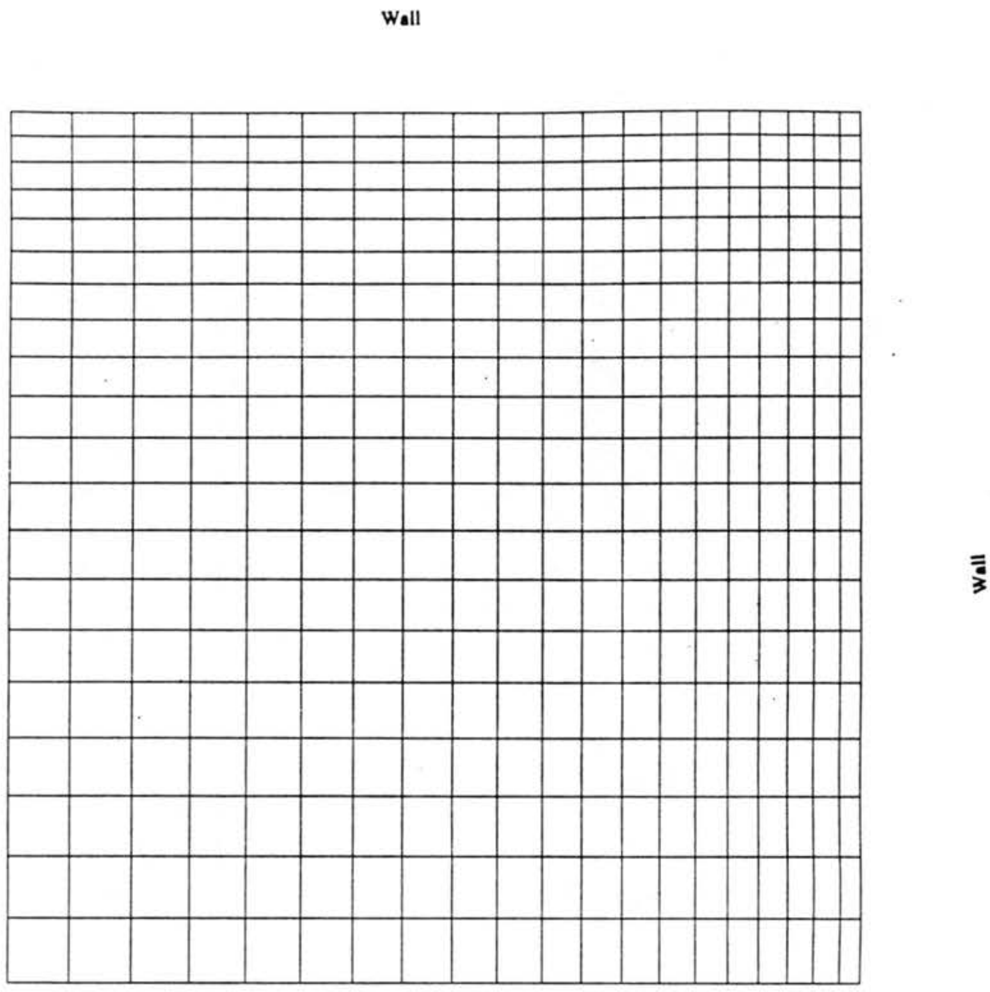

Figure 4.1 The Mesh for the Square Duct Problem. (One quarter of the duct. Centerlines are to the left and bottom of the graph.)

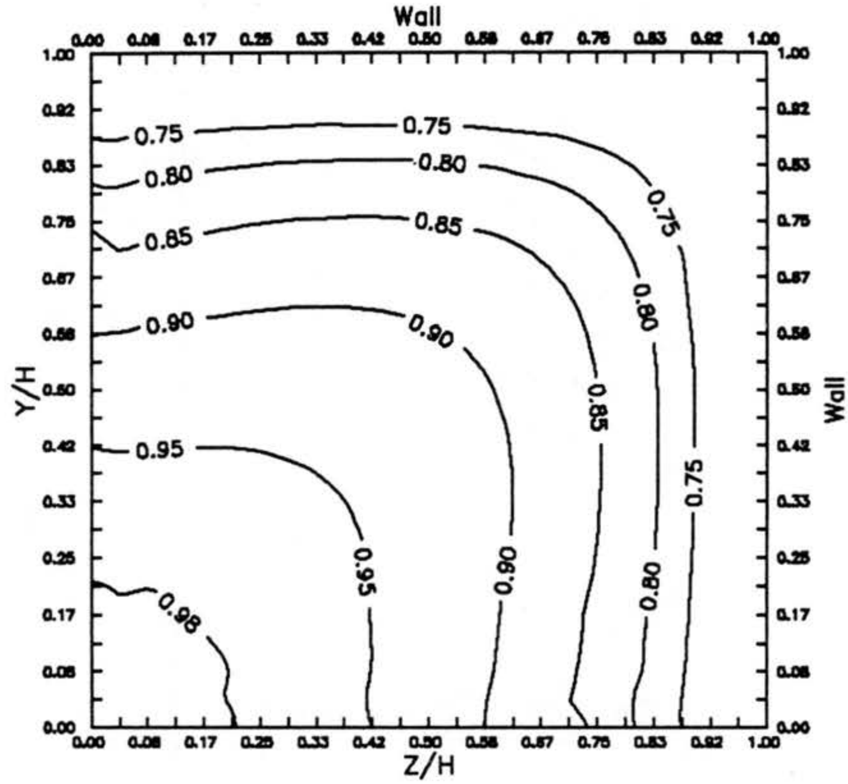

Figure 4.2a Predicted Main Velocity Contour Lines (Normalized by the centerline velocity U_{cl}) for the Flow in a Smooth Square Duct. $H = 1.5$ in, $U_{cl} = 65.9$ ft/s, and $R_e = 83,000$. (One quarter of the duct. Centerlines are to the left and bottom of the graph.)

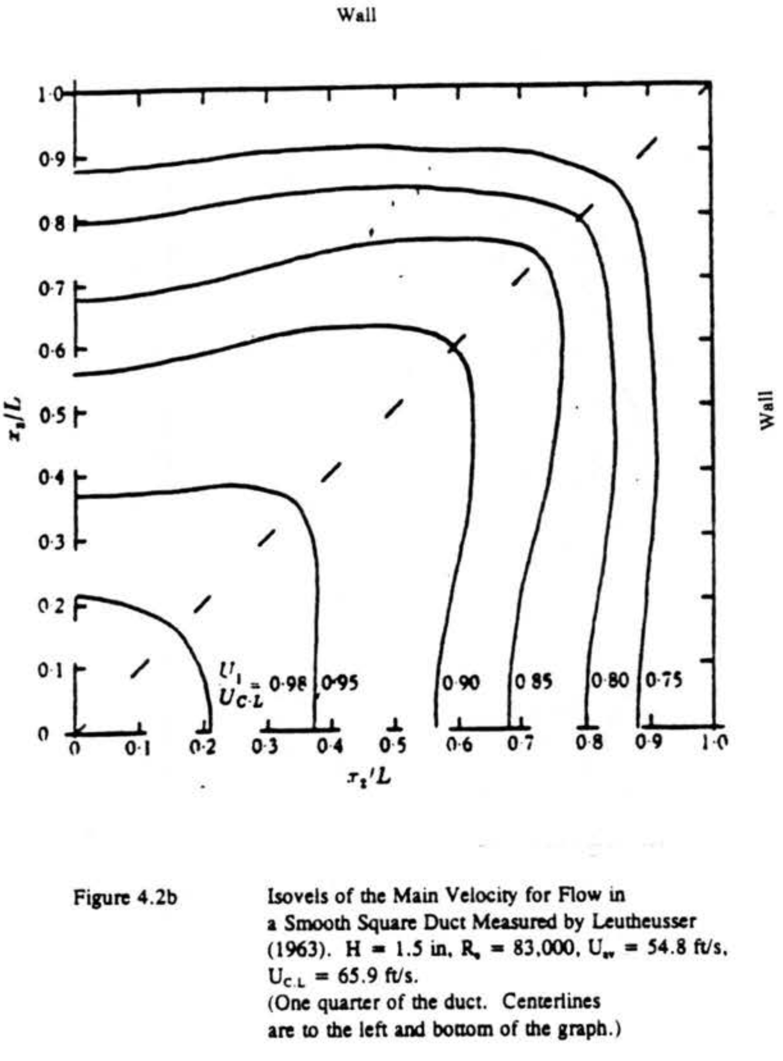

Figure 4.2b Isovels of the Main Velocity for Flow in a Smooth Square Duct Measured by Leutheusser (1963). H = 1.5 in, R_e = 83,000, U_{av} = 54.8 ft/s, $U_{C.L}$ = 65.9 ft/s.
(One quarter of the duct. Centerlines are to the left and bottom of the graph.)

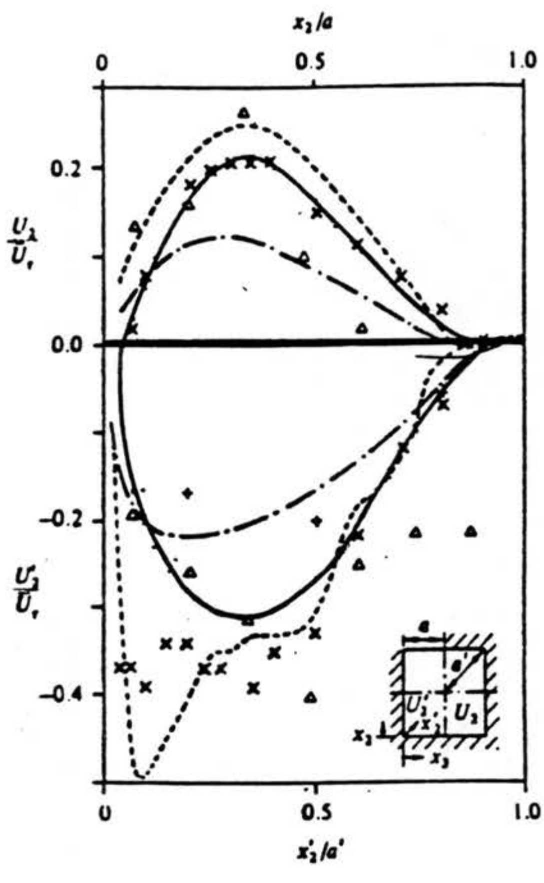

Figure 4.3 Secondary Velocities along Wall and Corner bisectors of a Smooth Square Duct.
Data: Δ Brundrett & Baines (1964);
+ Launder and Ying (1972);
x Gessner in (Gessner and Emery 1980).
Predictions: --- Naot and Rodi's (1982) model;
-.- Demuren and Rodi's (1982) model; - Present Model.

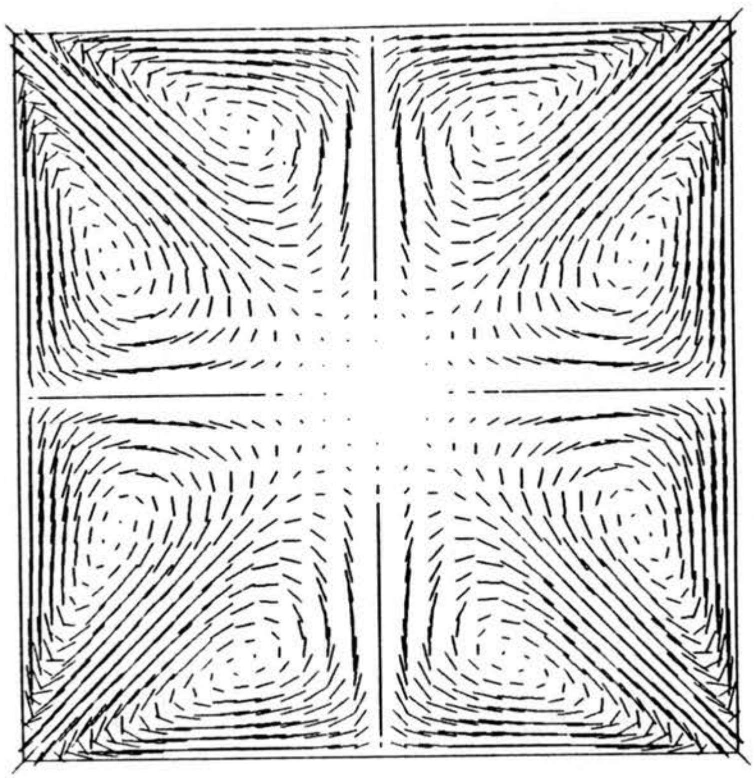

Figure 4.4a Predicted Secondary Flow in a Smooth Square Duct, R_e = 83,000 (Full cross section of the duct).

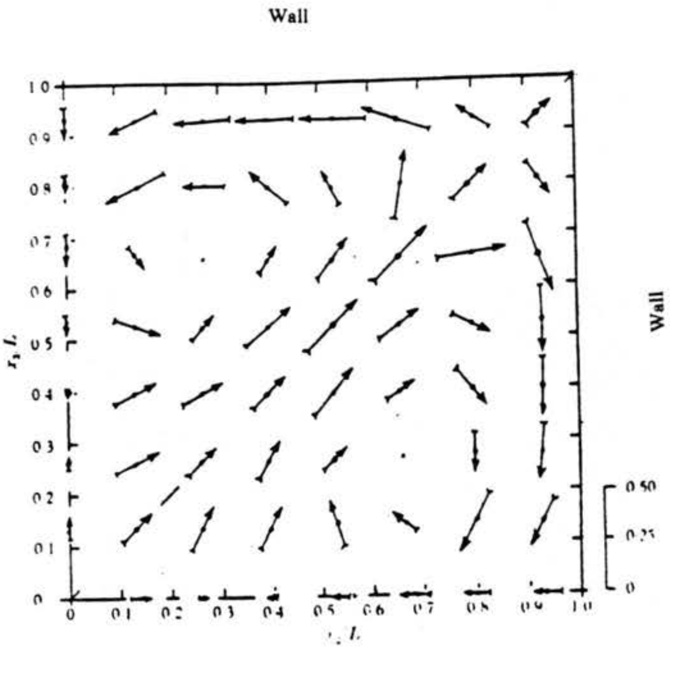

Figure 4.4b Measured Secondary Flow in a Smooth Square Duct, Brundrett & Baines 1964, R_e = 83,000, u_* = 2.55 ft/s. (One quarter of the duct. Centerlines are to the left and bottom of the graph.)

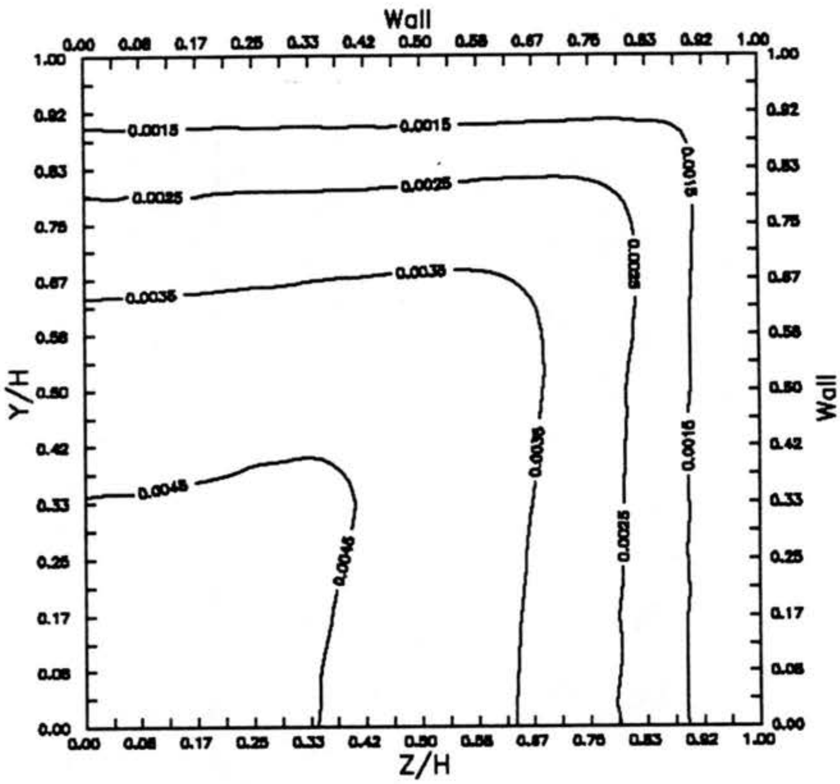

Figure 4.5 Predicted Contour Lines of the Turbulent Viscosity (Normalized by U_{av} H) in a Smooth Square Duct. H = 1.5 in, U_{av} = 54.8 ft/s, R_e = 83,000. (One quarter of the duct. Centerlines are to the left and bottom of the graph.)

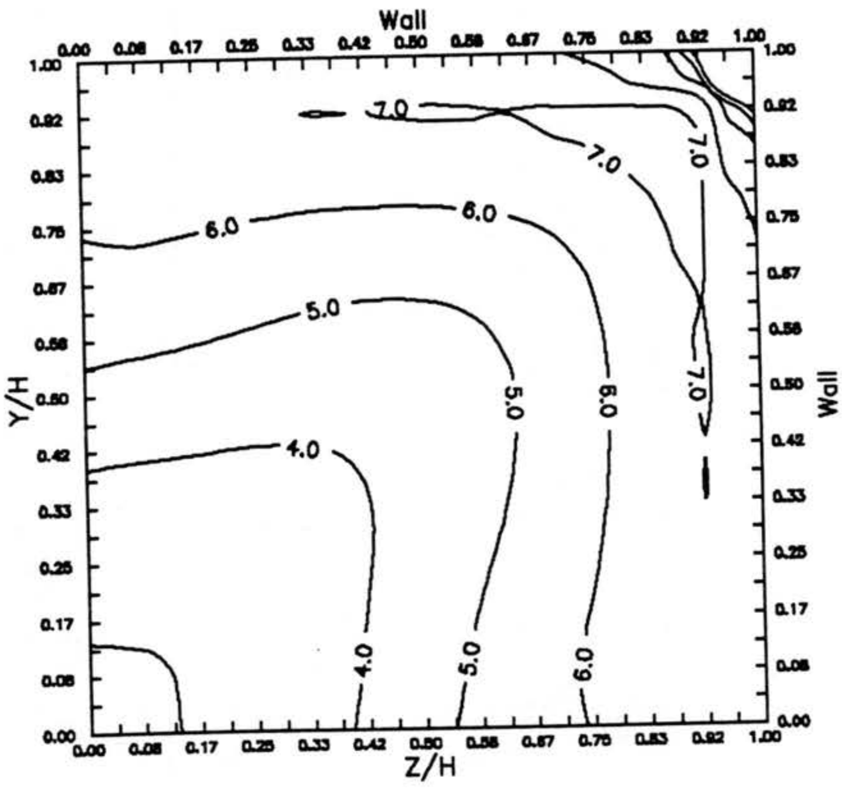

Figure 4.6a Predicted Distribution of the Turbulent Kinetic Energy (Normalized by $u_*^2/2$) in a Smooth Square Duct. H = 1.5 in, u_* = 2.55 ft/s, R_e = 83,000. (One quarter of the duct. Centerlines are to the left and bottom of the graph.)

Wall

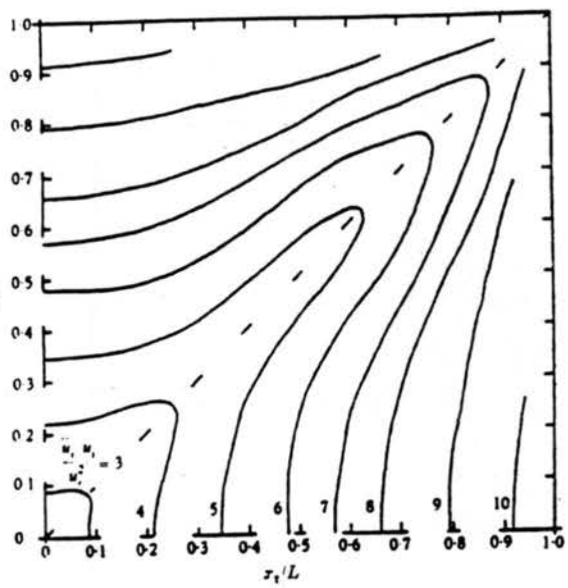

Wall

Figure 4.6b Measured Contour Lines of the Turbulent Kinetic Energy in a Smooth Square Duct, Brundrett & Baines 1964, $u_* = 2.55$ ft/s, $R_e = 83,000$.
(One quarter of the duct. Centerlines are to the left and bottom of the graph.)

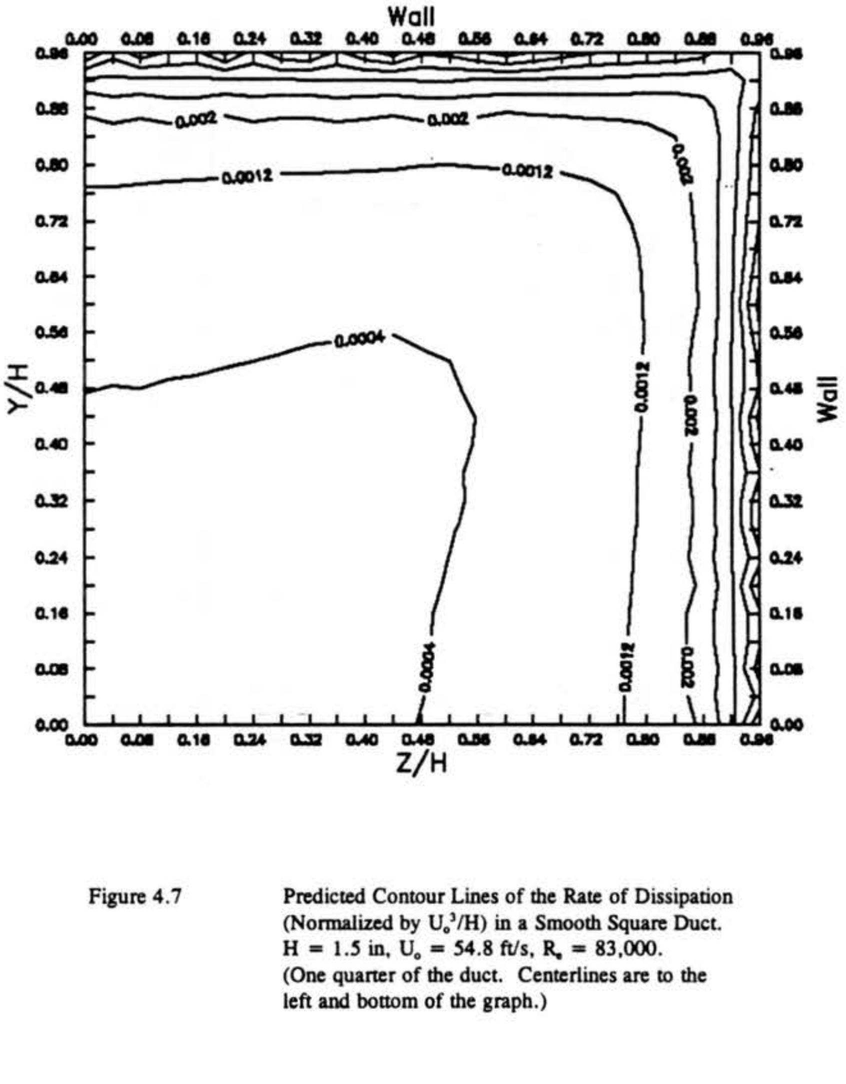

Figure 4.7 Predicted Contour Lines of the Rate of Dissipation (Normalized by U_o^3/H) in a Smooth Square Duct. $H = 1.5$ in, $U_o = 54.8$ ft/s, $R_e = 83,000$. (One quarter of the duct. Centerlines are to the left and bottom of the graph.)

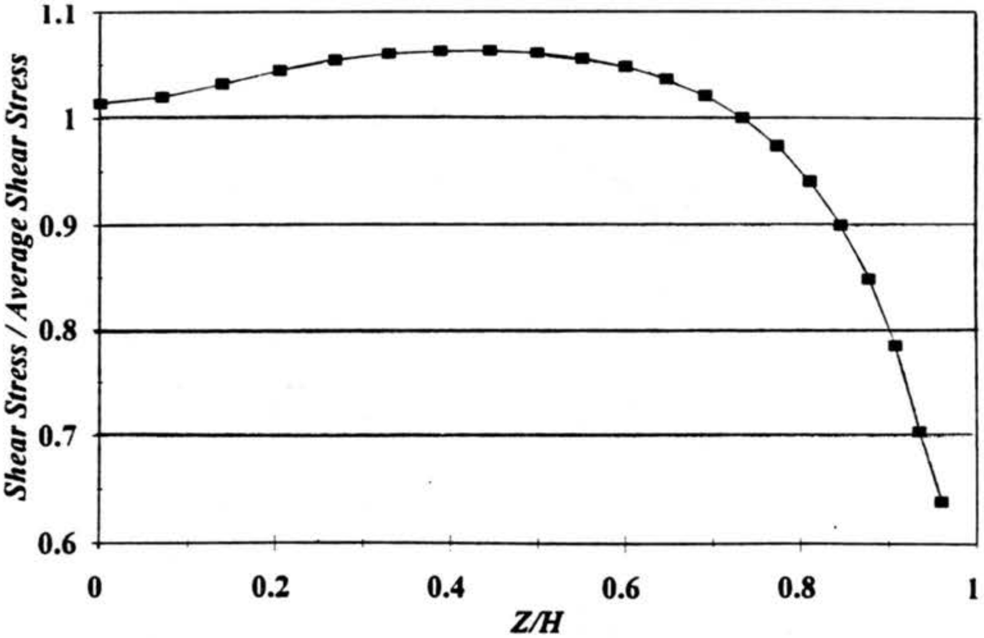

Figure 4.8a Predicted Wall Shear Stress Distribution in a Smooth Square Duct, R_e = 83,000. (Right half of the top wall. Centerline is to the left of the graph.)

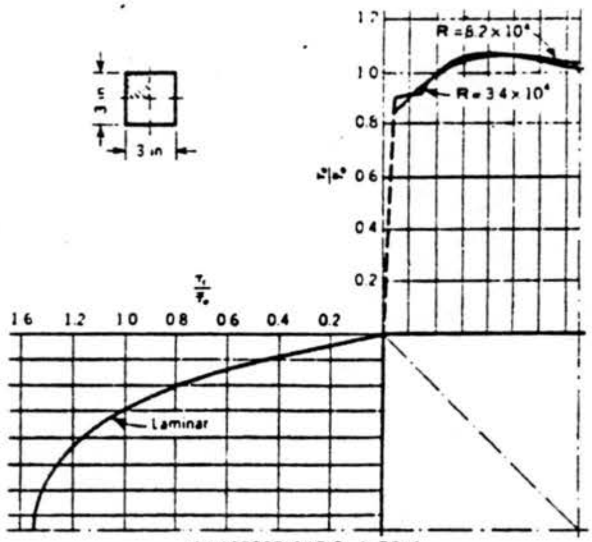

Figure 4.8b Measured Wall Shear Stress Distribution in a Smooth Square Duct, Leutheusser 1963, R_e = 83,000.
(One quarter of the duct. Centerlines are to the right and bottom of the graph.)

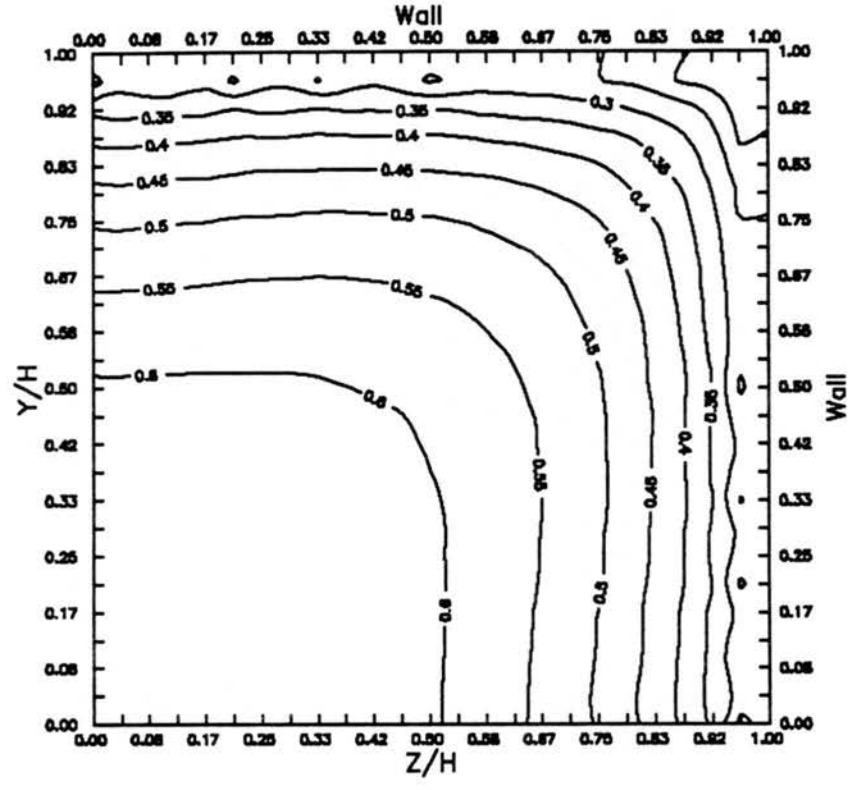

Figure 4.9 Predicted Main Velocity Contour Lines (Normalized by a velocity = 54.8 ft/s) in a Rough Square Duct. H = 1.5 in, K_s = 0.02 ft, R_e = 40,500. (One quarter of the duct. Centerlines are to the left and bottom of the graph.)

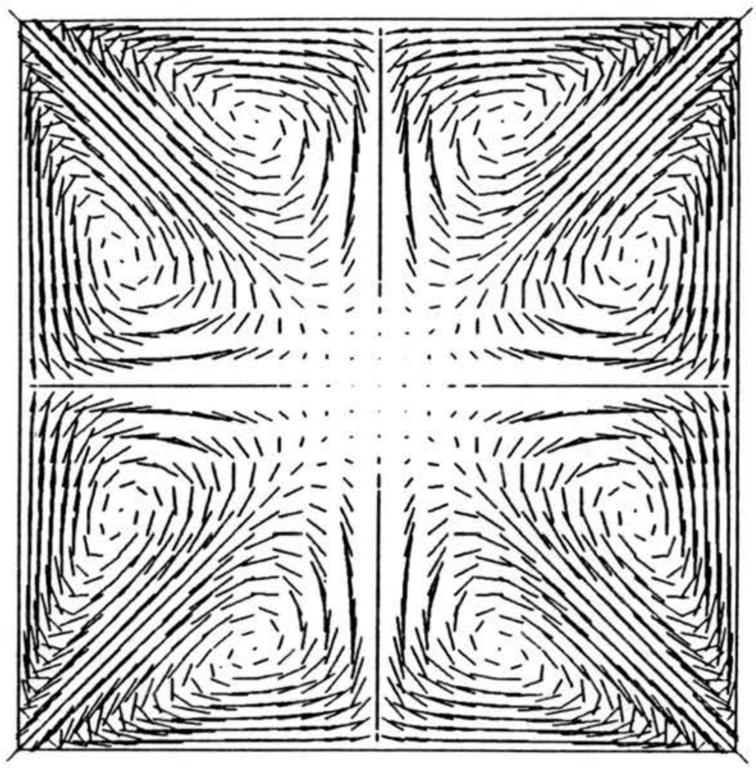

Figure 4.10 Predicted Secondary Flow in a Rough Square Duct. K_s = 0.02 ft, R_e = 40,500. (Full cross section of the duct. Same scale as in Figure 4.4a.)

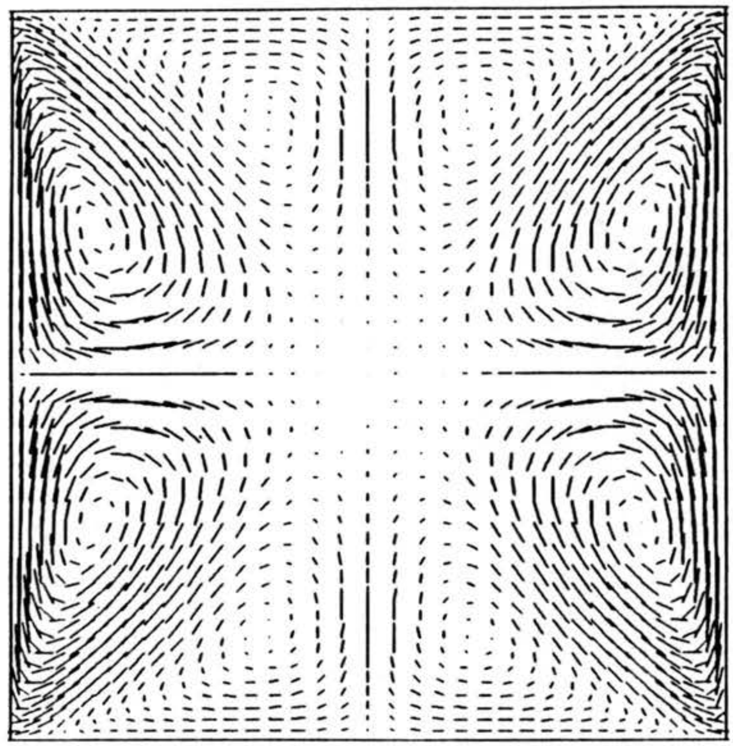

Figure 4.11 Predicted Secondary Flow in a Smooth Side Walls, Rough Top and Bottom Square Duct.
K_s = 0.02 ft, R_e = 53,000.
(Full cross section of the duct. Same scale as in Figures 4.4a and 4.10.)

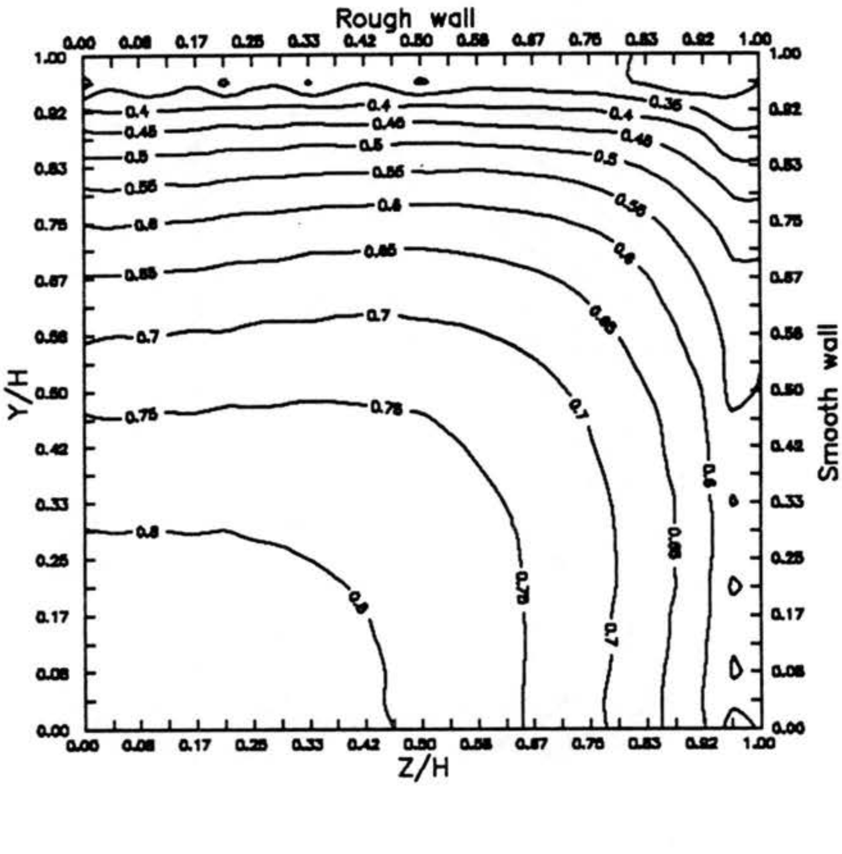

Figure 4.12 Predicted Main Velocity Contour Lines (Normalized by a velocity = 54.8 ft/s) in a Smooth Side Walls, Rough Top and Bottom Square Duct. H = 1.5 in, K_s =0.02 ft, R_e = 53,000. (One quarter of the duct. Centerlines are to the left and bottom of the graph.)

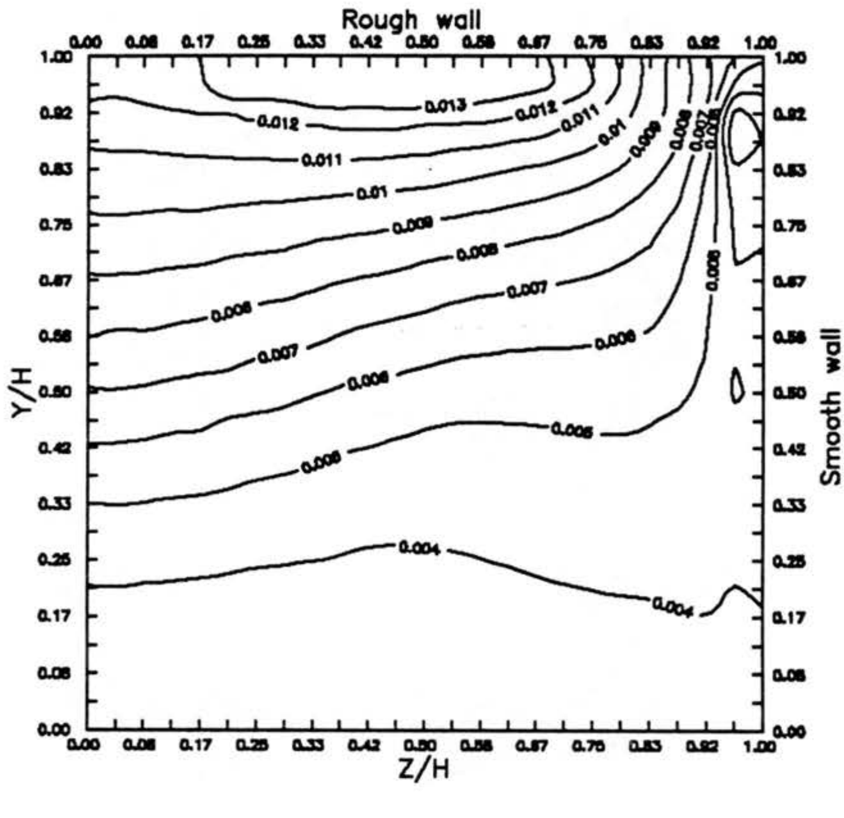

Figure 4.13 Predicted Turbulent Kinetic Energy Contour Lines (Normalized by U_o^2) in a Smooth Side Walls, Rough Top and Bottom Square Duct. $H = 1.5$ in, $K_s = 0.02$ ft, $U_o = 54.8$ ft/s, $R_e = 53{,}000$.
(One quarter of the duct. Centerlines are to the left and bottom of the graph.)

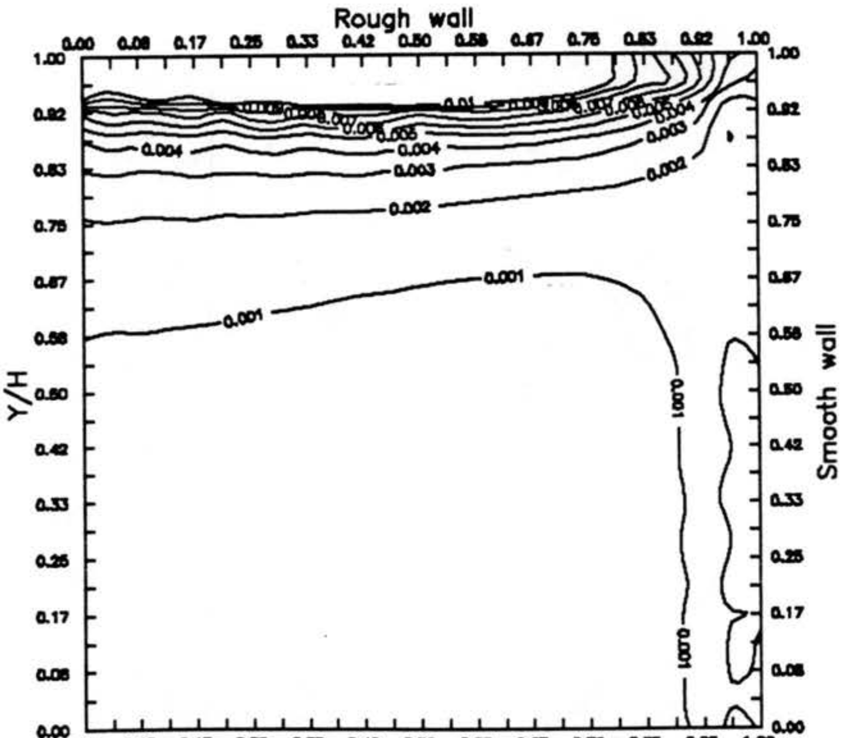

Figure 4.14 Predicted Rate of Dissipation Contour Lines (Normalized by U_o^3/H) in a Smooth Side Walls, Rough Top and Bottom Square Duct. H = 1.5 in, K_s = 0.02 ft, U_o = 54.8 ft/s, R_e = 53,000. (One quarter of the duct. Centerlines are to the left and bottom of the graph.)

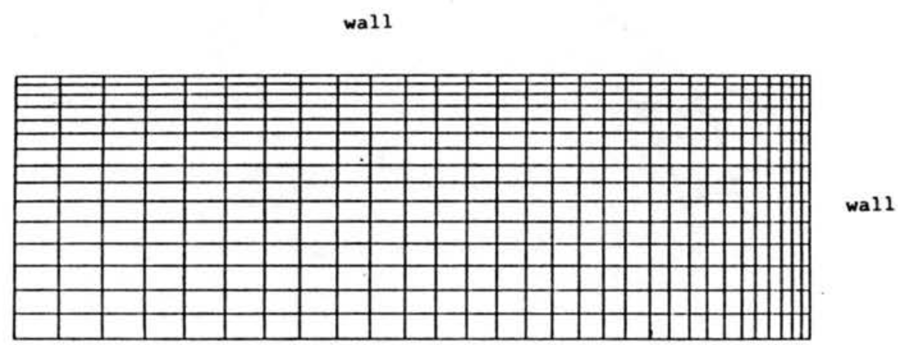

Figure 4.15 The Mesh for the Rectangular Duct (1:3). (One quarter of the duct. Centerlines are to the left and bottom of the graph.)

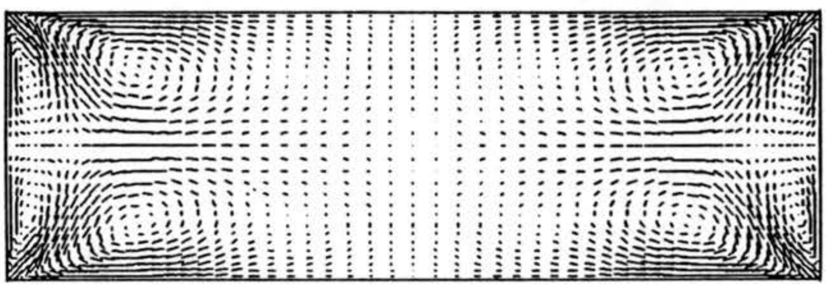

Figure 4.16a Predicted Secondary Flow in a Smooth Rectangular Duct (1:3). R_e = 92,190. (Full cross section of the duct.)

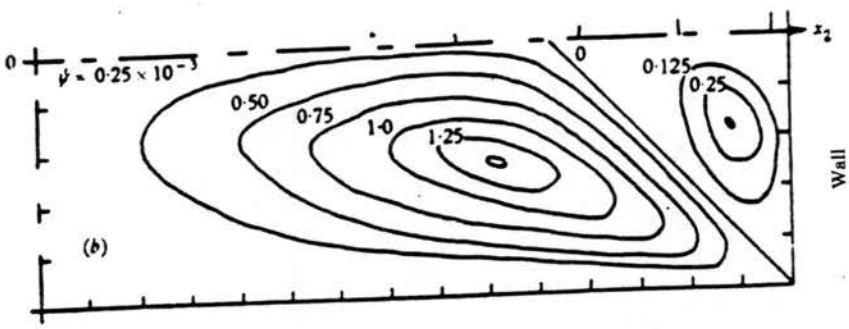

Figure 4.16b Stream Lines of Measured Secondary Flow in a Smooth Rectangular Duct (1:3), Hoagland 1960. R_e = 92,190. (One quarter of the duct. Centerlines are to the left and top of the graph.)

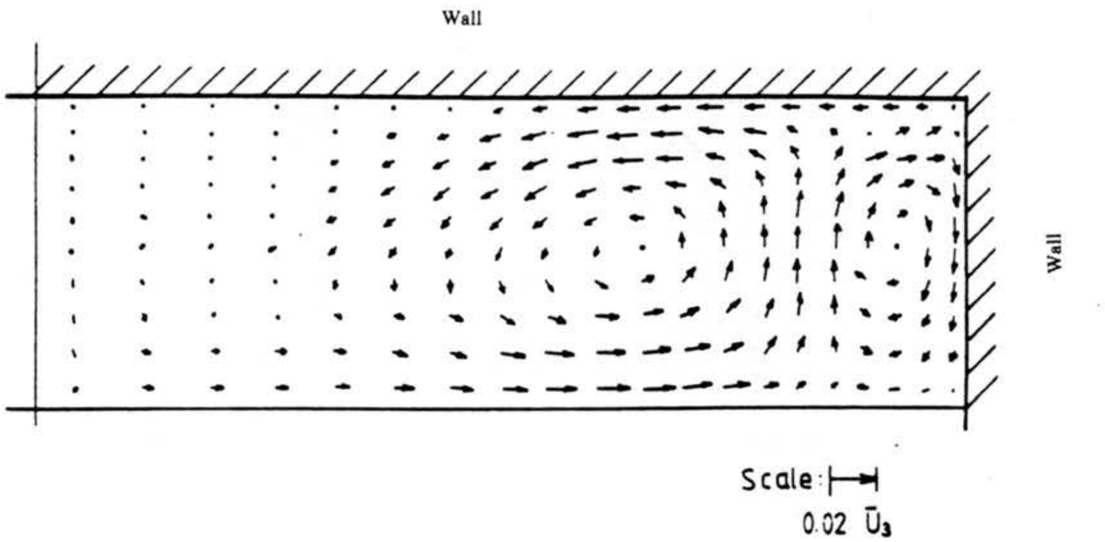

Figure 4.16c Predicted Secondary Flow in a Smooth Rectangular Duct (1:3), Gosman & Rapley 1978. (One quarter of the duct. Centerlines are to the left and bottom of the graph.)

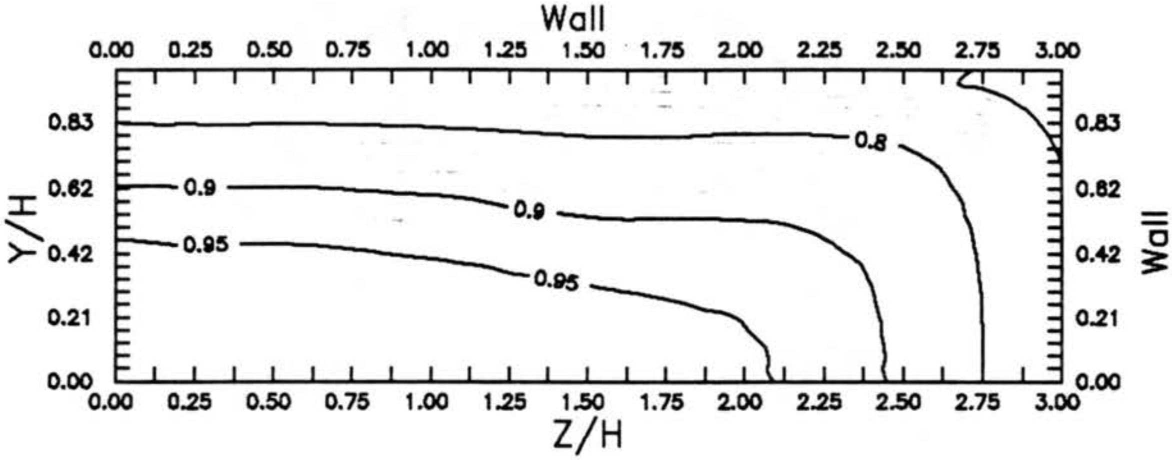

Figure 4.17a Predicted Main Velocity Contour Lines (Normalized by a velocity = 48.98 ft/s) in a Smooth Rectangular Duct (1:3). H = 1.5 in, R_e = 92,190. (One quarter of the duct. Centerlines are to the left and bottom of the graph.)

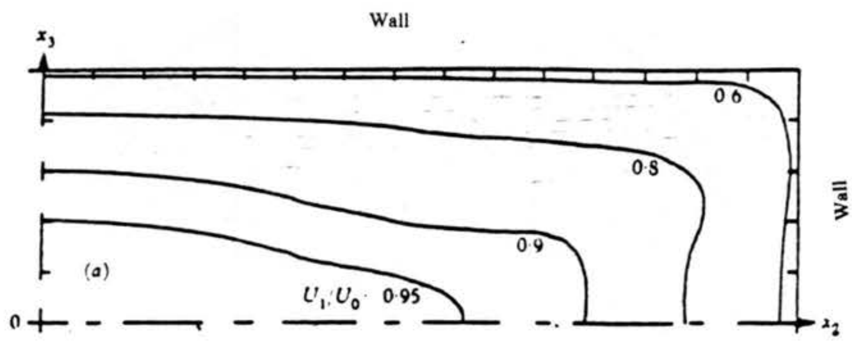

Figure 4.17b Measured Main velocity Contour Lines in a Smooth Rectangular Duct (1:3), Leutheusser 1963. U_o = 48.98 ft/s, R_e = 92,190. (One quarter of the duct. Centerlines are to the left and bottom of the graph.)

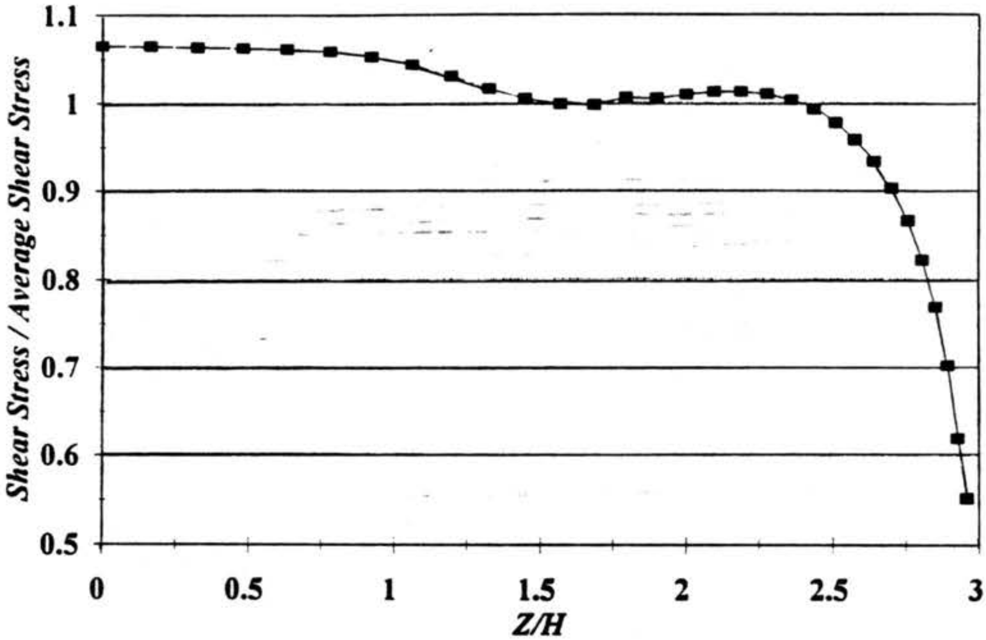

Figure 4.18a Predicted Top Wall Shear Stress Distribution in a Smooth Rectangular Duct (1:3).
$H = 1.5$ in, $R_e = 92{,}190$.
(Right half of top wall).

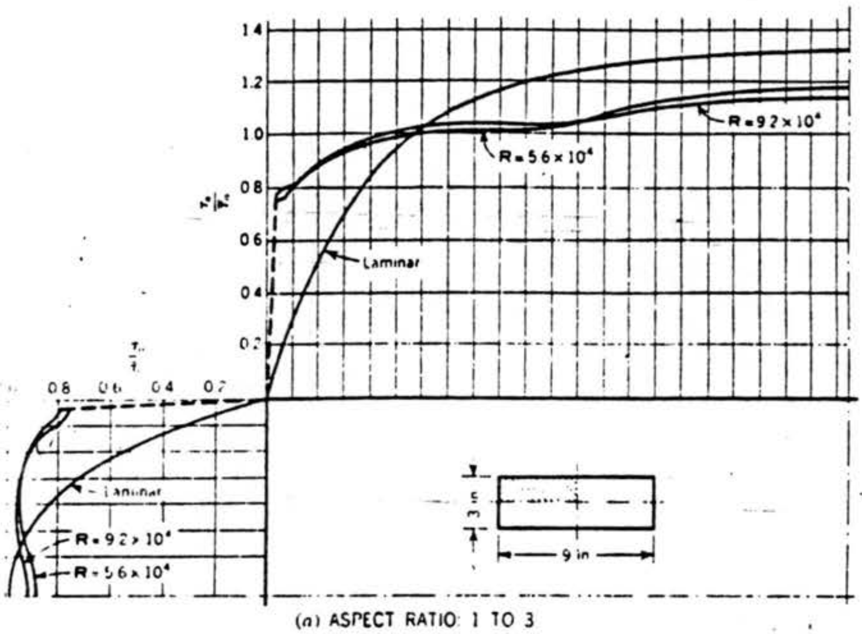

Figure 4.18b Measured Wall Shear Stress Distribution in a Smooth Rectangular Duct (1:3), Leutheusser 1963.

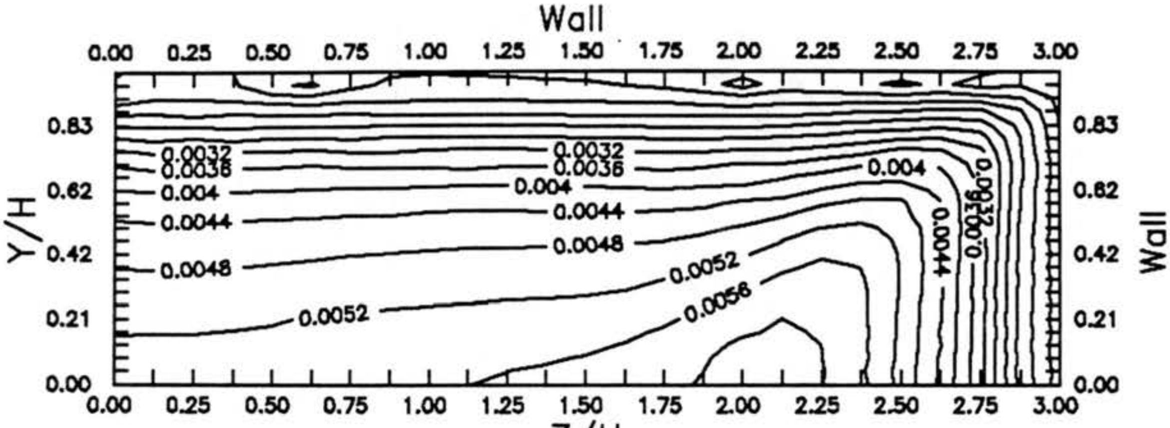

Figure 4.19 Predicted Contour Lines of the Turbulent Viscosity (Normalized by U_o H) in a Smooth Rectangular Duct (1:3). H = 1.5 in, U_o = 40.82 ft/s, R_e = 92,190. (One quarter of the duct. Centerlines are to the left and bottom of the graph.)

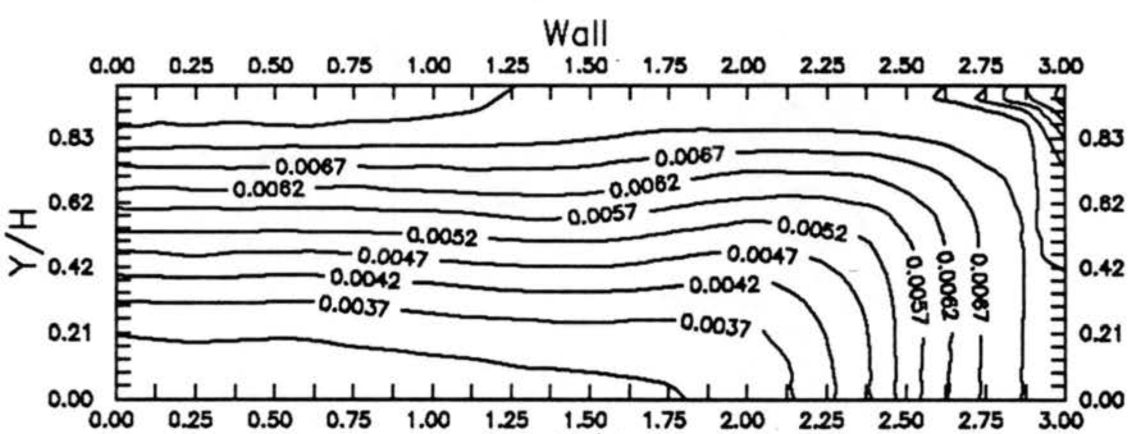

Figure 4.20 Predicted Contour Lines of the Turbulent Kinetic Energy (Normalized by U_o^2) in a Smooth Rectangular Duct (1:3). $H = 1.5$ in, $U_o = 40.82$ ft/s, $R_e = 92,190$. (One quarter of the duct. Centerlines are to the left and bottom of the graph.)

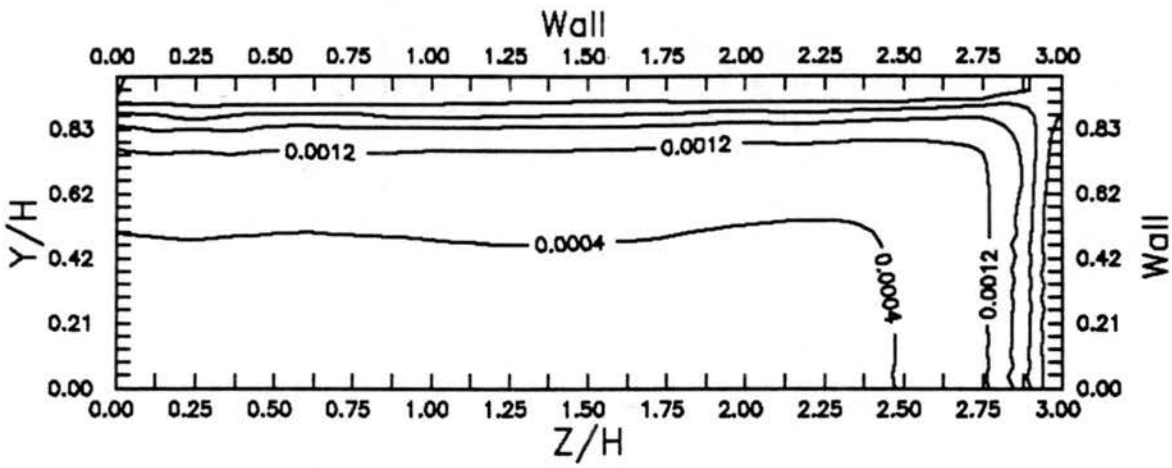

Figure 4.21 Predicted Contour Lines of the Rate of Dissipation (Normalized by U_o^3/H) in a smooth rectangular duct (1:3). $H = 1.5$ in, $U_o = 40.82$ ft/s, $R_e = 92{,}190$. (One quarter of the duct. Centerlines are to the left and bottom of the graph.)

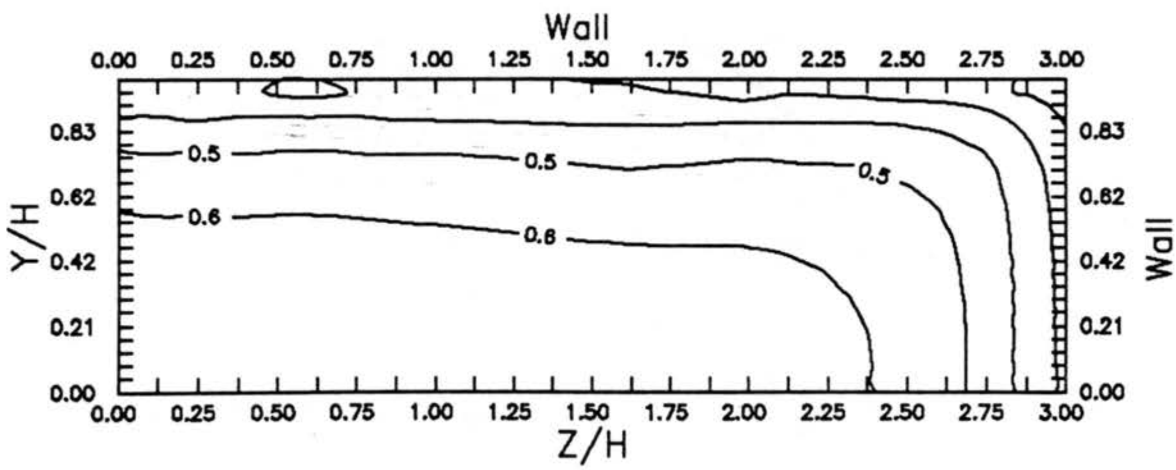

Figure 4.22 Predicted Main Velocity Contour Lines (Normalized by a velocity = 40.82 ft/s) in a Rough Rectangular Duct (1:3). H = 1.5 in, R_e = 49,000. (One quarter of the duct. Centerlines are to the left and bottom of the graph.)

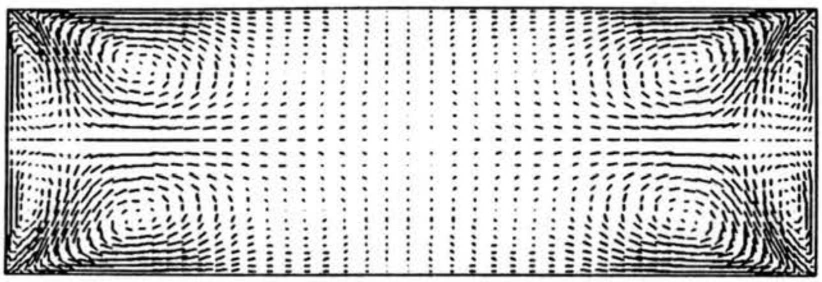

Figure 4.23 Predicted Secondary Flow in a Rough Rectangular Duct (1:3). (Full cross section of the duct.)

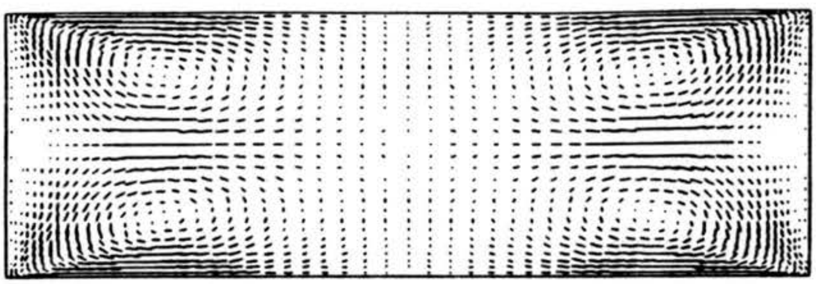

Figure 4.24 Predicted Secondary Flow in Rough Side Walls, Smooth Top and Bottom Walls Rectangular Duct (1:3).
(Full cross section of the duct.)

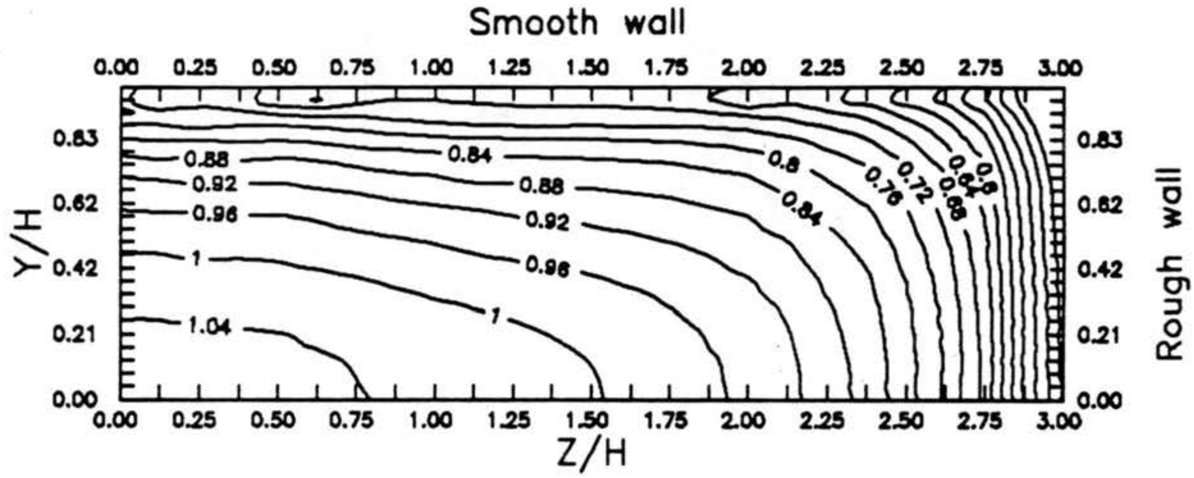

Figure 4.25 Predicted Main Velocity (Normalized by a velocity = 40.82 ft/s) in Rough Side Walls, Smooth Top and Bottom Walls Rectangular Duct (1:3). H = 1.5 in, R_e = 78,000. (One quarter of the duct. Centerlines are to the left and bottom of the graph.)

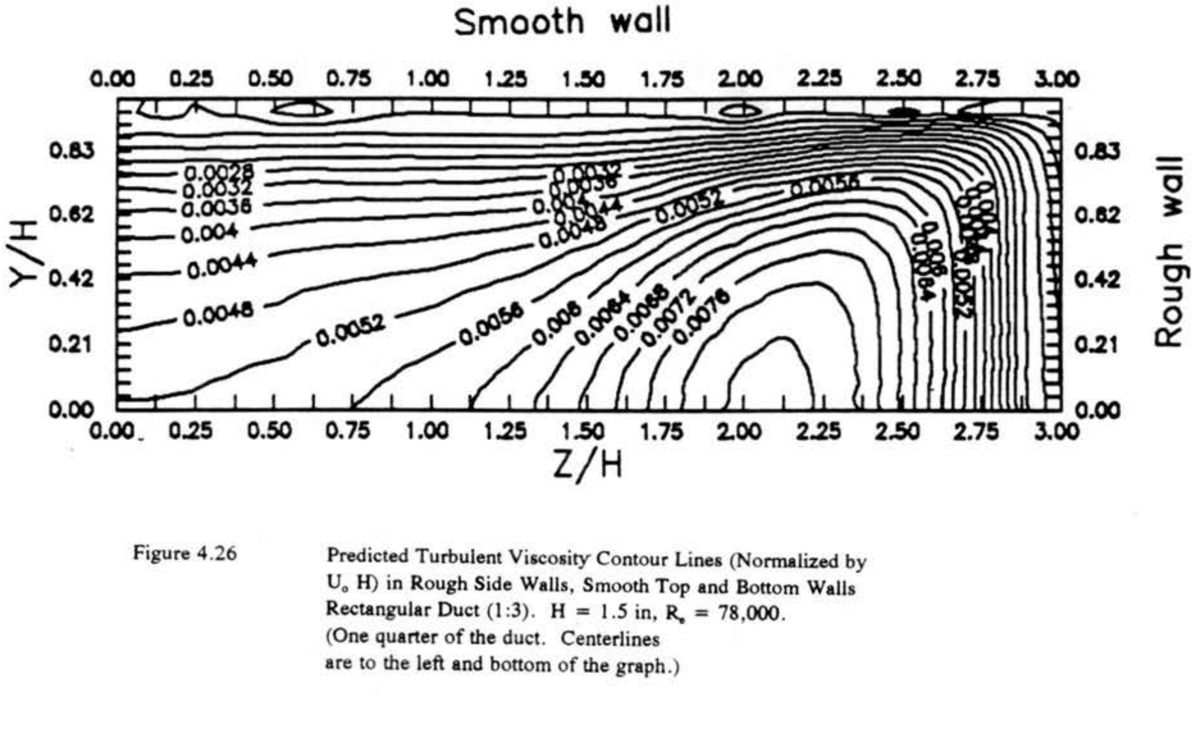

Figure 4.26 Predicted Turbulent Viscosity Contour Lines (Normalized by U_o H) in Rough Side Walls, Smooth Top and Bottom Walls Rectangular Duct (1:3). H = 1.5 in, R_e = 78,000. (One quarter of the duct. Centerlines are to the left and bottom of the graph.)

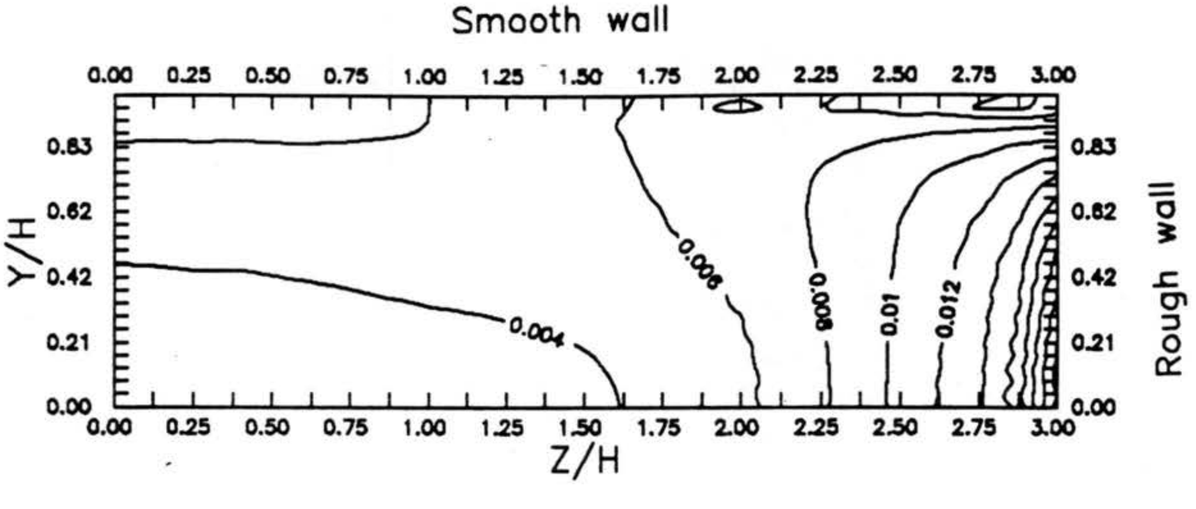

Figure 4.27 Predicted Turbulent Kinetic Energy Contour Lines (Normalized by U_o^2) in Rough Side Walls, Smooth Top and Bottom Walls Rectangular Duct (1:3). H = 1.5 in, U_o = 40.82 ft/s, R_e = 78,000. (One quarter of the duct. Centerlines are to the left and bottom of the graph.)

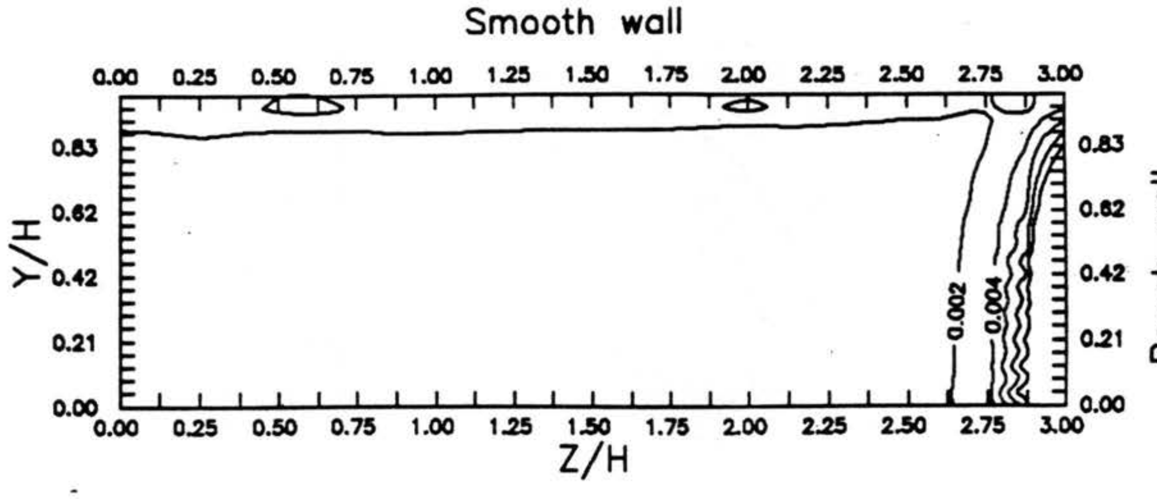

Figure 4.28 Predicted Rate of Dissipation Contour Lines (Normalized by U_o^3/H) in Rough Side Walls, Smooth Top and Bottom Walls Rectangular Duct (1:3). H = 1.5 in, U_o = 40.82 ft/s, R_e = 78,000. (One quarter of the duct. Centerlines are to the left and bottom of the graph.)

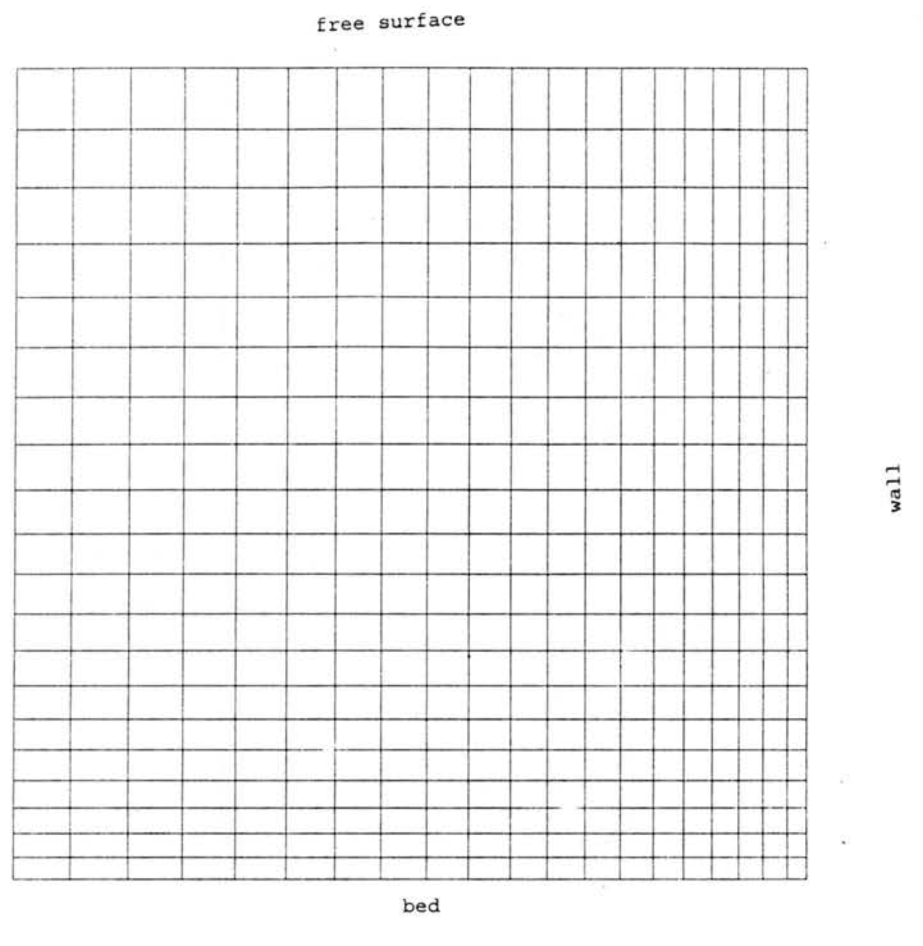

Figure 4.29 **The Mesh for the Smooth Open Channel (1:2).**
(Right side of the channel.
Centerline is to the left.)

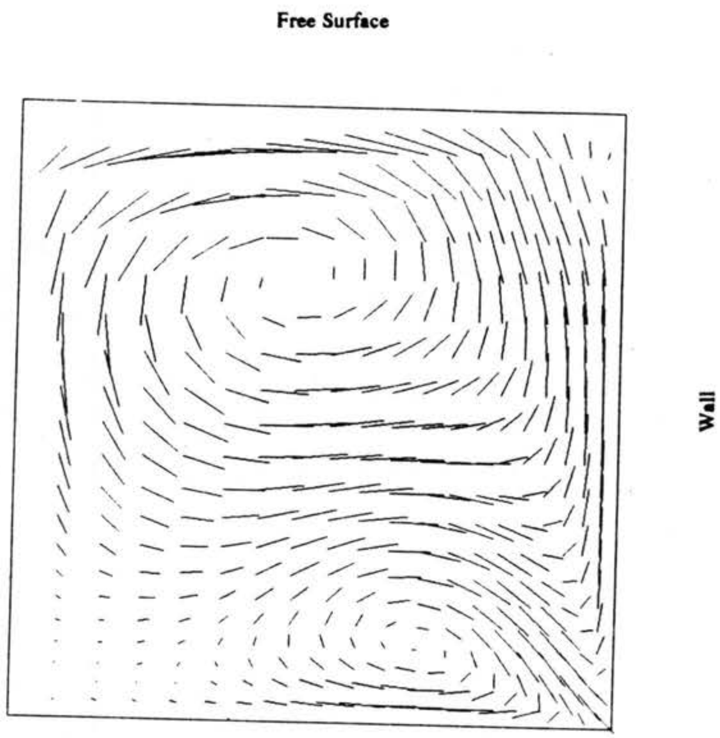

Figure 4.30a

Predicted Secondary Flow in Smooth Open Channel (1:2). H = 0.076 m, R_e = 39,000. (Right side of the channel. Centerline is to the left.)

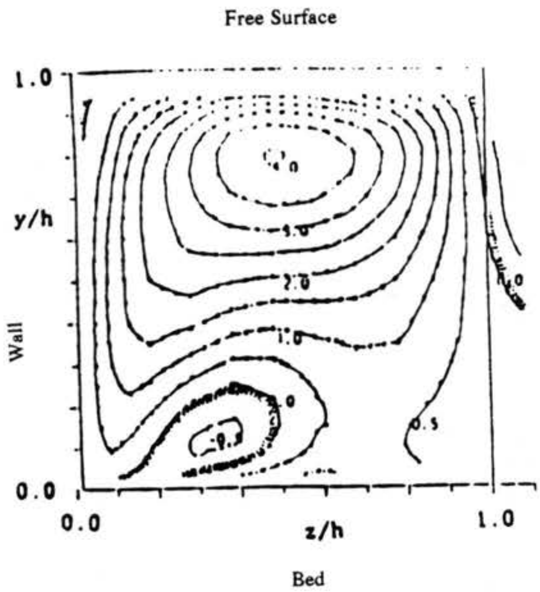

Figure 4.30b Measured Secondary Flow Stream Lines in Smooth Open Channel (1:2), Nezu et al. (1989). (Left side of the channel. Centerline is to the Right.)

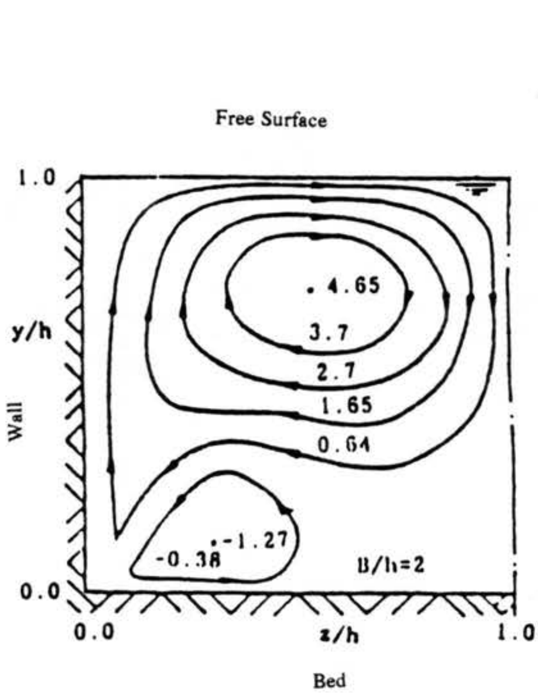

Figure 4.30c Predicted Secondary Flow Stream Lines in Smooth Open Channel (1:2), Naot & Rodi (1982). (Left side of the channel. Centerline is to the Right.)

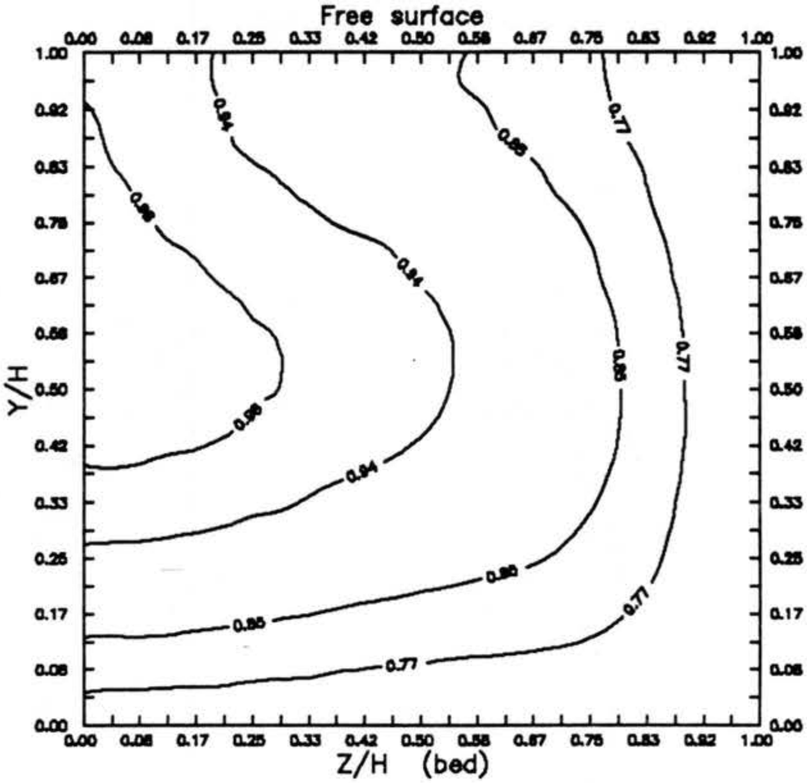

Figure 4.31a Predicted Main Velocity Contour Lines (Normalized by U_{max}) in Smooth Open Channel (1:2). $H = 0.076$ m, $R_e = 39{,}000$, $U_{max} = 0.421$ m/s.
(Right side of the channel.
Centerline is to the left.)

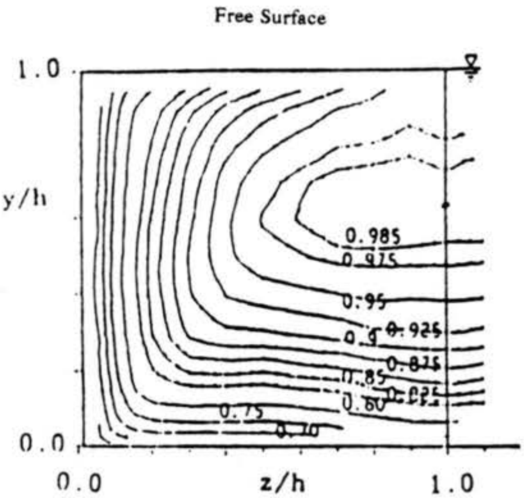

Figure 4.31b Measured (Laser Doppler Anemometer) Main Velocity Contour Lines in Smooth Open Channel (1:2), Nezu et al. (1989). (left side of the channel. Centerline is to the right.)

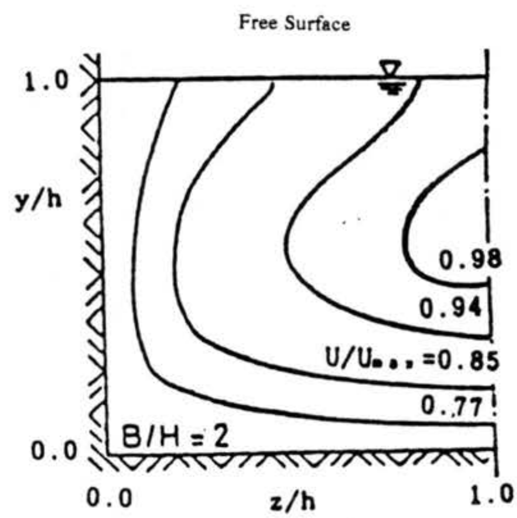

Figure 4.31c Predicted Main Velocity Contour Lines in Smooth Open Channel (1:2), Naot & Rodi (1982). (left side of the channel. Centerline is to the right.)

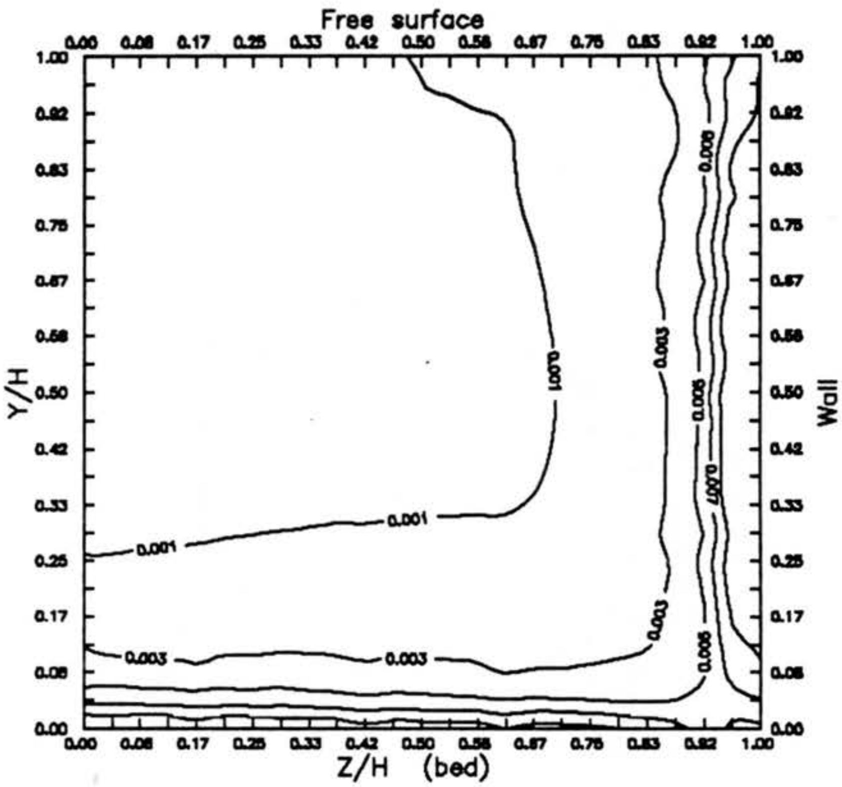

Figure 4.32 Predicted Rate of Dissipation Contour Lines (Normalized by U_o^3/H)in Smooth Open Channel (1:2). $H = 0.076$ m, $U_o = 0.338$ m/s, $R_e = 39,000$. (Right side of the channel. Centerline is to the left.)

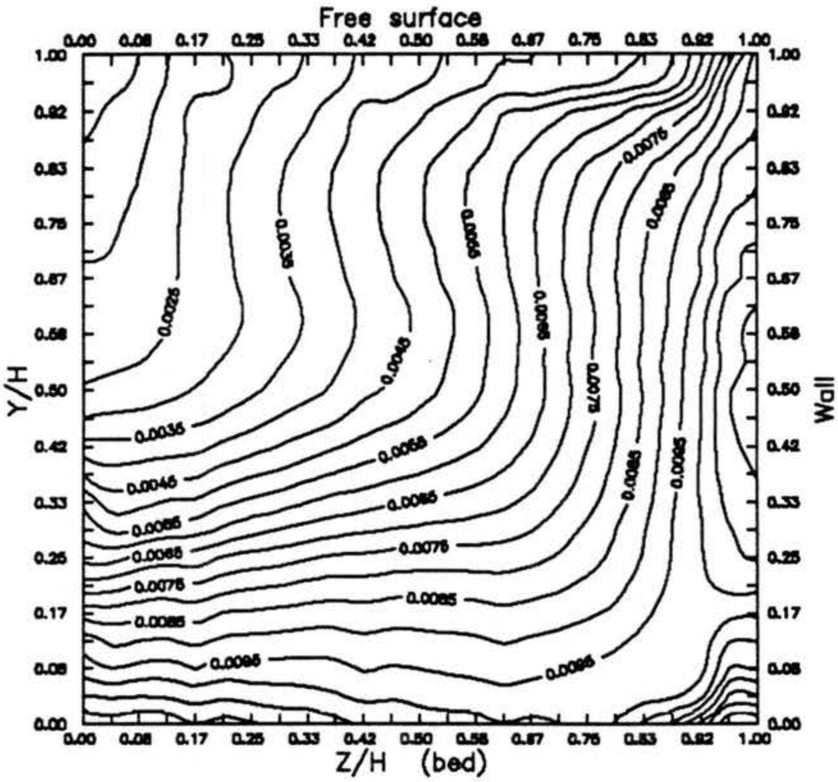

Figure 4.33 Predicted Turbulent Kinetic Energy Contour Lines (Normalized by U_o^2) in Smooth Open Channel (1:2). H = 0.076 m, U_o = 0.338 m/s, R_e = 39,000. (Right side of the channel. Centerline is to the left.)

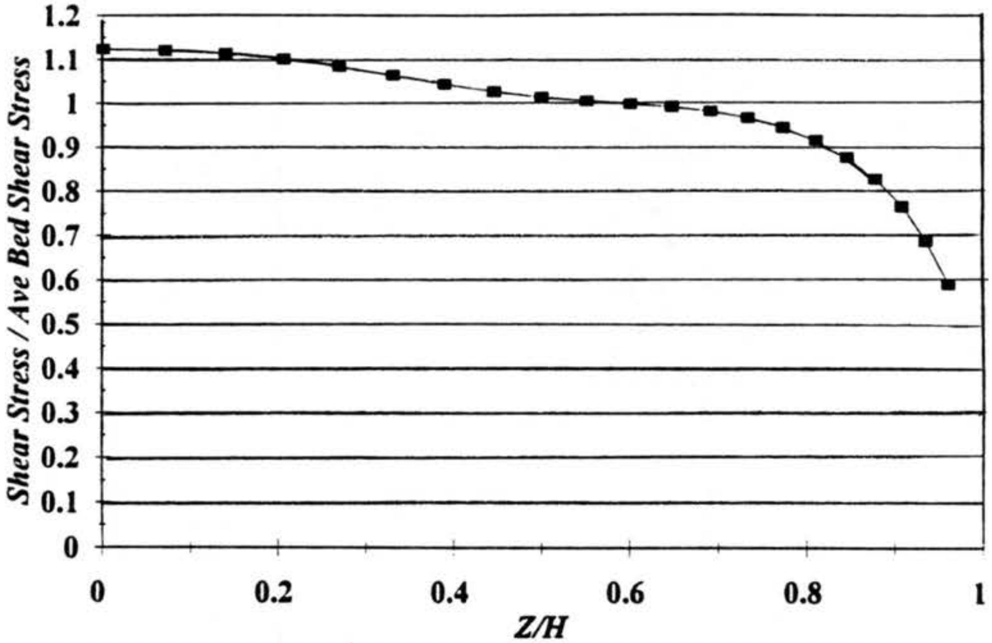

Figure 4.34a Predicted Bed Shear Stress in Smooth Open Channel (1:2). (Right half of the bed.)

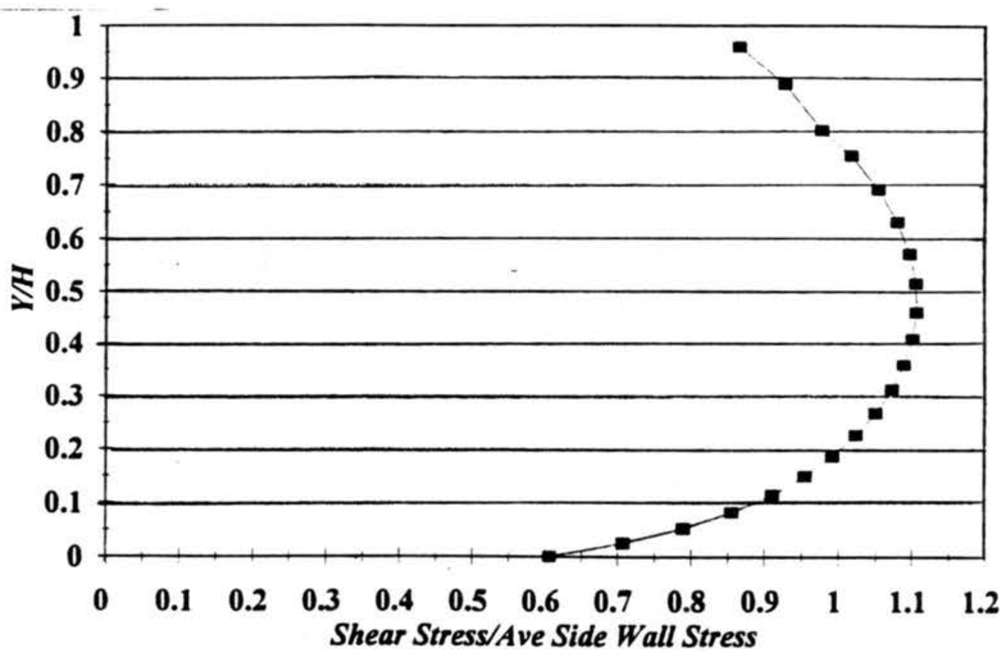

Figure 4.34b Predicted Side Wall Shear Stress in Smooth Open Channel (1:2).

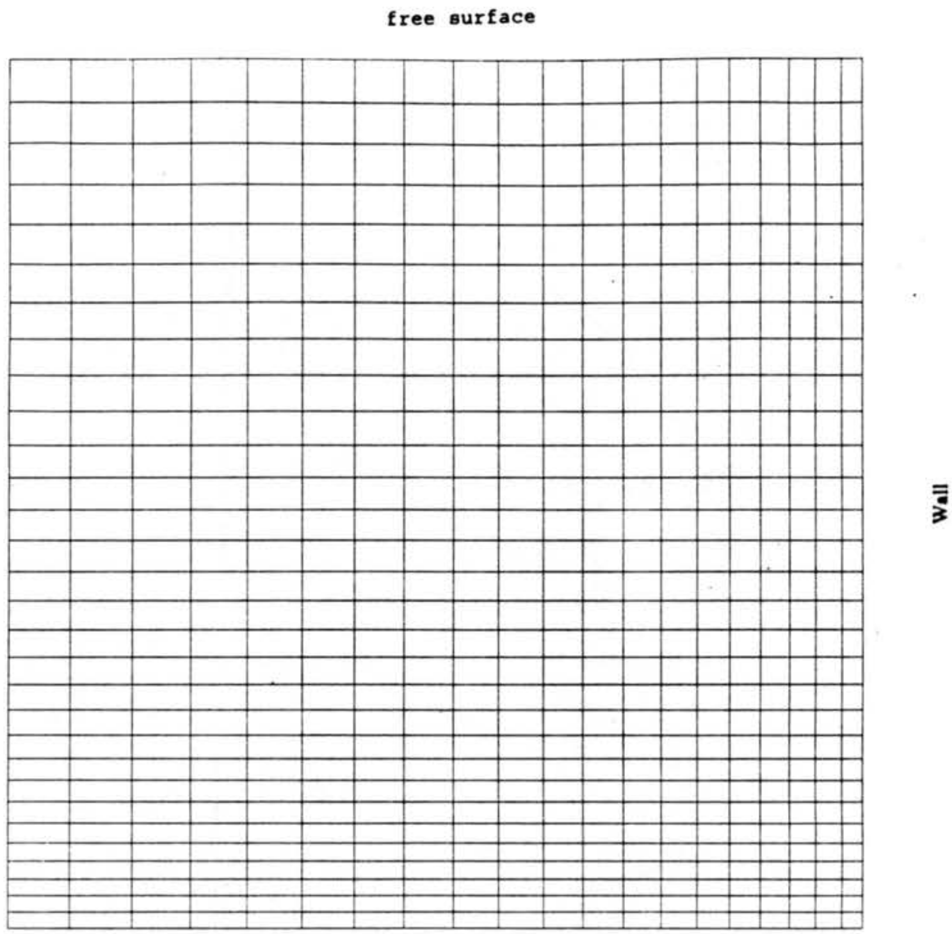

Figure 4.35 The Mesh for the Rough Open Channel (1:2).

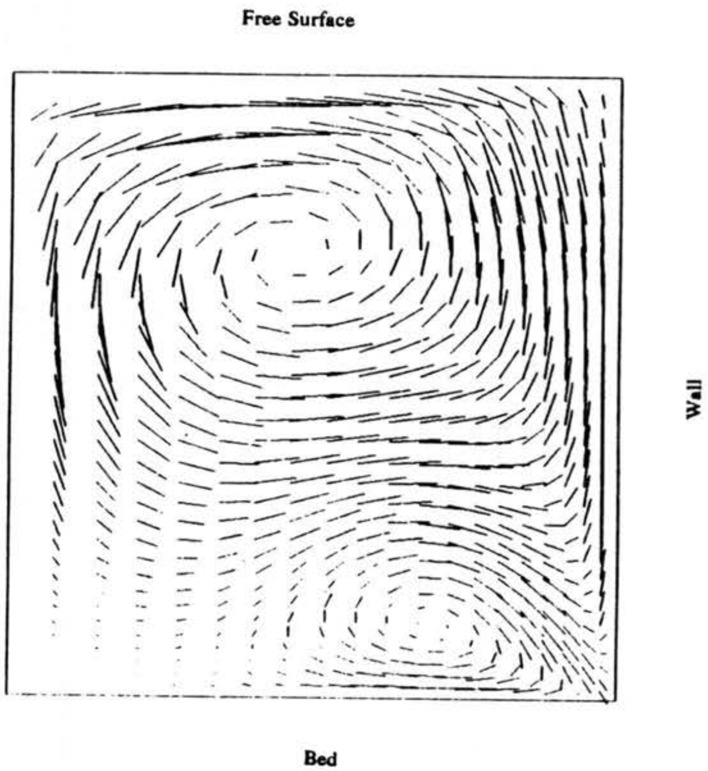

Figure 4.36 Predicted Secondary Flow for the Rough Open Channel (1:2). (Right side of the channel. Centerline is to the left.)

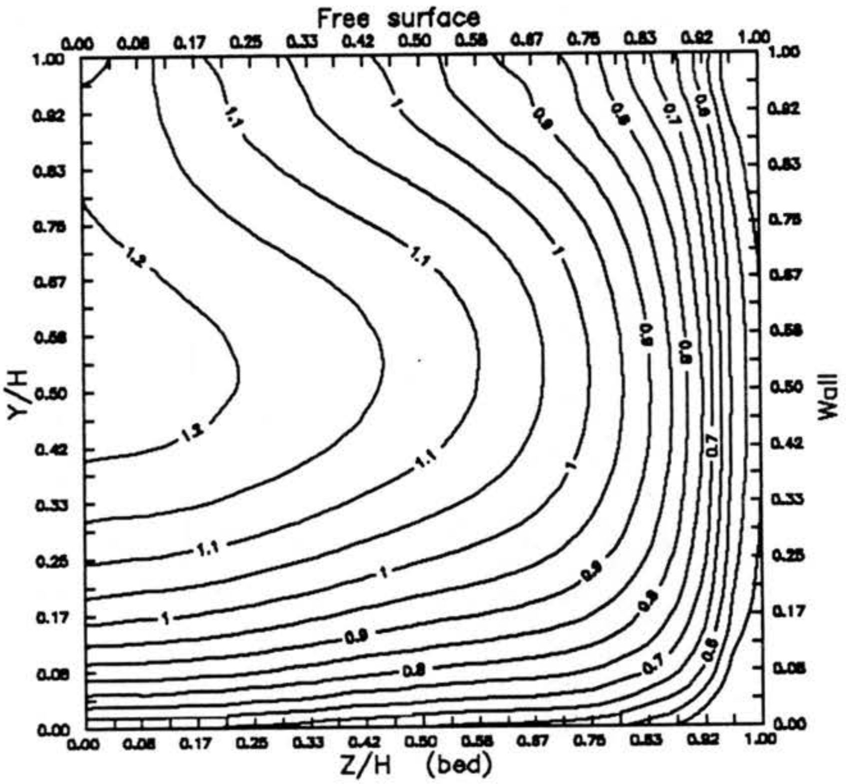

Figure 4.37 Predicted Main Velocity Contour Lines (Normalized by a velocity = 0.298 m/s) for the Rough Open Channel (1:2). H = 0.158 m, R_e = 87,300. (Right side of the channel. Centerline is to the left.)

Free Surface

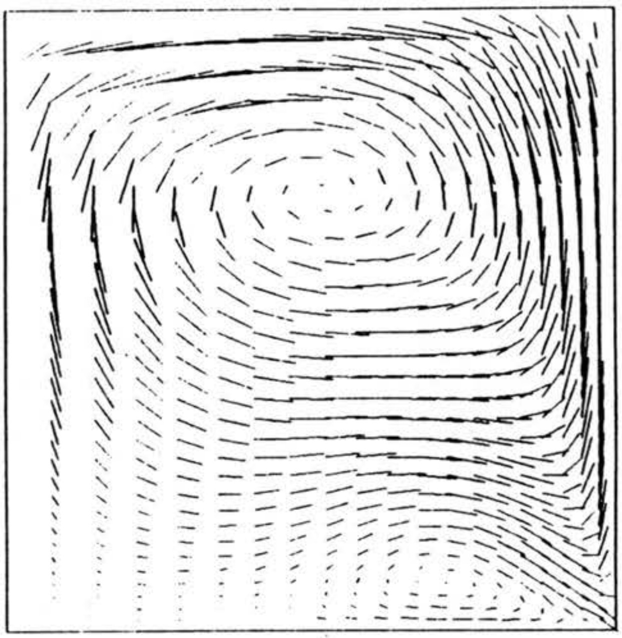

Wall

Bed

Figure 4.38 Predicted Secondary Flow for the Smooth Side Walls and Rough Bed Open Channel (1:2). R_e = 104,760. (Right side of the channel. Centerline is to the left.)

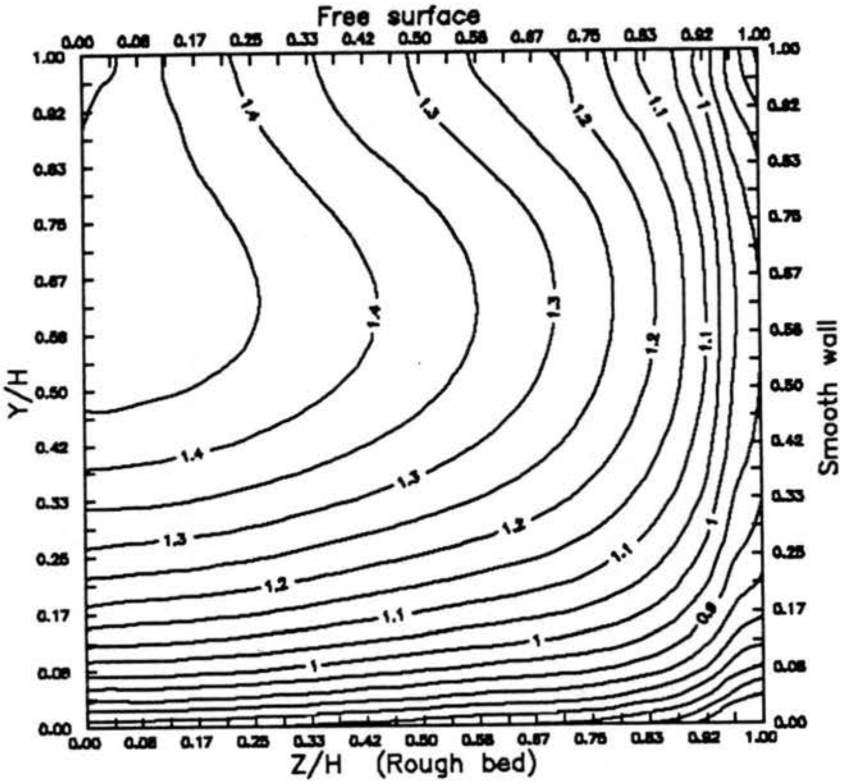

Figure 4.39 Predicted Main Velocity (Normalized by a velocity = 0.298 m/s) for the Smooth Side Walls and Rough bed open channel (1:2). H = 0.158 m, R_e = 104,760. (Right side of the channel. Centerline is to the left.)

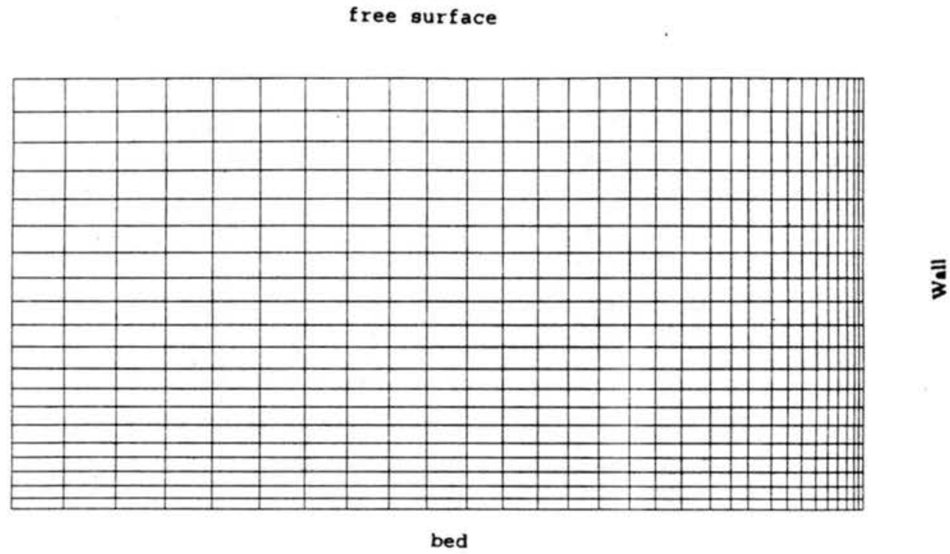

Figure 4.40 The Mesh for the Rectangular Open Channel (1:4).
(Right side of the channel. Centerline is to the left.)

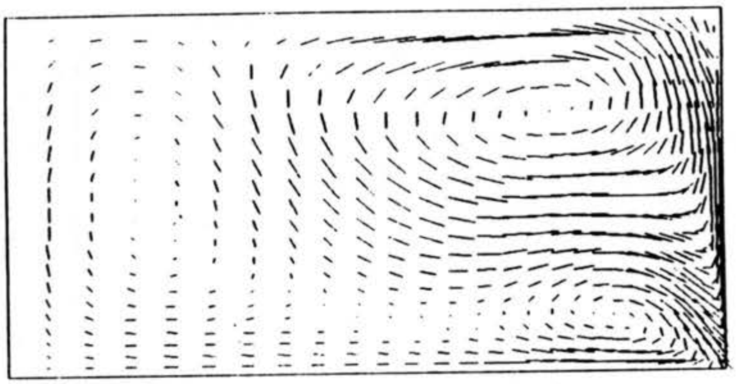

Figure 4.41a Predicted Secondary Flow for the Smooth Rectangular Open Channel (1:3.94). (Right side of the channel. Centerline is to the left.)

Free Surface

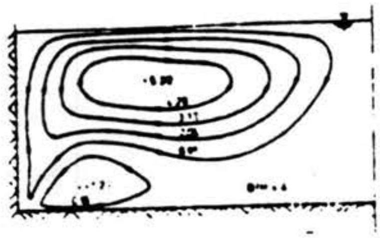

Figure 4.41b

Predicted Secondary Flow for the Smooth Rectangular Open Channel (1:4), Naot and Rodi (1982). (left side of the channel. Centerline is to the right.)

Free Surface

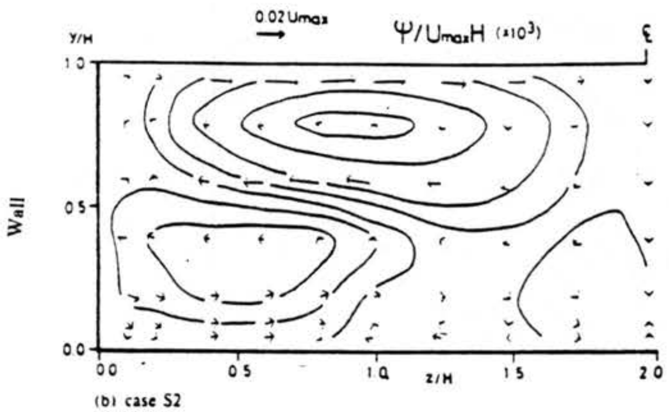

Figure 4.41c Measured Secondary Flow for the Smooth Rectangular Open Channel (1:3.94), Tominaga et al. (1989). (left side of the channel. Centerline is to the right.)

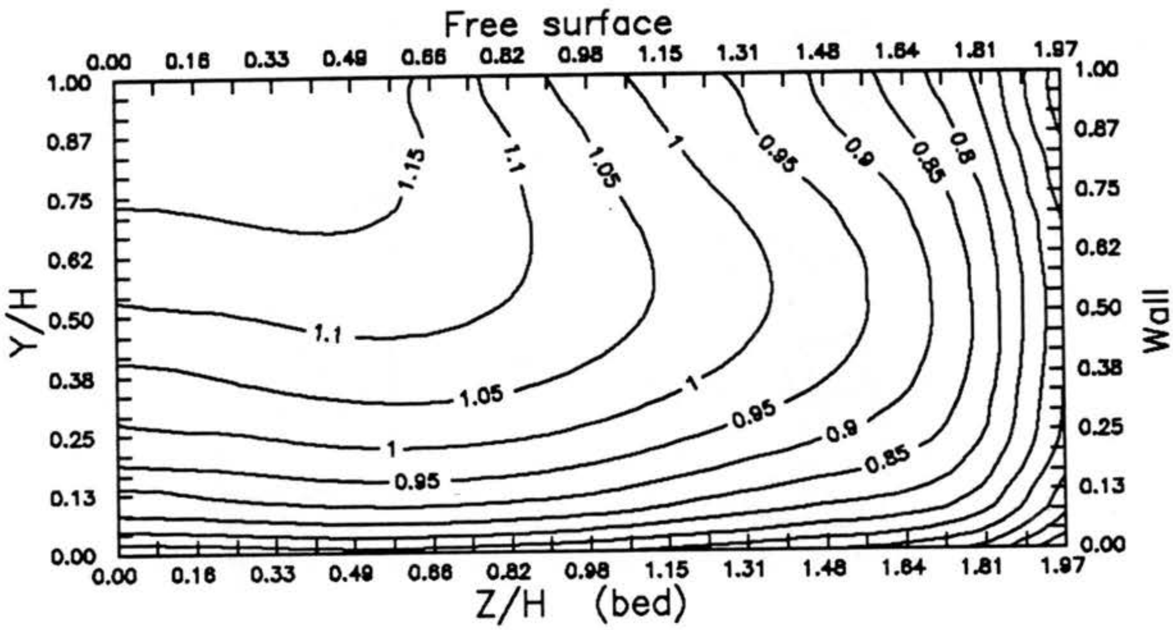

Figure 4.42 Predicted Main Velocity Contour Lines (Normalized by a velocity = 0.187 m/s) for the Smooth Rectangular Open Channel (1:3.94). H = 0.102 m, R_e = 50,700. (Right side of the channel. Centerline is to the left.)

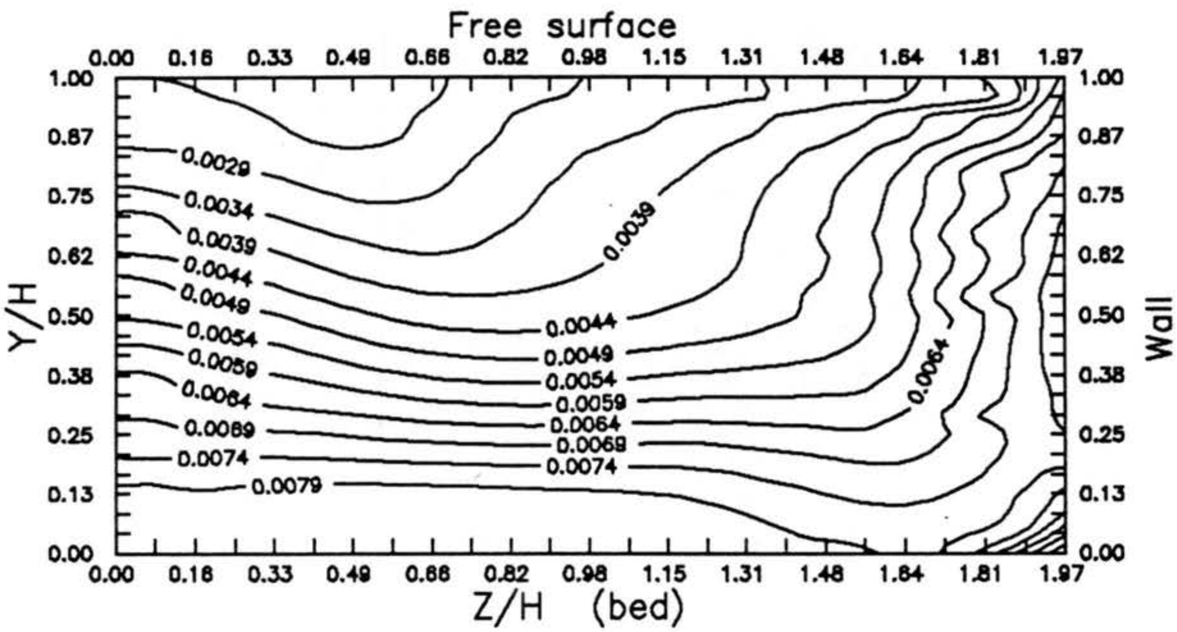

Figure 4.43 Predicted Turbulent Kinetic Energy Contour Lines (Normalized by U_o^2)for the Smooth Rectangular Open Channel (1:3.94). $H = 0.102$ m, $U_o = 0.187$ m/s, $R_e = 50,700$. (Right side of the channel. Centerline is to the left.)

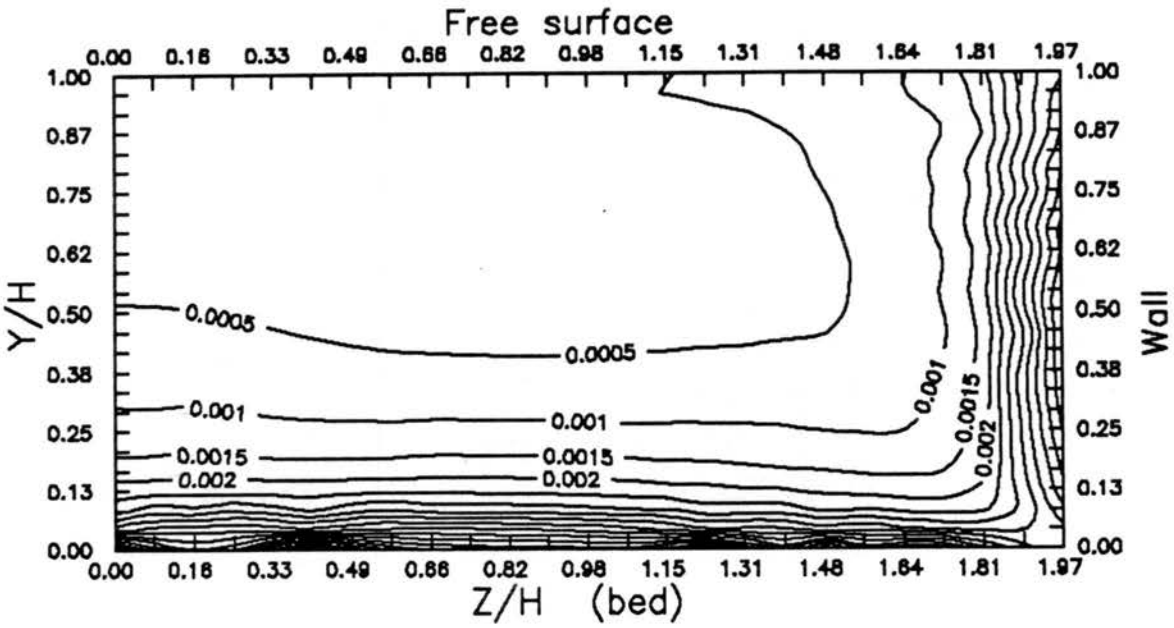

Figure 4.44 Predicted Rate of Dissipation Contour Lines (Normalized by U_o^3/H) for the Smooth Rectangular Open Channel (1:3.94). $H = 0.102$ m, $U_o = 0.187$ m/s, $R_e = 50{,}700$. (Right side of the channel. Centerline is to the left.)

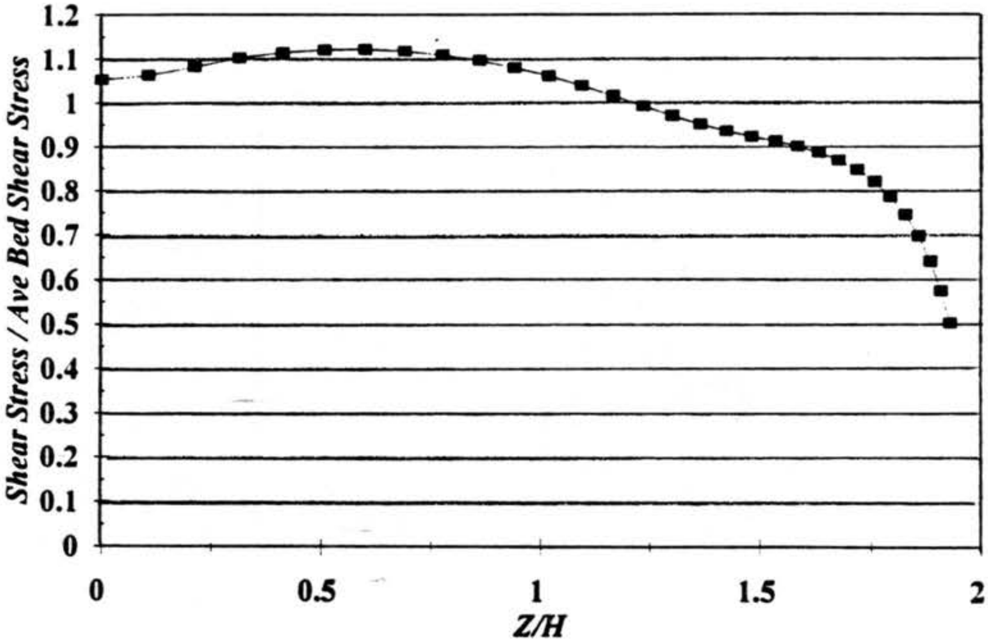

Figure 4.45a Predicted Bed Shear Stress for the Smooth Rectangular Open Channel (1:3.94). (Right side of the channel.)

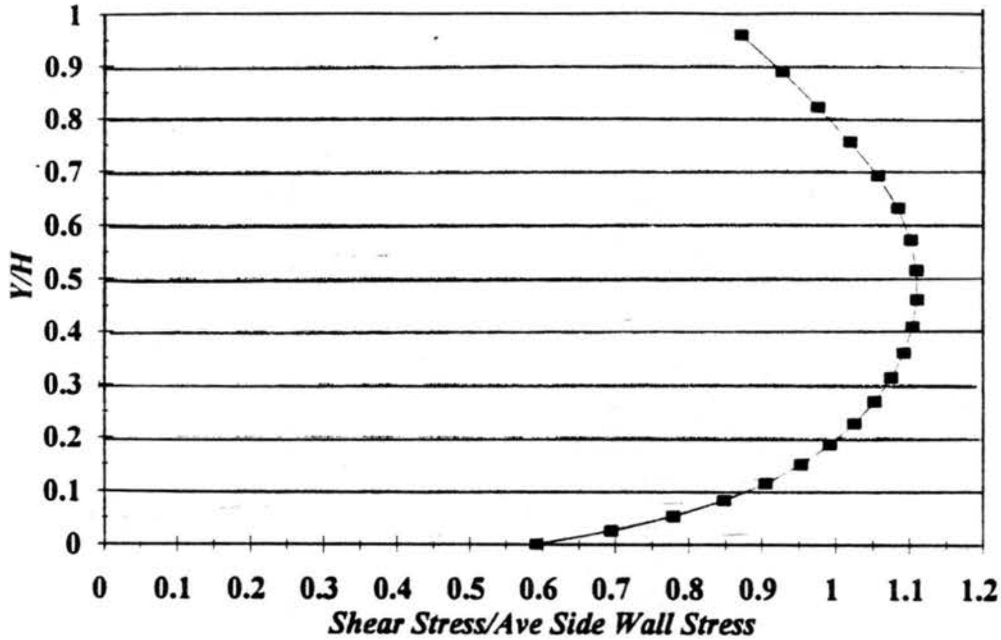

Figure 4.45b Predicted Side Wall Shear Stress for the Smooth Rectangular Open Channel (1:3.94).

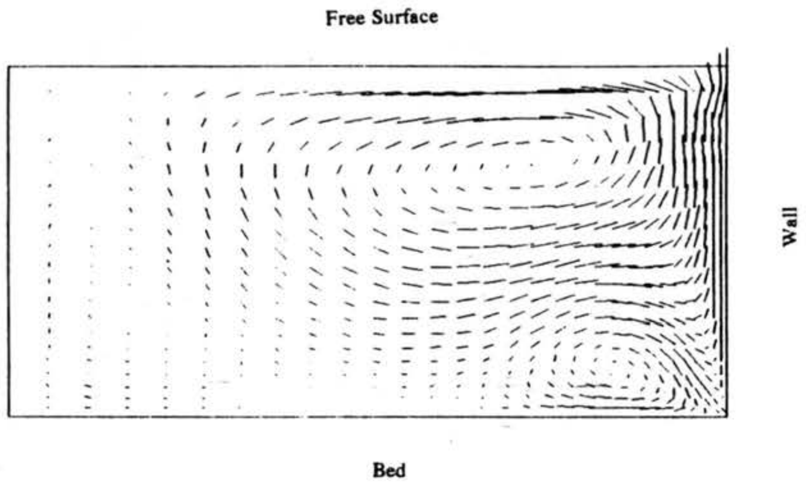

Figure 4.46 Predicted Secondary Flow in Rough Rectangular Open Channel (1:4.1). R_e = 73,500.
(Right side of the channel. Centerline is to the left.)

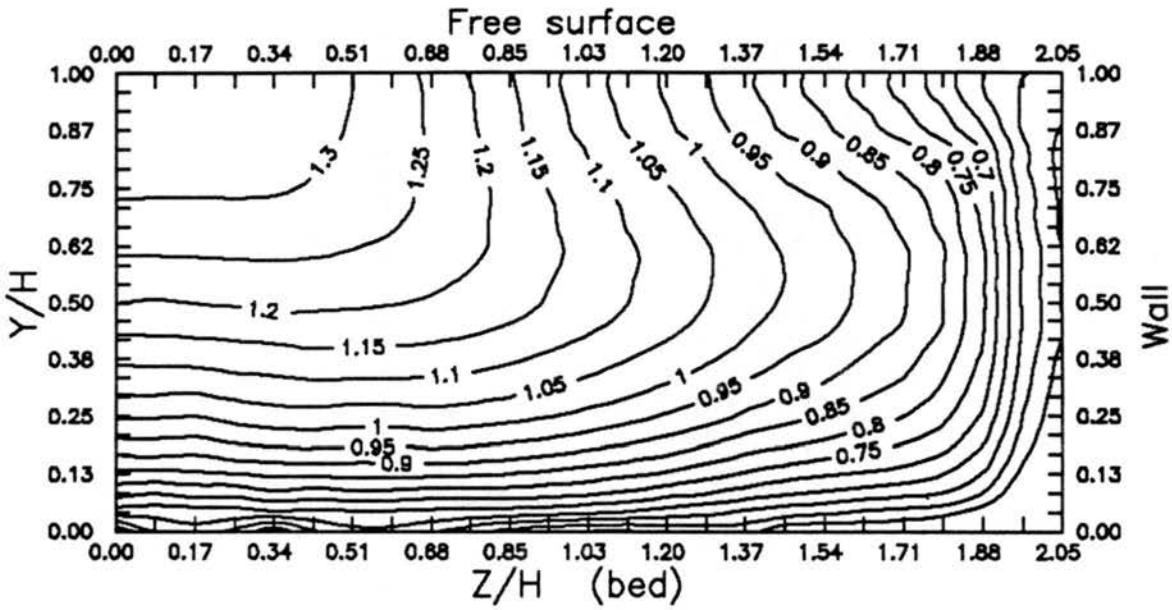

Figure 4.47 Predicted Main Velocity Contour Lines (Normalized by a velocity = 0.371 m/s) in Rough Rectangular Open Channel (1:4.1). H = 0.077 m, R_e = 73,500. (Right side of the channel. Centerline is to the left.)

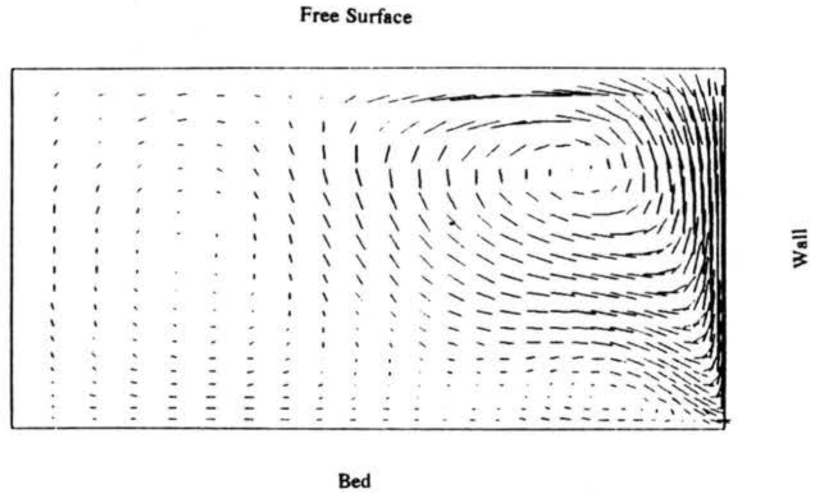

Figure 4.48 **Predicted Secondary Flow in Smooth Side Walls and Rough Bed Rectangular Open Channel (1:3.96). (Right side of the channel. Centerline is to the left.)**

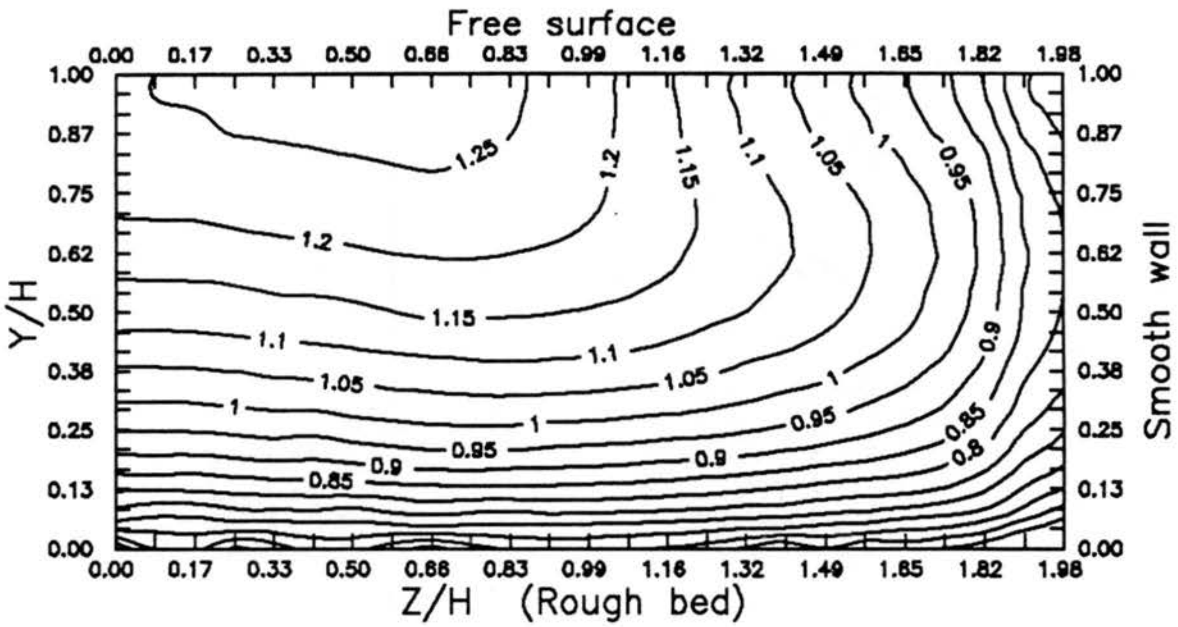

Figure 4.49 Predicted Main Velocity Contour Lines (Normalized by a velocity = 0.346 m/s) in Smooth Side Walls and Rough Bed Rectangular Open Channel (1:3.96). H = 0.101 m, R_e = 79,300.
(Right side of the channel. Centerline is to the left.)

Figure 4.50 Cross Section of the Flume with Stripes of Roughness and Grid of Measuring Points in the Experiment by Muller & Studerus (1979).

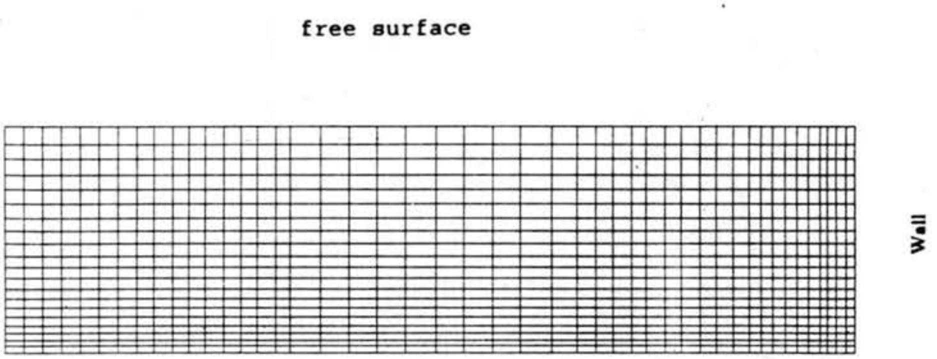

Figure 4.51 The Mesh for Rectangular Open Channel (1:7.5) with Periodic Roughness. (Right side of the channel. Centerline is to the left.)

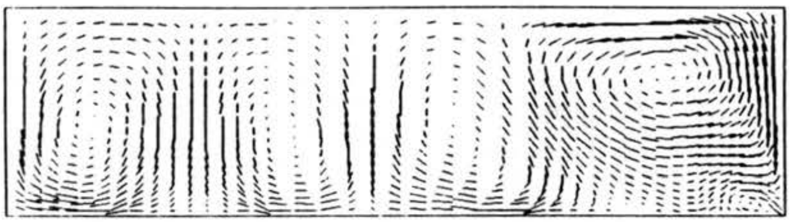

Figure 4.52a Predicted Secondary Flow for Rectangular Open Channel (1:7.5) with Periodic Roughness.
$R_* = 44{,}000$, $K_s = 0.0025$ m.
(Right side of the channel.
Centerline is to the left.)

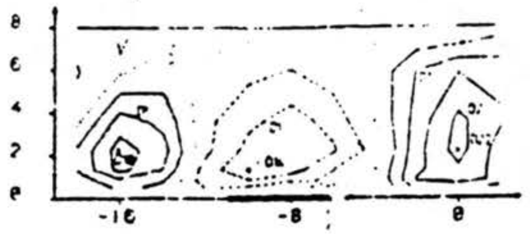

Figure 4.52b Measured Secondary Flow (Lines of constant V/U_o) for Rectangular Open Channel (1:7.5) with Periodic Roughness (0.0025 m), Muller & Studerus (1979). R_e = 44,000, K_s = 0.0025 m. (Left side of the channel. Centerline is to the right.)

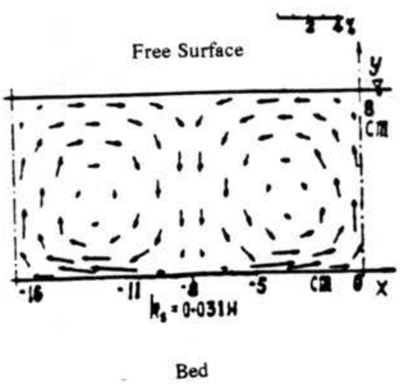

Figure 4.52c Predicted Secondary Flow for Rectangular Open Channel (1:7.5) with Periodic Roughness, Naot (1984). R_e = 44,000, K_s =0.0025 m. (left side of the channel. Centerline is to the right.)

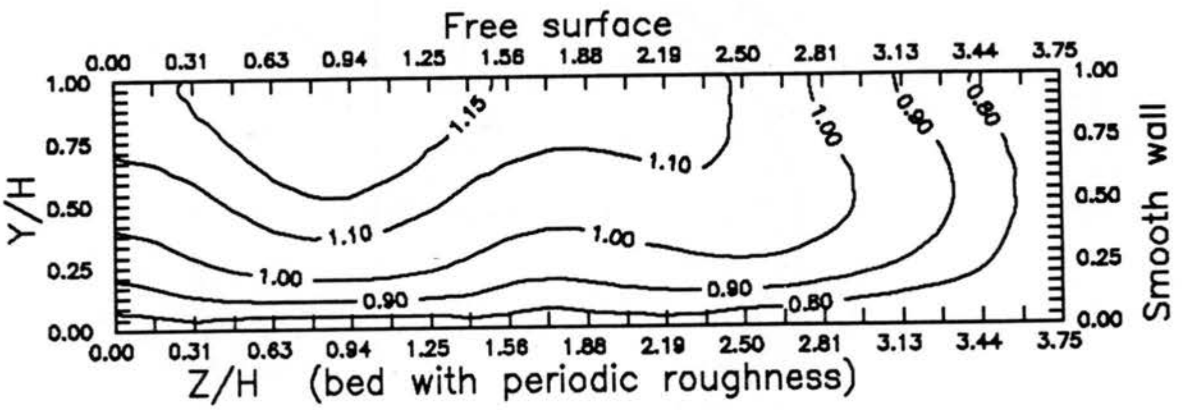

Figure 4.53a Predicted Main Velocity Contour Lines (Normalized by U_o) for Rectangular Open Channel (1:7.5) with Periodic Roughness. K_s =0.0025 m, H = 0.08 m, U_o =0.55 m/s, R_e = 44,000. (Right side of the channel. Centerline is to the left.)

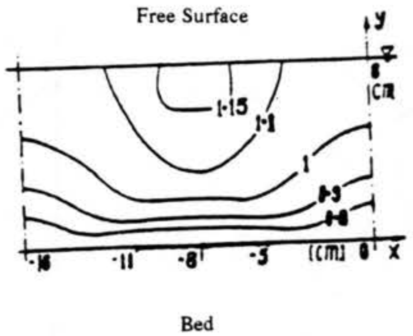

Figure 4.53b Predicted Main Velocity for Rectangular Open Channel (1:7.5) with Periodic Roughness, Naot (1984). K_s = 0.0025 m, R_e = 44,000. (Section of the channel.)

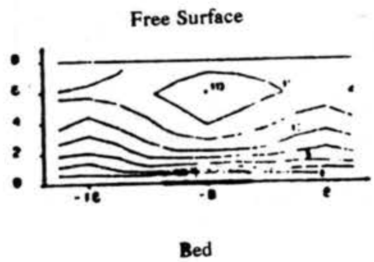

Figure 4.53c Measured Main Velocity for Rectangular Open Channel (1:7.5) with Periodic Roughness, Muller and Studerus (1979). K_s =0.0025 m, R_e = 44,000. (Section of the channel.)

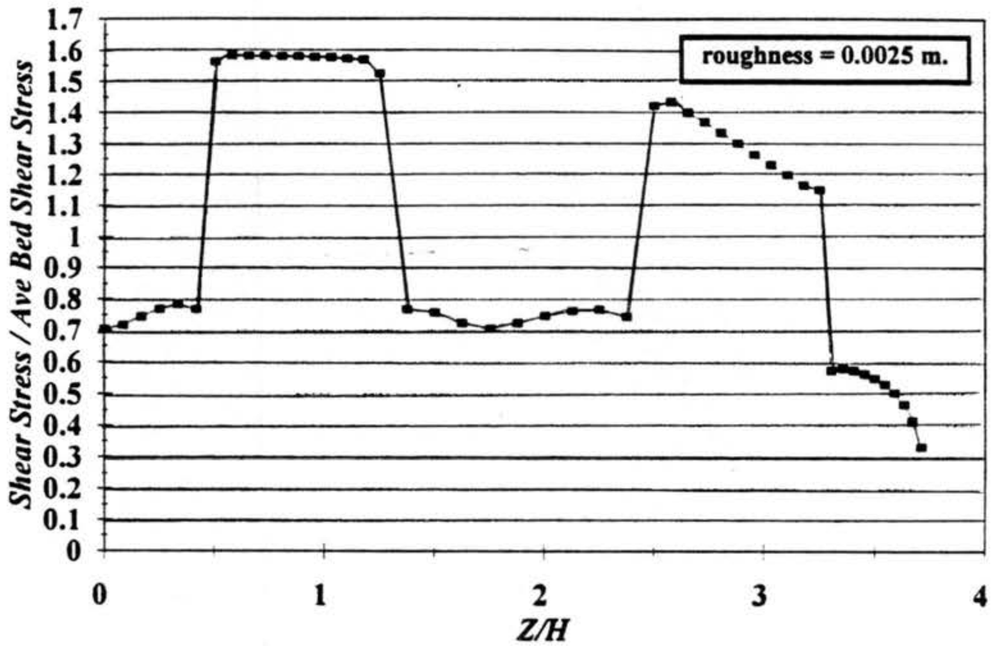

Figure 4.54a Predicted Bed Shear Stress for Rectangular Open Channel (1:7.5) with Periodic Roughness (0.0025 m). (Right half of the bed.)

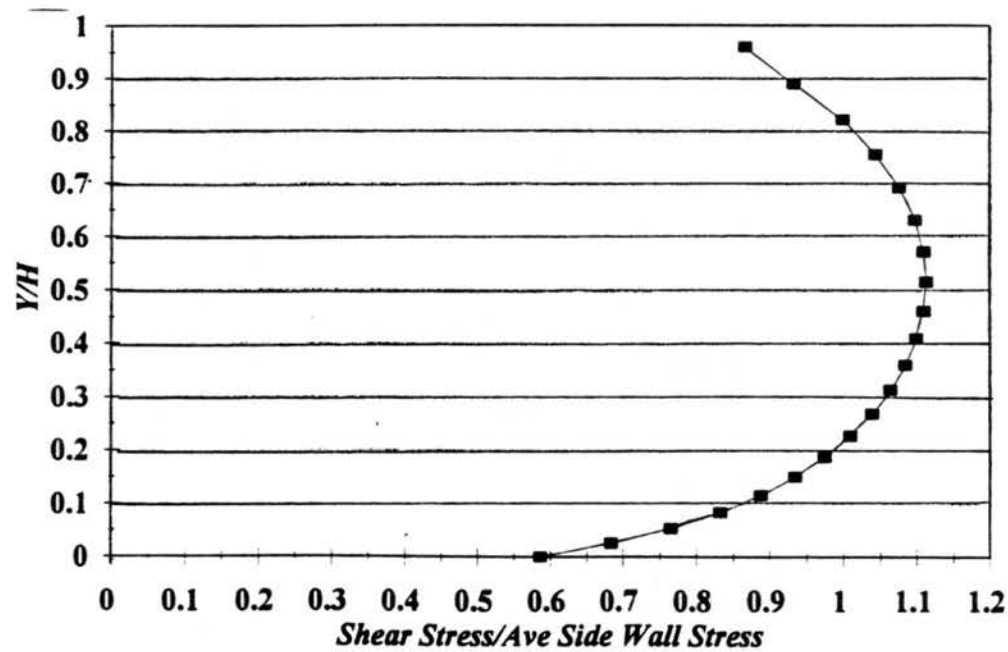

Figure 4.54b Predicted Side Wall Shear Stress for Rectangular Open Channel (1:7.5) with Periodic Roughness (0.0025 m).

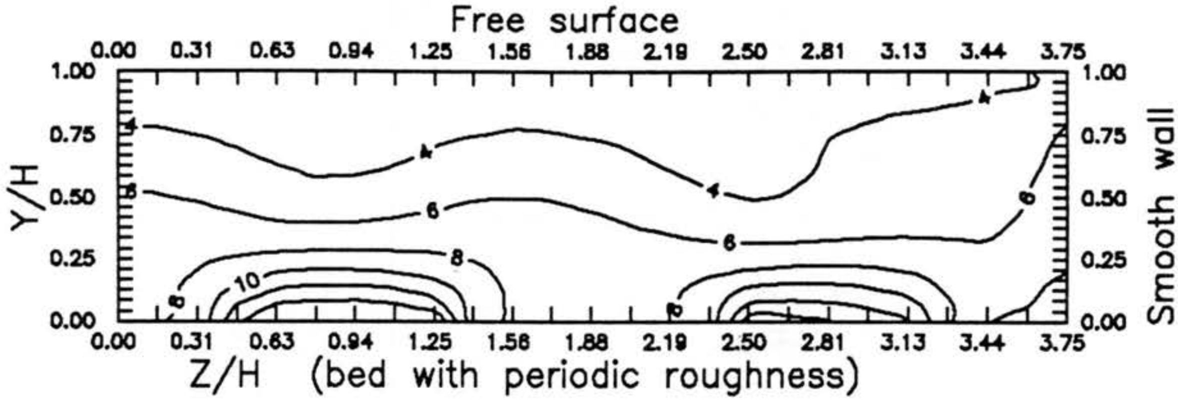

Figure 4.55a Predicted Turbulent Kinetic Energy Contour Lines (Normalized by U_o^2) for Rectangular Open Channel (1:7.5) with Periodic Roughness. K_s = 0.0025 m, U_o = 0.55 m/s, R_e = 44,000. (Right side of the channel. Centerline is to the left.)

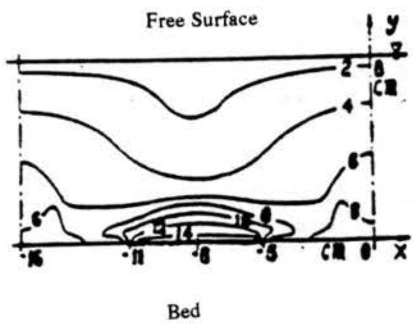

Figure 4.55b Measured Turbulent Kinetic Energy for Rectangular Open Channel (1:7.5) with Periodic Roughness (0.0025 m), Naot (1984). (Section of the channel.)

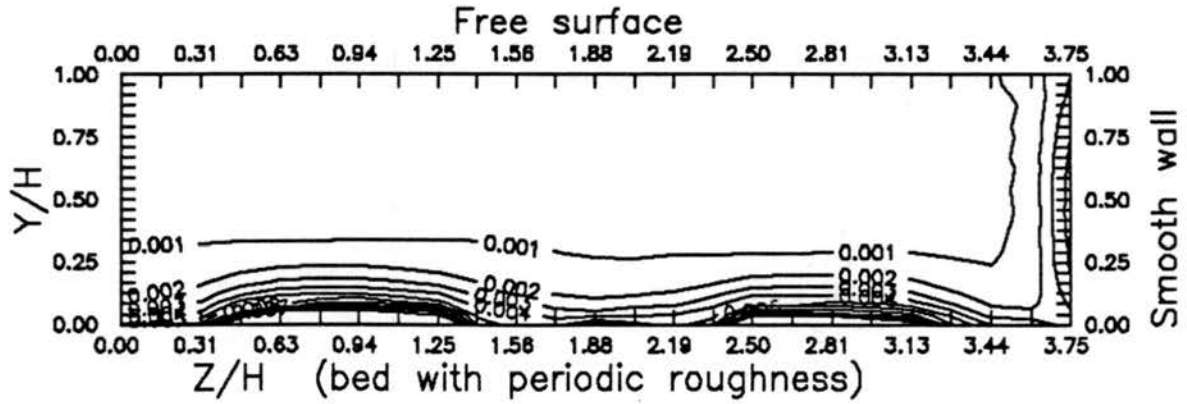

Figure 4.56 Predicted Rate of Dissipation Contour Lines (Normalized by U_o^3/H) for Rectangular Open Channel (1:7.5) with Periodic Roughness. K_s = 0.0025 m, H = 0.08 m, U_o = 0.55 m/s. (Right side of the channel. Centerline is to the left.)

Free Surface

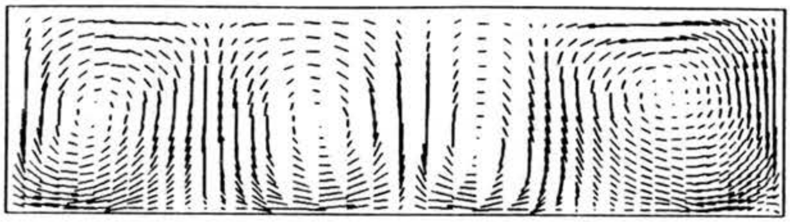

Wall

Bed

Figure 4.57 Predicted Secondary Flow for Rectangular Open Channel (1:7.5) with Periodic Roughness. K_s = 0.012 m. (Right side of the channel.Centerline is to the left.)

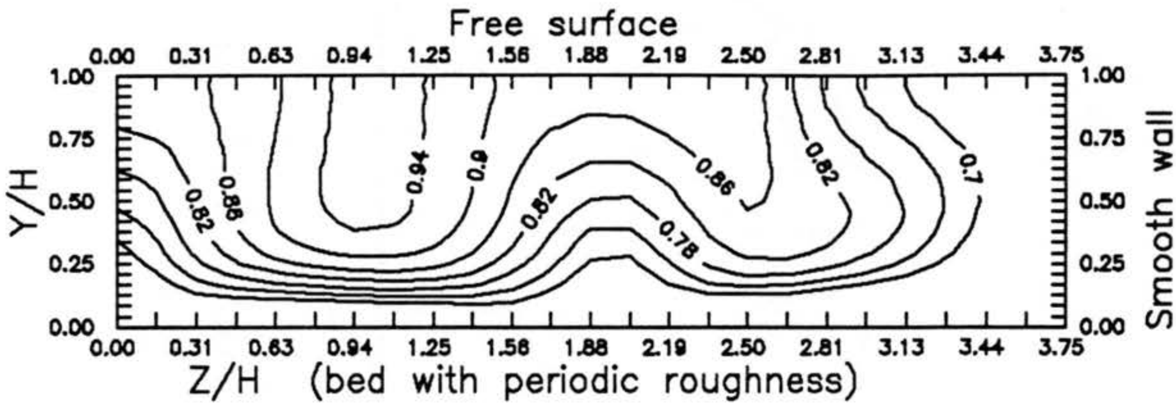

Figure 4.58 Predicted Main Velocity Contour Lines (Normalized by U_o) for Rectangular Open Channel (1:7.5) with Periodic Roughness. K_s = 0.012 m, U_o = 0.55 m/s, R_e = 33,700. (Right side of the channel. Centerline is to the left.)

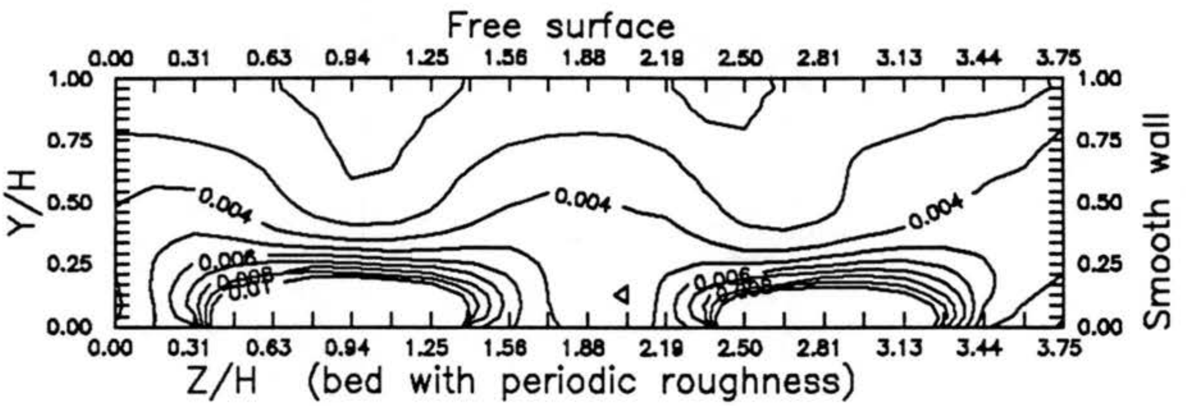

Figure 4.59 Predicted Turbulent Kinetic Energy Contour Lines (Normalized by U_o^2) for Rectangular Open Channel (1:7.5) with Periodic Roughness. K_s = 0.012 m, U_o =0.55 m/s, R_e = 33,700. (Right side of the channel. Centerline is to the left.)

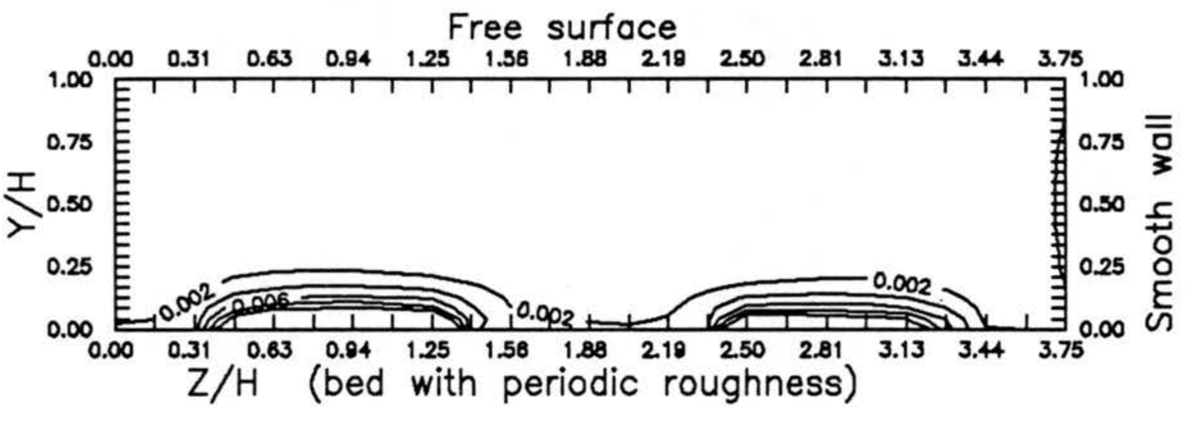

Figure 4.60 Predicted Rate of Dissipation Contour Lines (Normalized by U_o^3/H) for Rectangular Open Channel (1:7.5) with Periodic Roughness. K_s = 0.012 m, H = 0.08 m, U_o =0.55 m/s, R_e = 33,700. (Right side of the channel. Centerline is to the left.)

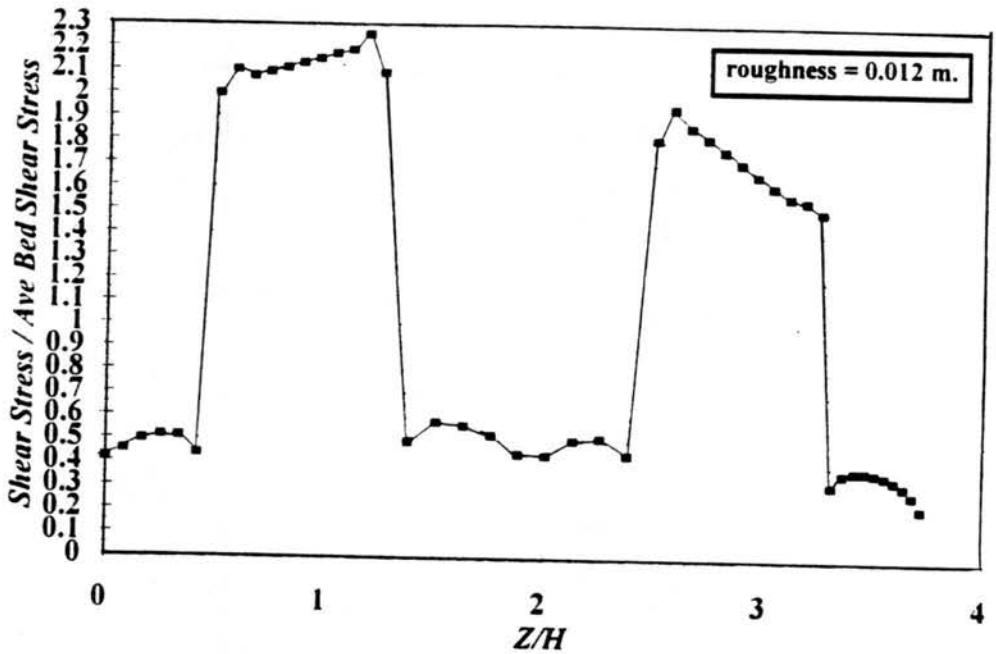

Figure 4.61 Predicted Bed Shear Stress for Rectangular Open Channel (1:7.5) with Periodic Roughness (0.012 m). (Right half of the bed channel.)

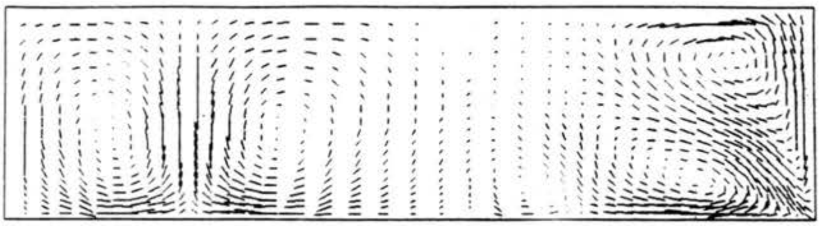

Figure 4.62 Predicted Secondary Flow for Rectangular Open Channel (1:7.5) with Periodic Roughness in case 4.3.3.
K_s = 0.0025 m, R_e = 42,200.
(Right side of the channel. Centerline is to the left.)

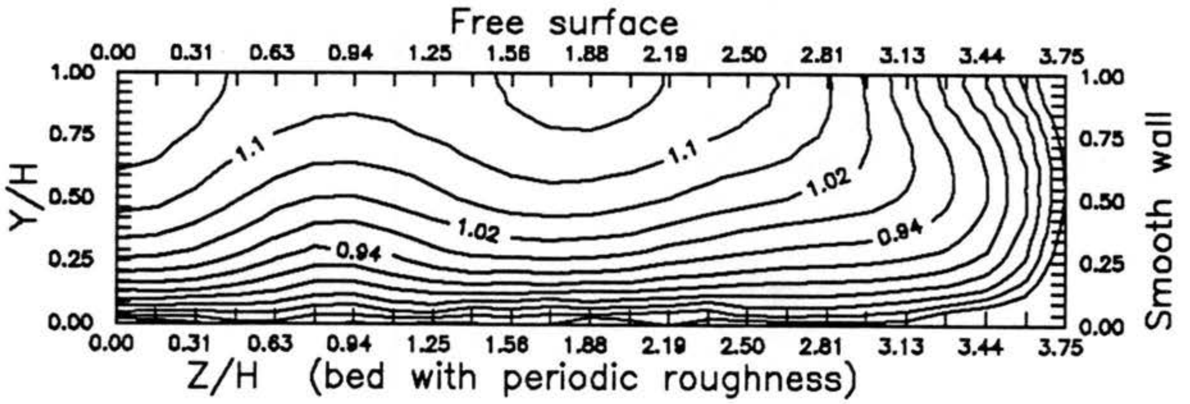

Figure 4.63 Predicted Main Velocity Contour Lines (Normalized by U_o) for Rectangular Open Channel (1:7.5) with Periodic Roughness in case 4.3.3. U_o = 0.55 m/s, K_s = 0.0025 m, R_e = 42,200.
(Right side of the channel. Centerline is to the left.)

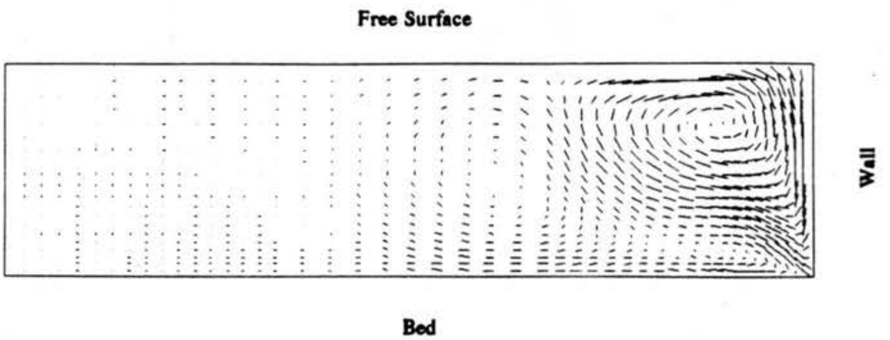

Figure 4.64 Predicted Secondary Flow in Rectangular Open Channel (1:7.5) with Smooth Side Wall and Uniform Rough Bed (K_s = 0.0025 m).
(Right side of the channel. Centerline is to the left.)

Free Surface

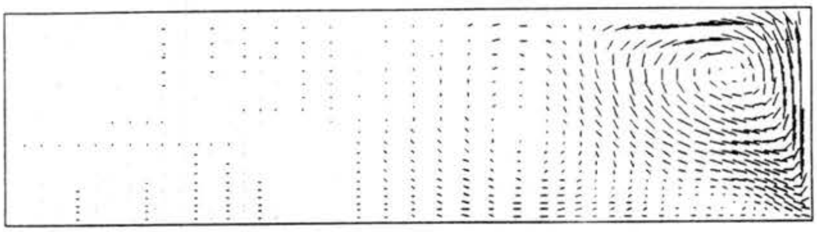

Bed

Wall

Figure 4.65 Predicted Secondary Flow in Rectangular Open Channel (1:7.5) with Smooth Side Wall and Uniform Rough Bed (K_s = 0.012 m).
(Right side of the channel. Centerline is to the left.)

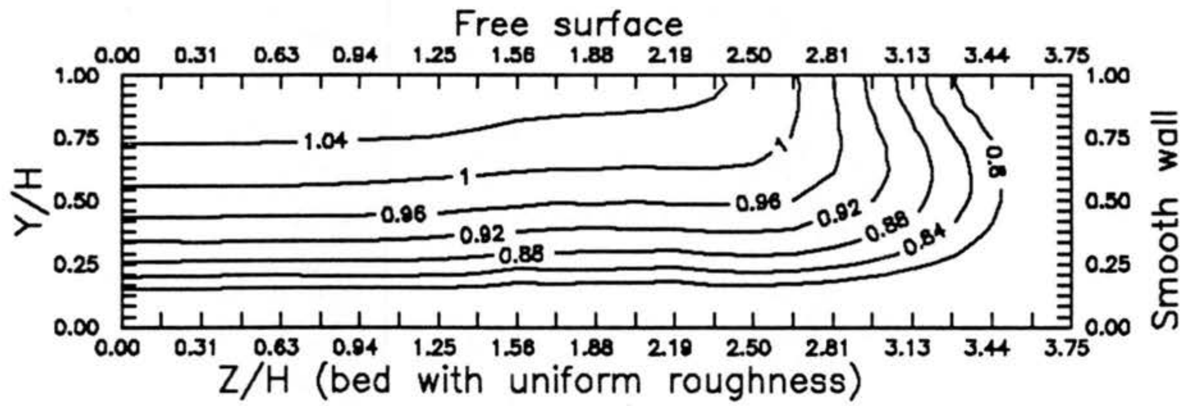

Figure 4.66 Predicted Main Velocity Contour Lines (Normalized by U_o) for Rectangular Open Channel (1:7.5) with Uniform Roughness. U_o = 0.55 m/s, K_s = 0.0025 m, R_e = 38,500. (Right side of the channel. Centerline is to the left.)

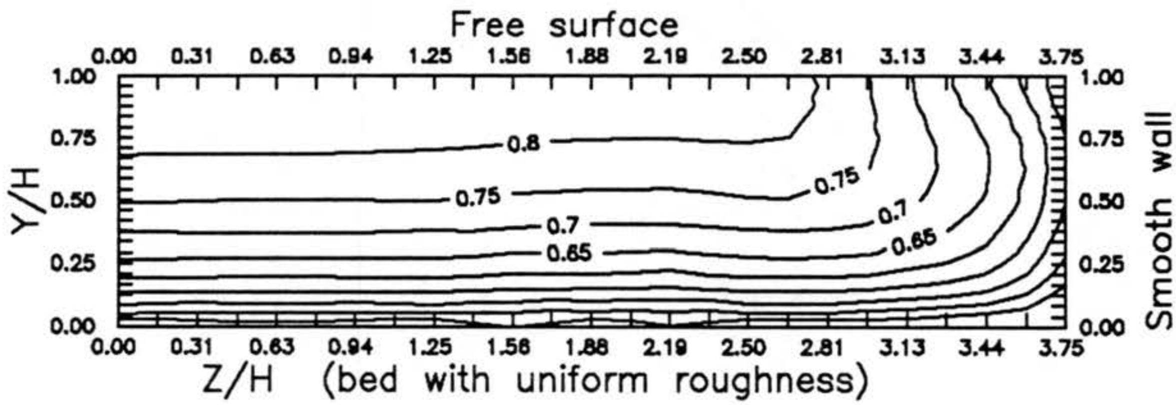

Figure 4.67 Predicted Main Velocity Contour Lines (Normalized by U_o) for Rectangular Open Channel (1:7.5) with Uniform Roughness. U_o = 0.55 m/s, K_s = 0.012 m, R_e = 29,300. (Right side of the channel. Centerline is to the left.)

APPENDIX C

TABLES

Table 4.1

Input Data for Closed Channels to the Computer Model

Fluid (air) viscosity = 0.001657 ft^2/s , Fluid density = 0.002301 $slugs/ft^3$

Type of Duct	H (ft)	B/2H	K_s (ft)	R_e	U_o (ft/s)	u_* (ft/s)	$-dP^*/dx^*$	C_μ	Data Source
1. Square (S)	0.125	1	0.00	83,000	54.80	2.55	0.00433	0.068	Leutheusser (1963)
2. Square (R) *	0.125	1	0.02	40,500	54.80	2.55	0.00433	0.068	-
3. Square (S & R) *	0.125	1	0.02	53,000	54.80	2.55	0.00433	0.068	-
4. Rectangular (S)	0.125	3	0.00	92,190	40.818	1.943	0.00302	0.075	Leutheusser (1963)
5. Rectangular (R) *	0.125	3	0.02	49,000	40.818	1.943	0.00302	0.075	-
6. Rectangular (S&R) *	0.125	3	0.02	78,000	40.818	1.943	0.00302	0.075	-

S = Smooth wall
R = Rough wall
S&R = Smooth side walls, rough top and bottom walls
* Data did not exist and U_o and u_* are only normalizing variables

Table 4.2

Initial Values for Starting Closed Channel Computer Model

Type of Duct	U_o	V_o	W_o	P_o	K_o	ϵ_o
1. Square (S)	1.0	0.0	0.0	0.0	0.005	0.001
2. Square (R)	1.0	0.0	0.0	0.0	0.005	0.001
3. Square (S&R)	1.0	0.0	0.0	0.0	0.005	0.001
4. Rectangular (S)	1.0	0.0	0.0	0.0	0.005	0.001
5. Rectangular (R)	1.0	0.0	0.0	0.0	0.005	0.001
6. Rectangular (S&R)	1.0	0.0	0.0	0.0	0.005	0.001

Note : All the variables in the table are normalized
S = Smooth wall
R = Rough wall
S&R = Smooth side walls, rough top and bottom walls
U_o = Initial starting value at all nodes for the main velocity
V_o = Initial starting value at all nodes for the V secondary velocity
W_o = Initial starting value at all nodes for the W secondary velocity
P_o = Initial starting value at all nodes for the pressure
K_o = Initial starting value at all nodes for K
ϵ_o = Initial starting value at all nodes for ϵ

Table 4.3

Mesh Data and Number of Iterations for Closed Channels

Type of Duct	Domain	No. of elements	No. of Nodes	Mesh Division	No. of Iterations
1. Square (S)	0.96 x 0.96	400	441	20 x 20	280
2. Square (R)	0.96 x 0.96	400	441	20 x 20	370
3. Square (S&R)	0.96 x 0.96	400	441	20 x 20	440
4. Rectangular (S)	2.96 x 0.96	450	496	30 x 15	920
5. Rectangular (R)	2.96 x 0.96	450	496	30 x 15	330
6. Rectangular (S&R)	2.96 x 0.96	450	496	30 x 15	390

S = Smooth wall
R = Roug wall
S&R = Smooth side walls, rough top and bottom walls

Table 4.4

Output Results For Closed Channels

Type of Duct	ΔU x 10^4	ΔV x 10^4	ΔW x 10^4	ΔK x 10^5	$\Delta \epsilon$ x 10^5	Divmax x 10^7	Divmin x 10^7	Qp/Qm
1. Square (S)	3.6	2.20	2.2	8.20	1.500	0.21	-0.92	1.009
2. Square (R) *	6.2	0.70	0.7	8.20	1.400	0.32	-0.85	-
3. Square (S&R) *	2.6	3.30	3.3	5.70	1.500	0.79	-0.99	-
4. Rectangular (S)	6.6	0.69	1.3	0.12	0.076	1.10	-2.60	1.030
5. Rectangular (R) *	4.1	2.60	2.6	8.10	1.400	1.30	-2.50	-
6. Rectangular (S&R) *	6.0	1.10	1.6	8.20	1.200	3.60	-3.90	-

S = Smooth wall
R = Rough wall
S&R = Smooth side walls, rough top and bottom walls
ΔU, ΔV, and ΔW = Absolute sum at all nodes of the U, V, and W velocity corrections respectively
ΔK and $\Delta \epsilon$ = Absolute sum at all nosed of the K and ϵ corrections
Divmax and Divmin = Maximum and minimum of the incompressibility error
Qp = Predicted discharge
Qm = measured discharge
* = Cases that have no measured discharge

Table 4.5

Input Data for Open Channels to the Computer Model

Fluid (water) viscosity = 1.31×10^{-6} m^2/s, Fluid density = 1000 kg/m^3

Type of open channel	B/H	Depth (m)	K_s (m)	R_e	U_o (m/s)	u_* (m/s)	slope $\times 10^4$	Data Source
1. Rectangular (S)	2.00	0.0760	0.000	39,000	0.338	0.0155	9.66	Knight et al. (1984)
2. Rectangular (R)	2.00	0.1577	0.012	87,300	0.298	0.0198	7.60	Tominaga et al. (1989),R14
3. Rectangular (S&R) *	2.00	0.1577	0.012	104,760	0.298	0.0198	7.60	
4. Rectangular (S)	3.94	0.1015	0.000	50,700	0.187	0.0074	1.38	Tominaga et al. (1989),S2
5. rectangular (R)	4.10	0.0770	0.012	73,500	0.371	0.0250	20.5	Tominaga et at. (1989),R13
6. Rectangular (S&R)	3.96	0.1010	0.012	79,300	0.346	0.0205	10.6	Tominaga et al. (1989),R22

S = Smooth side walls and bed
R = Rough side walls and bed
S&R = Smooth side walls and rough bed
* Data did not exist and U_o and u_* are only normalizing variables

Table 4.6

Initial Values for Starting Open Channel Computer Model

Type of Open Channel	U_o	V_o	W_o	P_o	K_o	ϵ_o
1. Rectangular (S) (1:2)	1.0	0.0	0.0	0.0	0.005	0.001
2. Rectangular (R) (1:2)	1.0	0.0	0.0	0.0	0.015	0.003
3. Rectangular (S&R) (1:2)	1.0	0.0	0.0	0.0	0.018	0.004
4. Rectangular (S) (1:3.94)	1.0	0.0	0.0	0.0	0.005	0.001
5. Rectangular (R) (1:4.1)	1.0	0.0	0.0	0.0	0.015	0.005
6. Rectangular (S&R) (1:3.96)	1.0	0.0	0.0	0.0	0.015	0.003

Note : All the variables in the table are normalized
S = Smooth side walls and bed
R = Rough side walls and bed
S&R = Smooth side walls and rough bed
U_o = Initial starting value at all nodes for the main velocity
V_o = Initial starting value at all nodes for the V secondary velocity
W_o = Initial starting value at all nodes for the W secondary velocity
P_o = Initial starting value at all nodes for the pressure
K_o = Initial starting value at all nodes for K
ϵ_o = Initial starting value at all nodes for ϵ

Table 4.7

Mesh Data and Number of Iterations for Open Channels

Type of open channel	Domain	No. of elements	No. of Nodes	Mesh Division	No. of Iterations
1. Rectangular (S) (1:2)	0.96 x 0.96	400	441	20 x 20	320
2. Rectangular (R) (1:2)	0.96 x 0.96	600	651	20 x 30	320
3. Rectangular (S&R) (1:2)	0.96 x 0.96	600	651	20 x 30	420
4. Rectangular (S) (1:3.94)	1.93 x 0.96	600	651	30 x 20	470
5. Rectangular (R) (1:4.1)	2.01 x 0.96	600	651	30 x 20	560
6. Rectangular (S&R) (1:3.96)	1.94 x 0.96	600	651	30 x 20	900

S = Smooth side walls and bed
R = Rough side walls and bed
S&R = Smooth side walls and rough bed

Table 4.8

Output Results For Open Channels

Type of Open channel	$\Delta U \times 10^4$	$\Delta V \times 10^4$	$\Delta W \times 10^4$	$\Delta K \times 10^5$	$\Delta \epsilon \times 10^5$	Divmax $\times 10^{10}$	Divmin $\times 10^{10}$	Qp/Qm
1. Rectangular (S) (1:2)	2.6	2.8	3.0	6.1	1.6	2.10	-3.40	1.057
2. Rectangular (R) (1:2)	1.8	3.4	3.4	6.9	2.7	1.10	-1.00	0.951
3. Rectangular (S&R) (1:2) *	1.6	3.9	3.2	1.0	3.9	0.72	-1.30	-
4. Rectangular (S) (1:3.94)	1.3	4.0	4.3	6.3	1.3	3.70	-5.30	0.957
5. Rectangular (R) (1:4.1)	2.0	3.7	3.4	6.7	2.5	7.50	-5.10	0.946
6. Rectangular (S&R) (1:3.96)	2.9	3.1	2.6	7.2	2.7	6.20	-10.0	0.99

S = Smooth side walls and bed
R = Rough side walls and bed
S&R = Smooth side walls and rough bed
ΔU, ΔV, and ΔW = Absolute sum at all nodes of the U, V, and W velocity corrections respectively
ΔK and $\Delta \epsilon$ = Absolute sum at all nosed of the K and ϵ corrections
Divmax and Divmin = Maximum and minimum of the incompressibility error
Qp = Predicted discharge
Qm = measured discharge
* = Case that have no measured data

Table 4.9

Input Data for Open Channels with Periodic or Uniform Roughness

Fluid (water) viscosity = 1.31×10^{-6} , Fluid density = 1000 kg/m^3

Type of open channel	Depth (m)	K_s (m)	R_e	U_o (m/s)	u_* (m/s)	slope x 10^4	Data Source
1. Rectangular (P) (1:7.5)	0.08	0.0025	44,000	0.55	0.031	15.2	Muller and Studerus (1979)
2. Rectangular (P) * (1:7.5)	0.08	0.0120	33,700	0.55	0.031	15.2	
3. Rectangular (P) * (1:7.5)	0.08	0.0025	42,200	0.55	0.031	15.2	
4. Rectangular (U) * (1:7.5)	0.08	0.0025	38,500	0.55	0.031	15.2	
5. rectangular (U) * (1:7.5)	0.08	0.0120	29,300	0.55	0.031	15.2	

P = open channels with periodic roughness on the bed and smooth side walls
U = open channels with uniform roughness on the bed and smooth side walls
* Measurements did not exist and U_o and u_* are only normalizing variables

Table 4.10

Initial Values for Starting Open Channel with Periodic or Uniform Roughness

Type of Open Channel	R_e	U_o	V_o	W_o	P_o	K_o	ϵ_o
1. Rectangular (p) (1:7.5)	44,000	1.0	0.0	0.0	0.0	0.009	0.001
2. Rectangular (p) (1:7.5)	33,700	1.0	0.0	0.0	0.0	0.009	0.001
3. Rectangular (p) (1:7.5)	42,200	1.0	0.0	0.0	0.0	0.009	0.001
4. Rectangular (U) (1:7.5)	38,500	1.0	0.0	0.0	0.0	0.009	0.001
5. Rectangular (U) (1:7.5)	29,300	1.0	0.0	0.0	0.0	0.009	0.001

Note : All the variables in the table are normalized
P = Open channels with periodic roughness on the bed and smooth side walls
U = open channels with uniform roughness on the bed and smooth side walls
U_o = Initial starting value at all nodes for the main velocity
V_o = Initial starting value at all nodes for the V secondary velocity
W_o = Initial starting value at all nodes for the W secondary velocity
P_o = Initial starting value at all nodes for the pressure
K_o = Initial starting value at all nodes for K
ϵ_o = Initial starting value at all nodes for ϵ

Table 4.11

Mesh Data and Number of Iterations for Open Channels with Periodic or Uniform Roughness

Type of open channel	R_e	Domain	No. of elements	No. of Nodes	Mesh Division	Time (minutes)	No. of Iterations
1. Rectangular (p) (1:7.5)	44,000	3.71 x 0.96	920	987	46 x 20	68	300
2. Rectangular (p) (1:7.5)	33,700	3.71 x 0.96	920	987	46 x 20	145	700
3. Rectangular (p) (1:7.5)	42,200	3.71 x 0.96	920	987	46 x 20	80	360
4. Rectangular (U) (1:7.5)	38,500	3.71 x 0.96	920	987	46 x 20	118	530
5. Rectangular (U) (1:7.5)	29,300	3.71 x 0.96	920	987	46 x 20	123	550

p = open channels with periodic roughness on the bed and smooth side walls
U = open channels with uniform roughness on the bed and smooth side walls

Table 4.12

Output Results For Open Channels with Periodic or Uniform Roughness

Type of Open channel	R_e	$\Delta U \times 10^4$	$\Delta V \times 10^4$	$\Delta W \times 10^4$	$\Delta K \times 10^5$	$\Delta \epsilon \times 10^6$	Divmax $\times 10^{10}$	Divmin $\times 10^{10}$	Qp/Qm
1. Rectangular (p) (1:7.5)	44,000	0.79	2.0	4.50	0.08	1.4	1.5	-0.9	0.973
2. Rectangular (p) (1:7.5) *	33,700	6.90	6.4	11.0	5.70	1.0	4.8	-4.1	-
3. Rectangular (p) (1:7.5) *	42,200	2.50	3.5	3.7	1.20	2.4	2.0	-1.8	-
4. Rectangular (U) (1:7.5) *	38,500	2.90	2.0	2.4	1.50	2.6	1.9	-1.4	-
5. Rectangular (U) (1:7.5) *	29,300	1.60	2.1	2.5	2.70	5.6	1.8	-1.4	-

p = open channels with periodic roughness on the bed and smooth side walls
U = open channels with uniform roughness on the bed and smooth side walls
* = cases that have no measured discharge
ΔU, ΔV, and ΔW = Absolute sum at all nodes of the U, V, and W velocity corrections respectively
ΔK and $\Delta \epsilon$ = Absolute sum at all nosed of the K and ϵ corrections
Divmax and Divmin = Maximum and minimum of the incompressibility error
Qp = Predicted discharge
Qm = measured discharge
* = Case that have no measured data